SPIN-CROSSOVER BEYOND THE TRADITIONAL FE(II) COMPLEXES: AB INITIO STUDY OF SPIN STATE STABILITY IN COMPLEXES WITH MN, NI AND RU

Gerard Alcover Fortuny

UNIVERSITAT ROVIRA i VIRGILI

Spin-Crossover beyond the traditional Fe(II) complexes: ab initio study of spin state stability in complexes with Mn, Ni and Ru

GERARD ALCOVER FORTUNY

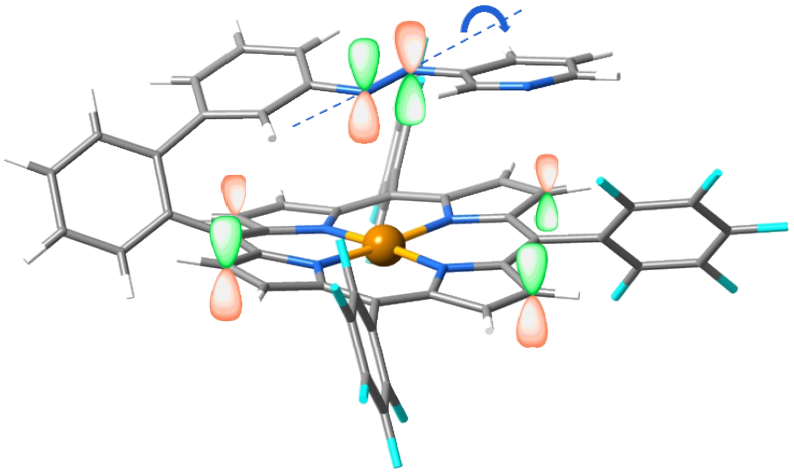

PhD THESIS

2016

Gerard Alcover Fortuny

Spin-Crossover beyond the traditional Fe(II) complexes: ab initio study of spin state stability in complexes with Mn, Ni and Ru

PhD Thesis

Supervised by Dr. Coen de Graaf and Dr. Rosa Caballol

Department of Physical and Inorganic Chemistry
Quantum Chemistry Group

UNIVERSITAT
ROVIRA i VIRGILI

Tarragona
2016

UNIVERSITAT ROVIRA I VIRGILI
DEPARTAMENT DE QUÍMICA FÍSICA I INORGÀNICA
Campus Sescelades
Marcel·lí Domingo, s/n
43007 Tarragona
Tel. +34 977 55 81 37
Fax +34 977 55 95 63
www.quimica.urv.es

Coen de Graaf, investigador ICREA, i Rosa Caballol Lorenzo, catedràtica de Química Física, del Departament de Química Física i Inorgànica de la Universitat Rovira i Virgili,

Fem constar a la comunitat científica que la tesi:

Spin-Crossover beyond the traditional Fe(II) complexes: ab initio study of spin-state stability in complexes with Mn, Ni and Ru

ha estat realitzada sota la nostra direcció en l'esmentat departament per Gerard Alcover Fortuny per a l'obtenció del títol de Doctor, i que acompleix els requeriments per a poder optar a la Menció Internacional al títol.

Tarragona, 27 de juny de 2016

El director de la tesi

Coen de Graaf

La directora de la tesi

Rosa Caballol Lorenzo

Acknowledgements

Aquesta tesi ha estat possible gràcies al suport de totes aquelles persones que dia rere dia han estat al meu costat i no han dubtat mai en ajudar-me. És per això que vull dedicar aquestes primeres pàgines a totes elles.

Primerament als meus directors de tesi Coen de Graaf i Rosa Caballol per la paciència, amabilitat i simpatia que sempre han mostrat i per totes les coses que he après al seu costat.

Ha estat un plaer elaborar aquesta tesi al Grup de Química Quàntica entre d'altres coses per l'equip humà que el forma. Per una banda els membres sèniors Jordi Carbó, Anna Clotet, Xavi López, Josep Maria Poblet, Mar Reguero i Toni Rodríguez perquè sempre que he necessitat alguna cosa m'he trobat les portes de tots els despatxos obertes. Per altra banda l'equip tècnic format per Moises Àlvarez, Elisenda Mas i José Ortiz per l'imprescindible suport logístic que m'han prestat aquests anys.

Són molts els companys que han passat pel grup i amb els quals he tingut el plaer de compartir no només moments de feina sinó també de festa i mil coses més. Entre ells Mariano, Jhon, Pedro, Magda, Sergi, Sonia, Jessica, Pablo A., Pablo J., Xavi, Núria, Laura, Marc, Gian, Albert, Juan Carlos, Jianfang, Zhongling i Roser. Un esment especial pel Pep Casellas amb el qual he tingut el privilegi de treballar colze a colze en diversos projectes.

Durant la meva estada a Bèlgica vaig tenir la sort de comptar amb el suport de bons amics de tota la vida com els Eric Wiliquet pare i fill i tota la seva família

als quals mai els podré agrair prou el fet d'haver-me obert les portes de casa seva. També al Maxime, al Mathieu i al Jon per tractar-me com un més de la seva colla i als amics que vaig fer a la KU Leuven Thanos, Ana i Daryna. Finalment a la Kristine Pierloot per donar-me l'oportunitat d'haver tingut aquesta enriquidora experiència.

Als amics de tota la vida, aquells que siguin on siguin no fallen mai. Al Marsal i la Victòria, al Pepe i l'Alba, al Manel i la Marina i al Ruben. I també a la família dels Pokers, l'Emili i la Jennifer, el Marc Comí i l'Ares, l'Héctor, l'Aniol i el Joel perquè junts hem descobert que com deia Nietzsche sense música la vida seria un error.

I finalment a la meva família. Als meus pares Miquel Àngel i Maria Dolors, a la meva tieta Victòria, a la meva àvia Maria Dolors, a la meva germana Natàlia i a la meva parella Carmen. Perquè poder assolir l'èxit d'escriure una tesi doctoral és també fruit del seu esforç i la seva dedicació durant molts anys.

Contents

Chapter 1

Introduction

1.1 Spin state in transition metal complexes

In systems with unpaired electrons the spin angular moment plays a crucial role not only in the magnetic propierties but also in the structure, the reactivity and the spectroscopy. In contrast with organic molecules which usually have closed-shell ground states, in transition metal (TM) compounds with d^4-d^7 electronic configurations several states are often accessible due to the close energy of d-orbitals. High-spin (HS) and low-spin (LS) are the usual terms for the highest and lowest spin multiplicities, respectively [1].

The first attempts to explain the magnetic state of TMs were based on the Valence Bond Theory. In 1931 Pauling introduced the 'magnetic criterion of bond type' to explain why $[Fe(H_2O)_6]^{2+}$ is HS and $[Fe(CN)_6]^{4-}$ is LS. The Fe-OH_2 bond is considered an ion-dipole interaction in which the metal centre is described as a free Fe^{II} (d^6) ion in the (S=2) HS state (see Fig. 1.1 top). In contrast, the dative covalent Fe-CN bond implies d^2sp^3 hybridization to form the six-fold complex and hence only three d-orbitals of the metal are available to accommodate the six Fe^{II} d-electrons, giving the LS (S=0) state (see Fig. 1.1 below) [2]. This first approach reflected the influence of the metal-ligand interaction in the spin states of the TMs complexes. The Valence Bond Theory

is a useful tool among others to quantify the charge transfer extent between metal and ligands and to assign an oxidation state to the metal centre [3–6].

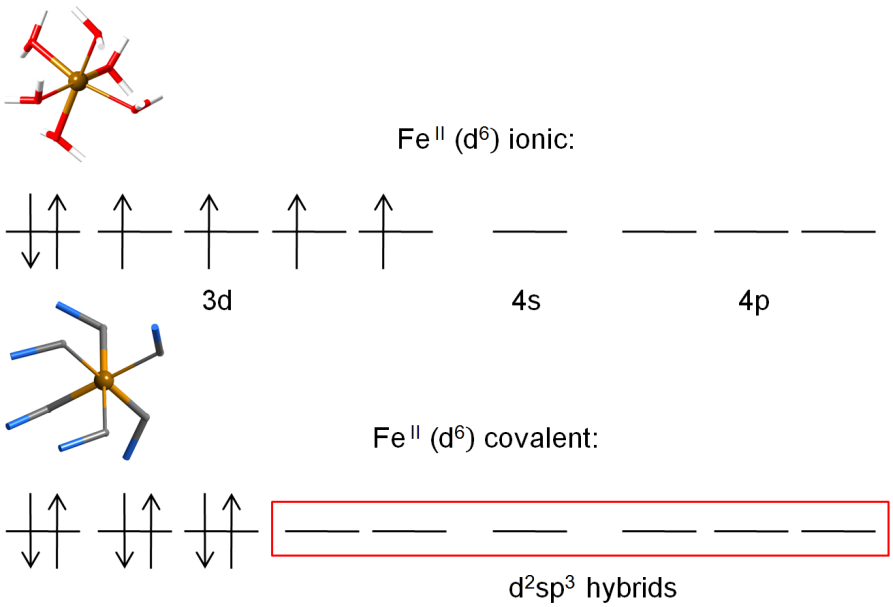

Figure 1.1. Valence Bond Theory LS and HS states description for octahedral Fe^{II} complexes.

Parallel to the Valence Bond Theory, the Ligand-Field Theory [7–9] was derived from the Crystal Field-Theory [10–12]. In this approach the TM d-orbitals are considered as atomic orbitals in an external potential and do not participate a priori in the metal-ligand bond. In an octahedral ligand-field the degeneracy of the d-orbitals is broken as shown in Fig. 1.2. The electrons in the e_g orbitals suffer a larger repulsion than those in the t_{2g} orbitals, since the former orbitals point directly to the ligands while the latter are oriented in between the ligands. The resulting energy gap between the lower t_{2g} and the higher e_g d-orbitals is known as the crystal-field splitting, $\triangle_{oct}$ or $10D_q$ in the Racah parameterization scheme. Hence, occupying an e_g orbital pushes up the energy of the electronic state by $6D_q$, while occupying a t_{2g} orbital lowers it by $4D_q$. Simultaneously, the loss of exchange interactions and to a lesser extent the increase of electron repulsion increases the energy of the electronic state by E_{pair} when two electron are placed in the same orbital.

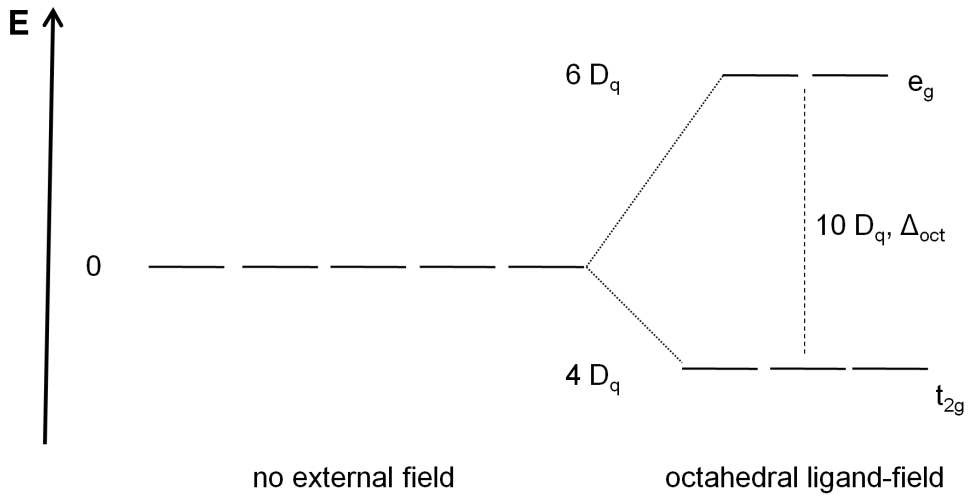

Figure 1.2. Breakdown of the metal d-orbitals degeneracy due to the ligand repulsion suffered in an octahedral ligand-field.

Coming back to the Fe^{II} example, the electronic configuration of the state with maximum spin multiplicity is $t_{2g}{}^4\ e_g{}^2$, which results in a net decrease of the energy of $4D_q$ with respect to the free ion. On the other hand, the state with all six electrons in the t_{2g} orbitals gains $24D_q$ compared to the free ion, but has two more pairs of electrons in the same orbital, and hence, looses $2E_{pair}$. The energy difference between the high-spin and the low-spin state is $20D_q$ - $2E_{pair}$ and, obviously depending on the importance of the ligand field, the ground state is either low-spin or high-spin. In weak-field ligands such as H_2O in $[Fe(H_2O)_6]^{2+}$ (see left part of Fig. 1.3), $\triangle_{oct}$ is smaller than E_{pair} favouring HS states, while strong-field ligands as CN- in $[Fe(CN_6]^{4-}$ favour electron pairing in the low-lying t_{2g} orbitals giving rise to LS states as illustrated in the right part of Fig. 1.3. In contrast with Valence Bond Theory which is only qualitative, Ligand-Field Theory treats $\triangle_{oct}$ as a free variable and quantifies it by fitting experimental data. In this line, the well-known Tanabe-Sugano diagram pictures the relative energies of all the magnetic states from a d configuration in function of the Racah parameters B, C and $10D_q$ [13, 14].

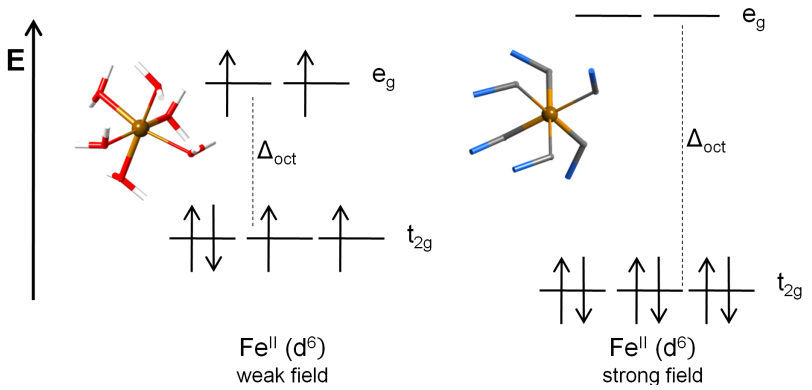

Figure 1.3. Ligand Field Theory LS and HS states for two octahedral Fe^{II} complexes with weak (left) and strong (right) ligand-field.

1.2 The spin-crossover effect

In favourable conditions with ligands of an intermediate field strength, the LS and HS states in TM complexes are close in energy. In this situation, the reversible crossing from LS to HS can be induced by an external stimulus as temperature, pressure or light. In the solid state, intermolecular cooperative interactions can cause hysteresis, meaning that the crossover from LS to HS occurs at a different temperature than the reverse process. This switchable magnetic hysteresis is interesting due to its potential applications in electronic devices such as computer displays or memory [15]. The change of magnetic ground state is known as Spin-Crossover (SCO) [16–18] and was reported for first time in 1931 by Cambi and Szegö when they observed that magnetic moment measurements on tris(*N,N*-disubstituted dithiocarbamate) Fe^{III} derivatives, $[Fe(R_2NCS_2)_3]$, were consistent with a d^5 electronic configuration with one unpaired electron at low temperatures and five at higher temperatures [19, 20]. A detailed description of the history of the research and development of SCO complexes can be found in first chapter of Ref. [21].

The vast majority of SCO complexes consists of a Fe^{II} ion in a N_6 coordination sphere [22]. In this octahedral environment (see Fig. 1.3) the transition from the LS (S=0) to the HS (S=2) state implies the transfer of two electrons from

the (mostly) non-bonding t_{2g} to the anti-bonding e_g orbitals which are empty in the LS (S=0) state. This leads to a weakening of the metal-ligand bond and results in an expansion of the coordination sphere as the most characteristic geometrical changes upon spin crossover. As previously seen, stable HS and LS states are available in TM complexes with d^4-d^7 electronic configurations and they are therefore good candidates to exhibit SCO. However, in most of the TM complexes one of the two states is high up in energy and the change from one to the other cannot be induced by external factors. For that reason, apart from the previous reported Fe^{II} and some Fe^{III} [23] and Co^{II} [24, 25] compounds, few SCO complexes with other metal centres have been reported.

Although it gives a qualitative picture, Ligand Field Theory is not suitable for quantitatively studying SCO. Since the Tanabe-Sugano diagrams only provide vertical excitation energies from the ground state geometry, the description of the potential energy surface of different spin states is out of the scope of this theory. The mentioned structural changes during the SCO make the estimation of absolute energies of the spin states in their equilibrium geometry fundamental to describe SCO. To properly perform a deep study of SCO processes, *ab initio* quantum mechanical models are required. The range of methods for this purpose is wide and will be discussed later.

1.3 Beyond the octahedral ligand-field

The design of novel ligands has been one of the major working lines to control SCO, that is, to widen the hysteresis and push the transition to room temperature [26–29]. Ligand substituents induce electronic and steric changes in the metal coordination sphere which affect the d-orbital splitting and reduce the energy difference between the spin states. This enables the control of SCO by temperature, pressure, light or magnetic fields in a wide range of new and promising SCO complexes with TMs different than Fe and Co and with novel coordination numbers [30].

SCO in square-pyramidal Fe^{II} porphyrinate complexes was firstly reported in 2008 [31]. This spin state switching is unexpected because the absence of a sixth

ligand in the coordination sphere stabilizes the d_{z^2} with respect to the $d_{x^2-y^2}$ orbital favouring an intermediate (S=1) spin state (see Fig. 1.4). However, the metal-ligand bond distance elongation is more pronounced in the axial cyanide ligand than in the rigid porphyrin macrocycle, which reduces the energy gap between the two d-orbitals and results in a HS state at low energy [32, 33]. SCO in a square-pyramidal ligand field has also been reported for Ni^{II} complexes [34].

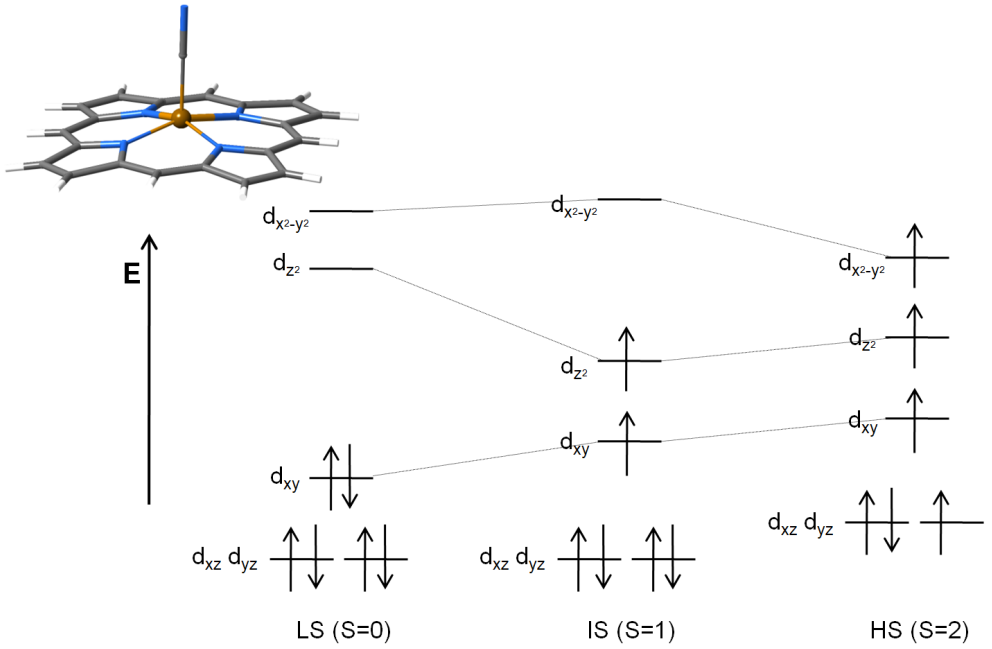

Figure 1.4. Low-spin (S=0), intermediate spin (S=1) and high-spin (S=2) configurations of Fe^{II} in the square-pyramidal coordination sphere of the [Fe(porphyrin)] complex (left, centre and right, respectively).

In the same line, the first square-planar Fe^{II} SCO complex was prepared few years ago [35] and tetrahedral Fe^{II} complexes with SCO have also been reported [36]. In a four-fold coordination sphere, the thermally or photo-induced switch from LS to HS implies the occupation of the d_{xz} and d_{yz} orbitals with two electrons with the consequent elongation of the metal-ligand bond distances [37]. Some Fe^{III} SCO complexes with non-octahedral coordination spheres have also been synthesized [38, 39]. Square-planar Ni^{II} and Co^{II} can as well be made suitable for SCO [40].

1.4 Light-induced excited state spin trapping

In the 1980s, McGarvey et al. [41–43] described how the spin-switch in complexes with thermal SCO is also triggered by light. Irradiation of Fe^{II} and Fe^{III} complexes in solution induces transitions from the LS to the HS state or *viceversa*. The photo-induced HS lifetimes are extremely short at high temperatures but these states become trapped at cryogenic temperatures and can survive for several days [44, 45], fact that coined the concept of Light-Induced Excited State Spin Trapping (LIESST) [46]. Despite the large amount of potential applications based on LIESST, the temperature at which the effect takes place severely limits its use as basis for actual devices. For this reason the relaxation mechanism from the HS to the LS state has been studied in a wide variety of Fe^{II} complexes to increase the LIESST temperature range [47–50].

Upon green-light irradiation, LS Fe^{II} complexes undergo either d-d metal centred or ligand-metal charge transfer (MLCT) spin-allowed transitions. After a double intersystem crossing (ISC) *via* an intermediate-spin state, the system reaches the HS state where it remains trapped at low enough temperature. Irradiation of the system in the HS state with red light induces $^5T_2 \rightarrow {}^5E$ absorption which results in the reconversion to the LS state, and hence, the LIESST is reversible.

The mechanism of light-induced spin crossover in Ni^{II} (d^8) is also well-established. In solvents such as toluene, square-planar Ni-porphyrin in LS (S=0) state undergoes a $S_0 \rightarrow S_{1,2}$ excitation when irradiated with the light of the appropriate wave length. In this case only one ISC is required to reach the HS (S=1) state, which decays *via* ISC to the ground state in approximately 200 ps [51]. However, it is well known that square-planar Ni-porphyrin allows coordination of axial ligands. Concretely, in excited states of this complex the metal centre tends to bind to Lewis basic ligands with lone pair electrons [52, 53]. The photo-induced HS state of Ni-porphyrin in pyridine solution has considerably larger lifetimes without cryogenic temperatures [54]. This variant of LIESST will be extensively studied in Chapter 4.

Most of the theoretical studies about LIESST processes are focused on Fe^{II} [55–59] but, as mentioned before, this effect has also been detected in other

transition metals. Chapter 3 presents a theoretical study of LIESST in the luminescent $[Ru^{II}(bipyridine)_3]^{2+}$, a complex with potential applications in the field of solar energy conversion and information storage [60], among others.

1.5 Coordination-induced spin-crossover

In most of the known SCO complexes, the spin change is induced by external factors that alter structural parameters as metal-ligand bond distances or angles. There are, however, other ways to influence the relative stability of the different spin states. Thermal SCO was reported in 1986 for a Fe^{II} complex with a for that time surprisingly high transition temperature of more 130 K, sign of unusual high stability of the HS state. The LS structure characterization indicated that the metal was six-coordinated but no structural data were available for the HS state [61, 62] until fifteen years later when it was discovered that Fe^{II} becomes seven-coordinated in the HS state [63, 64]. This is an example of how a change of the coordination number provides robust spin states whose stability is hardly affected by temperature or environmental changes. The spin state switch induced by coordination of ligands to the TM complexes is known as Coordination-Induced Spin-Crossover (CISCO).

An interesting example of CISCO can be observed by comparing the Ni^{II} complexes in square-planar, square-pyramidal or octahedral ligand-field. While square-planar coordinations always lead to LS states, the square-pyramidal coordination sphere can result in LS or HS states depending on the ligand-field strength. In an octahedral ligand field Ni^{II} is HS. When a solution of square-planar $[Ni^{II}(porphyrin)]$ (S=0) in water or organic solvents is titrated with a basic ligand such as pyridine or piperidine, these ligands axially coordinate to the Ni^{II} resulting in square-pyramidal or octahedral (S=1) complexes. The LS to HS transition is easily detectable since it is accompanied by a change of colour from red to yellow-ochre [65–67]. CISCO has recently been reported also for Mn^{V} (d^2) complexes [68].

The photo-induced version of CISCO, the so-called Light-Driven Coordination-Induced Spin-State Switching (LD-CISSS) was designed by Herges et al. adding

the photochromic azopyridine ligand to a solution of [Ni^{II}(porphyrin)] [69]. This ligand is stable at both *cis* and *trans* conformations but while at the latter it coordinates to the metal centre, at the former the binding is impeded due to steric hindrance as schematically depicted in Fig. 1.5.

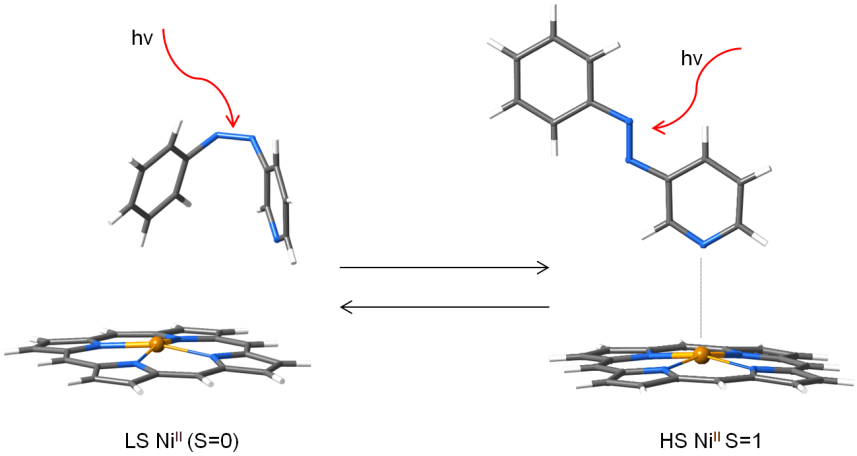

Figure 1.5. Scheme of LD-CISSS in solution with photochromic phenylazopyridine ligand. The axial binding of the ligand in the *cis* conformation to the LS (S=0) Ni^{II} is impeded by steric hindrance (left). The photo-switched *trans* isomer coordinates to the metal inducing the HS (S=1) state (right).

Irradiation of the sample with the appropriate wave-length induces the photoisomerization of the ligand and in this way the spin state of the complex is controlled. Chapter 5 describes the theoretical study of LD-CISSS in a [Ni^{II}-(porphyrin)] complex functionalized with a phenylazopyridine arm. The photoisomerization of this arm induces the change of the metal centre coordination number with the consequent LD-CISSS in solution at room temperature which is fully switchable and induces an exceptionally stable HS state [70–72].

1.6 The role of the ligand: valence tautomerism

A change in the coordination number is not the only way to force a spin-crossover. Photo-active ligands may undergo conformational changes when irradiated, which in turn affects the field exerted by the ligand on the metal

centre and causes a change of the spin moment of the ground state of the complex. This Ligand-Driven Light-Induced Spin-Change (LD-LISC) has been observed in some Fe^{II} complexes [73–76] but has never become very important because of the difficulty to induce large changes in the ligand-field by conformational changes in the ligand.

When the ligand is redox-active with more than one possible oxidation state, it can also behave in a non-innocent fashion transferring electrons to the metal centre and changing its effective charge [77]. In complexes containing a redox-active metal ion coordinated to a redox-active ligand several electronic isomers are possible. These so-called valence tautomers differ in the charge distribution and hence are characterized by different optical, electric and magnetic properties. If the degree of covalence between the metal and the ligand is small and their frontier orbitals are similar in energy, a spin transition implying an electron transfer from the ligand to the metal or *viceversa* can be stimulated by external factors. This switch from one valence tautomer to another is known as valence tautomeric transition. Since the valence tautomeric transition implies a change in the total spin of the system this effect is considered a SCO process [78–80].

Although the most famous transition metal complexes exhibiting VT transitions contain Co [81–84], this effect has also been reported in V, Fe, Ni, Cu, Ru, and Yb complexes [85]. With several accessible oxidation states, Mn is also a good candidate to show VT transitions [86, 87]. As an example, the accessibility to two different valence tautomers for a $[Mn(porphyrin)]^+$ has been reported [88]. The LS (S=2) tautomer is characterized by a Mn^{III} (d^4) coordinated to a closed-shell dianionic porphyrin (see Fig. 1.6 left). Induced by temperature or pressure, one electron is transferred from the porphyrin to the metal. The resulting HS (S=3) state is described as a (S=5/2) reduced Mn^{II} ferromagnetically coupled to an (S=1/2) oxidized anionic porphyrin (see Fig. 1.6 right). Chapter 6 explores the oxidation and spin states of high-valent Mn coordinated to porphyrin derivatives.

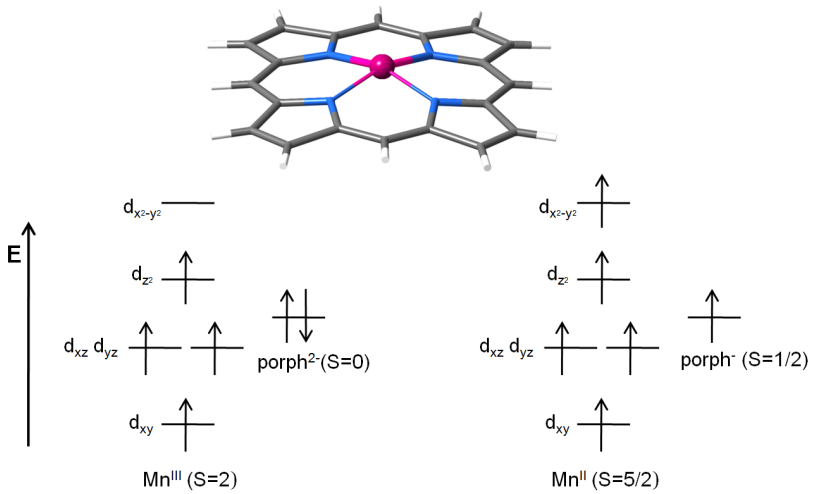

Figure 1.6. Low-spin (S=2) Mn^{III} and high-spin (S=5/2) Mn^{II} configurations of the Mn ion in the square-planar coordination sphere of the [Mn(porphyrin)] complex (left and right respectively).

1.7 Objectives

As already mentioned, the vast majority of the SCO studies focus on octahedral Fe^{II} complexes with FeN_6 core. However, the design of novel ligands has given room to the development of new SCO complexes beyond these standard complexes. Nowadays, the range of TMs and coordination numbers that have been reported to exhibit SCO is wide and the techniques used to induce the effect go further than changes in temperature or pressure, providing better control over the spin of the system and more robust and stable LS and HS states.

Geometrical parameters, relative stabilities and lifetimes of the spin states, spectroscopic data or metal and ligand charges, among others, give fundamental information on the understanding of SCO mechanisms. However, in many cases these data are not accessible from experiment. An obvious example is the oxidation state of the metal centre, which cannot be experimentally determined and has to be assigned indirectly. In other cases intermediate electronic states are unstable and cannot be characterized. In LIESST processes the system

reaches the HS state after a radiation-less relaxation and the energy used to induce the process does not correspond with the HS-LS relative stability. In this sense, theoretical chemistry is a powerful tool which can provide reliable predictions of all this parameters.

The aim of the present work is to get insight in the SCO phenomenon in complexes with less conventional TMs and coordination numbers by means of a computational study. In Chapter 2 the *ab initio* methods used for this purpose are reviewed. Chapters 3 and 4 present a deep study of LIESST in Ru and Ni complexes and report differences in the photochemistry of these metals compared with the well-known Fe^{II} case. The example of a Ni porphyrin functionalized with an azopyridine arm provides insights into the LD-CISSS mechanism in Chapter 5. The spin and oxidation states of imido Mn corrole and corrolazine derivatives are predicted in Chapter 6. The general conclusions of the thesis are exposed in Chapter 7.

1.8 References

[1] M. Swart and M. Costas, Spin States in Biochemistry and Inorganic Chemistry (Wiley, 2015), ISBN 9781118898307.

[2] L. Pauling, J. Am. Chem. Soc. **53**, 3225 (1931).

[3] K. Pierloot, H. Zhao, and S. Vancoillie, Inorg. Chem. **49**, 10316 (2010).

[4] J. Zapata-Rivera, R. Caballol, and C. Calzado, Phys. Chem. Chem. Phys. **13**, 20241 (2011).

[5] J. Zapata-Rivera, R. Caballol, and C. Calzado, J. Comput. Chem. **32**, 1144 (2011).

[6] J. Zapata-Rivera, R. Caballol, and C. Calzado, J. Comput. Chem. **33**, 1407 (2012).

[7] C. Housecroft and A. Sharpe, Inorganic Chemistry (2th ed. (Pearson Education Limited, 2005).

[8] D. Shriver and P. Atkins, Inorganic Chemistry (4th ed. (Oxford University Press, 2006).

[9] I. Bersuker, Electronic Structure and Properties of Transition Metal Compounds (Wiley, 2010), ISBN 9780470920855.

[10] H. Bethe, Ann. Phys. **3**, 133 (1929).

[11] J. Van Vleck, J. Chem. Phys. **3**, 807 (1935).

[12] C. Ballhausen, Introduction to ligand field theory (McGraw-Hill, 1962).

[13] Y. Tanabe and S. Sugano, J. Phys. Soc. Jpn. **9**, 766 (1954).

[14] S. Sugano, Y. Tanabe, and H. Kamimura, Multiplets of transition-metal ions in crystals (Academic Press, 1970).

[15] A. Bousseksou, G. Molnar, and G. Matouzenko, Eur. J. Inorg. Chem. pp. 4353–4369 (2004).

[16] P. Gütlich, Y. Garcia, and H. Goodwin, Chem. Soc. Rev. **29**, 419 (2000).

[17] A. Koudriavtsev and W. Linert, J. Struct. Chem. **51**, 335 (2010).

[18] A. Bousseksou, G. Molnar, L. Salmon, and W. Nicolazzi, Chem. Soc. Rev. **40**, 3313 (2011).

[19] L. Cambi and L. Szegö, B. Deutschen Chemischen Gesellschaft **64**, 2591 (1931).

[20] L. Cambi and L. Szegö, B. Deutschen Chemischen Gesellschaft **66**, 656 (1933).

[21] M. Halcrow, Spin-Crossover Materials: Properties and Applications (Wiley, 2013), ISBN 9781118519325.

[22] A. Gaspar, M. Seredyuk, and P. Guetlich, J. Mol. Struct. **924**, 9 (2009).

[23] M. Nihei, T. Shiga, Y. Maeda, and H. Oshio, Coord. Chem. Rev. **251**, 2606 (2007).

[24] I. Krivokapic, M. Zerara, M. Daku, A. Vargas, C. Enachescu, C. Ambrus, P. Tregenna-Piggott, N. Amstutz, E. Krausz, and A. Hauser, Coord. Chem. Rev. **251**, 364 (2007).

[25] S. Hayami, Y. Komatsu, T. Shimizu, H. Kamihata, and Y. Lee, Coord. Chem. Rev. **255**, 1981 (2011).

[26] J. Kitchen and S. Brooker, Coord. Chem. Rev. **252**, 2072 (2008).

[27] M. Halcrow, Coord. Chem. Rev. **253**, 2493 (2009).

[28] I. Gass, S. Batten, C. Forsyth, B. Moubaraki, C. Schneider, and K. Murray, Coord. Chem. Rev. **255**, 2058 (2011).

[29] J. Olguin and S. Brooker, Coord. Chem. Rev. **255**, 203 (2011).

[30] P. Gütlich, Eur. J. Inorg. Chem. pp. 581–591 (2013).

[31] J. Li, R. Lord, B. Noll, M.-H. Baik, C. Schulz, and W. Scheidt, Angew. Chem. Int. Ed. **47**, 10144 (2008).

[32] J. Li, Q. Peng, A. Barabanschikov, J. Pavlik, E. Alp, W. Sturhahn, J. Zhao, J. Sage, and W. Scheidt, Inorg. Chem. **51**, 11769 (2012).

[33] J. Cirera and S. Alvarez, Dalton Trans. **42**, 7002 (2013).

[34] H. Ma, J. Petersen, V. Young, Jr., G. Yee, and M. Jensen, J. Am. Chem. Soc. **133**, 5644 (2011).

[35] J. Scepaniak, T. Harris, C. Vogel, J. Sutter, K. Meyer, and J. Smith, J. Am. Chem. Soc. **133**, 3824 (2011).

References

[36] H.-J. Lin, D. Siretanu, D. Dickie, D. Subedi, J. Scepaniak, D. Mitcov, R. Clerac, and J. Smith, J. Am. Chem. Soc. **136**, 13326 (2014).

[37] C. Mathoniere, H.-J. Lin, D. Siretanu, R. Clerac, and J. Smith, J. Am. Chem. Soc. **135**, 19083 (2013).

[38] A. Bowman, C. Milsmann, E. Bill, Z. Turner, E. Lobkovsky, S. DeBeer, K. Wieghardt, and P. Chirik, J. Am. Chem. Soc. **133**, 17353 (2011).

[39] S. Mossin, B. Tran, D. Adhikari, M. Pink, F. Heinemann, J. Sutter, R. Szilagyi, K. Meyer, and D. Mindiola, J. Am. Chem. Soc. **134**, 13651 (2012).

[40] K. Ono, M. Yoshizawa, M. Akita, T. Kato, Y. Tsunobuchi, S. Ohkoshi, and M. Fujita, J. Am. Chem. Soc. **131**, 2782 (2009).

[41] J. McGarvey and I. Lawthers, J. Chem. Soc. Chem. Commun. pp. 906–907 (1982).

[42] I. Lawthers and J. McGarvey, J. Am. Chem. Soc. **106**, 4280 (1984).

[43] J. McGarvey, I. Lawthers, K. Heremans, and H. Toftlund, J. Chem. Soc. Chem. Commun. pp. 1575–1576 (1984).

[44] J. Jeftic and A. Hauser, J. Phys. Chem. B **101**, 10262 (1997).

[45] J. Jeftic, R. Hinek, S. Capelli, and A. Hauser, Inorg. Chem. **36**, 3080 (1997).

[46] S. Decurtins, P. Gutlich, K. Hasselbach, A. Hauser, and H. Spiering, Inorg. Chem. **24**, 2174 (1985).

[47] J. Letard, P. Guionneau, L. Rabardel, J. Howard, A. Goeta, D. Chasseau, and O. Kahn, Inorg. Chem. **37**, 4432 (1998).

[48] M. Halcrow, Chem. Soc. Rev. **37**, 278 (2008).

[49] N. Moisan, M. Servol, M. Lorenc, A. Tissot, M.-L. Boillot, H. Cailleau, S. Koshihara, and E. Collet, C. R. Chimie **11**, 1235 (2008).

[50] G. Craig, J. Sanchez Costa, S. Teat, O. Roubeau, D. Yufit, J. Howard, and G. Aromi, Inorg. Chem. **52**, 7203 (2013).

[51] L. Chen, X. Zhang, E. Wasinger, K. Attenkofer, G. Jennings, A. Muresan, and J. Lindsey, J. Am. Chem. Soc. **129**, 9616 (2007).

[52] D. Kim and T. Spiro, J. Am. Chem. Soc. **108**, 2099 (1986).

[53] H. Eom, S. Jeoung, D. Kim, J. Ha, and Y. Kim, J. Phys. Chem. A **101**, 3661 (1997).

[54] M. Shelby, M. Mara, and L. Chen, Coord. Chem. Rev. **277**, 291 (2014).

[55] J. Letard, J. Mater. Chem. **16**, 2550 (2006).

[56] B. Ordejon, C. de Graaf, and C. Sousa, J. Am. Chem. Soc. **130**, 13961 (2008).

[57] C. de Graaf and C. Sousa, Chem. Eur. J. **16**, 4550 (2010).

[58] A. Cannizzo, C. J. Milne, C. Consani, W. Gawelda, C. Bressler, F. van Mourik, and M. Chergui, Coord. Chem. Rev. **254**, 2677 (2010).

[59] C. de Graaf and C. Sousa, Int. J. Quantum Chem. **111**, 3385 (2011).

[60] A. Cannizzo, F. van Mourik, W. Gawelda, G. Zgrablic, C. Bressler, and M. Chergui, Angew. Chem. Int. Ed. **45**, 3174 (2006).

[61] S. Nelson, P. Mcllroy, C. Stevenson, E. Konig, G. Ritter, and J. Waigel, J. Chem. Soc. Dalton Trans. pp. 991–995 (1986).

[62] E. Konig, G. Ritter, J. Dengler, and S. Nelson, Inorg. Chem. **26**, 3582 (1987).

[63] S. Hayami, Z. Gu, Y. Einaga, Y. Kobayasi, Y. Ishikawa, Y. Yamada, A. Fujishima, and O. Sato, Inorg. Chem. **40**, 3240 (2001).

[64] P. Guionneau, F. Le Gac, A. Kaiba, J. Costa, D. Chasseau, and J.-F. Letard, Chem. Commun. pp. 3723–3725 (2007).

[65] S. Thies, C. Bornholdt, F. Koehler, F. Soennichsen, C. Naether, F. Tuczek, and R. Herges, Chem. Eur. J. **16**, 10074 (2010).

[66] M. Dommaschk, F. Gutzeit, S. Boretius, R. Haagc, and R. Herges, Chem. Commun. **50**, 12476 (2014).

[67] M. Dommaschk, V. Thoms, C. Schuett, C. Naether, R. Puttreddy, K. Rissanen, and R. Herges, Inorg. Chem. **54**, 9390 (2015).

[68] H. Kropp, A. Scheurer, F. Heinemann, J. Bendix, and K. Meyer, Inorg. Chem. **54**, 3562 (2015).

[69] S. Thies, H. Sell, C. Schuett, C. Bornholdt, C. Naether, F. Tuczek, and R. Herges, J. Am. Chem. Soc. **133**, 16243 (2011).

References

[70] S. Venkataramani, U. Jana, M. Dommaschk, F. Soennichsen, F. Tuczek, and R. Herges, Science **331**, 445 (2011).

[71] G. Alcover-Fortuny, C. de Graaf, and R. Caballol, Phys. Chem. Chem. Phys. **17**, 217 (2015).

[72] M. Dommaschk, M. Peters, F. Gutzeit, C. Schuett, C. Naether, F. Soennichsen, S. Tiwar, C. Riedel, S. Boretius, and R. Herges, J. Am. Chem. Soc. **137**, 7552 (2015).

[73] J. Kolb, M. Thomson, M. Novosel, K. Senechal-David, E. Riviere, M.-L. Boillot, and H. Roskos, C. R. Chimie **10**, 125 (2007).

[74] M.-L. Boillot, S. Pillet, A. Tissot, E. Riviere, N. Claiser, and C. Lecomte, Inorg. Chem. **48**, 4729 (2009).

[75] Y. Hasegawa, S. Kume, and H. Nishihara, Dalton Trans. pp. 280–284 (2009).

[76] A. Bannwarth, S. Schmidt, G. Peters, F. Soennichsen, W. Thimm, R. Herges, and F. Tuczek, Eur. J. Inorg. Chem. pp. 2776–2783 (2012).

[77] W. Kaim, Inorg. Chem. **50**, 9752 (2011).

[78] E. Evangelio and D. Ruiz-Molina, Eur. J. Inorg. Chem. pp. 2957–2971 (2005).

[79] E. Evangelio and D. Ruiz-Molina, C. R. Chimie **11**, 1137 (2008).

[80] O. Sato, J. Tao, and Y.-Z. Zhang, Angew. Chem. Int. Ed. **46**, 2152 (2007).

[81] A. Dei, D. Gatteschi, C. Sangregorio, and L. Sorace, Acc. Chem. Res. **37**, 827 (2004).

[82] O. Sato, A. Cui, R. Matsuda, J. Tao, and S. Hayami, Acc. Chem. Res. **40**, 361 (2007).

[83] F. Senn, M. Zlatar, M. Gruden-Pavlovic, and C. Daul, Monatsh. Chem. **142**, 593 (2011).

[84] A. Witt, F. Heinemann, and M. Khusniyarov, Chem. Sci. **6**, 4599 (2015).

[85] T. Tezgerevska, K. Alley, and C. Boskovic, Coord. Chem. Rev. **268**, 23 (2014).

[86] M. Lynch, D. Hendrickson, B. Fitzgerald, and C. Pierpont, J. Am. Chem. Soc. **103**, 3961 (1981).

[87] A. Caneschi and A. Dei, Angew. Chem. Int. Ed. **37**, 3005 (1998).

[88] M. Kepenekian, V. Vetere, B. Le Guennic, P. Maldivi, and V. Robert, Chem. Eur. J. **17**, 12045 (2011).

Chapter 2

Theoretical background

In non-relativistic quantum mechanics a many-particle system in a stationary state is described by the Ψ_n wave function, solution of the time-independent Schrödinger equation

$$\hat{H}\Psi_n = E_n\Psi_n \tag{2.1}$$

$\hat{H}$ is the Hamiltonian operator and Ψ_n and E_n are respectively the eigenfunction and eigenvalue of state n. In atomic units, $\hat{H}$ has the following form:

$$\hat{H} = -\frac{1}{2}\sum_i \nabla_i^2 + \sum_{i<j}\frac{1}{r_{ij}} - \sum_{i,A}\frac{Z_A}{r_{iA}} - \frac{1}{2}\sum_A \frac{\nabla_A^2}{M_A} + \sum_{A<B}\frac{z_A z_B}{R_{AB}}, \tag{2.2}$$

where A and B subscripts refer to nuclei while i and j to electrons. The five terms correspond respectively to the kinetic energy of the electrons ($\hat{T}_e$), Coulomb repulsion between electrons ($\hat{V}_{ee}$) and attraction between electrons and nuclei ($\hat{V}_{Ne}$), kinetic energy of nuclei ($\hat{T}_N$) and Coulomb repulsion between nuclei ($\hat{V}_{NN}$).

The Hamiltonian can be expressed as

$$\hat{H} = \hat{H}_{elec} + \hat{H}_{nucl} \tag{2.3}$$

accounting for electronic ($\hat{H}_{elec} = \hat{T}_e + \hat{V}_{ee} + \hat{V}_{Ne}$) and nuclear ($\hat{H}_{nucl} = \hat{T}_N + \hat{V}_{NN}$) terms. Since nuclei are heavier than electrons, electronic movement is

faster than the nuclear one and can be neglected in a system in a stationary state. The nuclear repulsion $\hat{V}_{NN}$ is in this case a parameter and its contribution to the total energy added afterwards. This separation of nuclear and electronic motion is known as Born-Oppenheimer approximation, and in this picture the time-independent Schrödinger equation is reduced to the electronic problem

$$\hat{H}_{elec}\Phi_{elec}(r, R) = E_{elec}(R)\Phi_{elec}(r, R), \tag{2.4}$$

and the total energy is

$$E_{tot} = E_{elec}(R) + V_{NN}(R). \tag{2.5}$$

As a consequence of this separation the wave function can be expressed as

$$\Psi(r, R) = \Phi_{elec}(r, R)\chi_{nucl}(R). \tag{2.6}$$

In the Born-Oppenheimer approximation the electronic Schrödinger equation considers the motion of electrons within the field of nuclei with fixed position and both electronic wave function and energy depend parametrically on the nuclear coordinates. Hereinafter we will assume this approximation and we will focus on the electronic problem.

The exact solution of the electronic time-independent Schrödinger equation is only known for single-electron systems. The two-electron repulsion term makes this equation unsolvable for many-electron systems and only approximate solutions can be obtained. To this purpose, a common approach is based on representing the N-electron wave function as an expansion of Slater determinants

$$\Psi = \sum_k c_k\Phi_k. \tag{2.7}$$

Slater determinants (Φ_k) consist in antisymmetrized products of N one-electron wave functions (χ) ensuring the antisymmetry of the wave function:

$$\Phi_k = \det(\chi_a(1)\chi_b(2)...). \tag{2.8}$$

χ are spin-orbitals and are obtained as products of spatial and spin functions.

In this approach the exact wave function is given as a complete expansion of all the Slater determinants which can be generated distributing the N electrons in all possible ways over the orbitals in a given basis set. In this case, equation 2.7 refers to a full Configuration Interaction calculation (FCI). This is in general not possible and the set of determinants included in the expansion must be truncated according to different approximations.

Among the methods to truncate the linear expansion (equation 2.7), the Hartree-Fock (HF) approximation is the crudest one since it represents the many-electron wave function with a single Slater determinant. The variational principle leads to a system of eigenvalues and eigenfunction equations which is solved iteratively until convergence. These equations have monoelectronic character and the operator is known as the Fock operator. The motion of one electron is described in the field of the nuclei and the average field of the rest of electrons and therefore, the electron-electron interaction is taken into account only in an average way. The method is also known as Self-Consistent-Field (SCF) [1].

2.1 Electron correlation

Since HF method describes the interaction of the electrons in an average way, the motion of one specific electron does not affect the motion of the rest of electrons, in other words the motion of the electrons is uncorrelated. However, due to the coulombic repulsion, each electron presents a spatial region known as Coulomb hole in which the probability of finding another electron rapidly goes to zero. The absence of the Coulomb hole in the HF approximation to the N-electron wave function makes that the electron-electron repulsion is overestimated. The difference between the exact energy and the Hartree-Fock energy is traditionally defined as the correlation energy

$$\mathrm{E_{corr}} = \mathrm{E_{exact}} - \mathrm{E_{HF}}. \tag{2.9}$$

Electron correlation has usually been classified in dynamic and non-dynamic although there is not an exact differentiation between them. The dynamic electron correlation is related to the fact that beyond the mean-field, the electrons

avoid each other more effectively and partially restitute the Coulomb hole, while the non-dynamic correlation is due to the existence of several low-lying nearly degenerate determinants.

The so-called *post*-Hartree-Fock methods aim to restore the Coulomb hole by including part of the electron correlation. The expansion with more Slater determinants makes the wave function multideterminantal and gives it flexibility. If these determinants are classified in terms of single (S), double (D), triple (T) excitations, equation 2.7 can be re-expressed as follows:

$$\Psi = c_0\Phi_0 + \sum_S c_S\Phi_S + \sum_D c_D\Phi_D + \sum_T c_T\Phi_T + ... \qquad (2.10)$$

The HF determinant Φ_0 is called the reference determinant. Systems with near degeneracies are not well described even qualitatively within the HF approximation and a multiconfigurational function has to be used as the reference, as discussed in Sections 2.2 and 2.3.

In variational methods the expansion coefficients are obtained by diagonalizing the corresponding Hamiltonian matrix. Either in single reference or in multiconfigurational schemes, Equation 2.10 is often truncated to the third term, including only single and double excitations in the CI space (CISD), since these excitations are the most relevant contributions to the correlation energy. Other truncations can be defined according to the specific aim of the calculation. This is the case of the Difference-Dedicated Configuration Interaction method (DDCI) [2, 3], which is used in Chapter 6, and is designed to accurately estimate energy differences. In this method a multiconfigurational function is taken as reference and the CI space is expanded up to double excitations but many of them are excluded on the basis of perturbation theory criteria. In any case, the truncation must be used with caution since it can lead to an incorrect dependence of the energy on the number of electrons known as size-consistency error. Alternatively, the linear expansion of configurations can be avoided generating the wave function with an exponential *Ansatz*, which is called Coupled Cluster approach [4–7] and is exempt of size-consistency error.

An alternative to the variational determination of the expansion coefficients and the correlation energy is Perturbation Theory.

2.2 Multiconfigurational self-consistent field

Some systems present (nearly) degenerate electronic configurations in their electronic structure. This is the case for certain transition metals where the $d^n s^2$, $d^{n+1} s^1$ and d^{n+2} configuration lead to multiplets with similar energies. Other examples of marked multiconfigurational character of the wave function can be found in electronically excited states or systems far away from their equilibrium geometry. Such cases are obviously not well described with approaches based on a monoconfigurational reference wave function and a more flexible wave function is mandatory.

The multiconfigurational self-consistent field (MCSCF) method [8, 9] is designed to construct wave functions to recover the largest part of the non-dynamic electron correlation, that is, to take into account the presence of (nearly) degenerate electronic configurations from the very beginning in a rigorous manner. Typically, the wave function is written as a relatively short CI expansion that contains the most important electronic configurations. The method optimizes both the CI coefficients and the orbital expansion coefficients to avoid any bias towards one of the electronic configurations. In contrast to the monoconfigurational methods, the occupation numbers of the orbitals are no longer restricted to 0, 1 or 2, but become non-integer and can take any value between 0 and 2, depending on the weight in the final wave function of the configurations in which these orbitals are occupied.

Among the different MCSCF methods, the most widely used is the complete active space self-consistent field (CASSCF) approach [10, 11]. The molecular orbital space is divided in three subspaces (see Fig. 2.1): the inactive space contains the orbitals that are doubly occupied in all the configurations of the wave function; the virtual space contains the orbitals that are empty in all configurations; and finally, the active space, which contains the orbitals with variable occupations. The multiconfigurational wave function is constructed as a linear combination of Slater determinants in which the active electrons[1] are distributed over the active orbitals in all possible ways compatible with the

[1] The electrons that are not in the inactive space. The number of active electrons is defined as the total number of electrons minus twice the number of inactive orbitals.

spin multiplicity and the spatial symmetry of the electronic state under study. For this reason, CASSCF can be seen as a full CI in the active space.

The main difficulty of CASSCF lies in the choice of the active space, an inadequate choice can easily lead to unphysical results. Unfortunately, there is no generally applicable rule for selecting the active orbitals. Different systems need different active spaces and the limitation of the size of the active space to approximately 15 orbitals makes it impossible to use CASSCF as a black-box method, chemical knowledge is essential to ensure a correct treatment of the electronic structure. It must be stated that the experience gained over the years with the application of CASSCF to a wide variety of systems established some general guidelines for the proper choice of the active space [12–14].

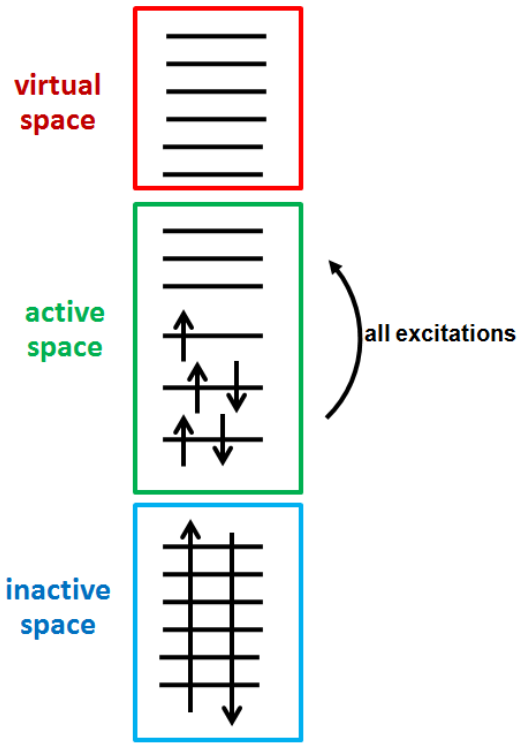

Figure 2.1. Schematic representation of the classification in three subspaces of the molecular orbitals in a CASSCF calculation.

2.3 Multiconfigurational reference perturbation theory

While CASSCF can give a rather precise description of the non-dynamic electron correlation, it is practically impossible to include the effect of the dynamic correlation. To further improve the theoretical description of the electronic structure, multiconfigurational reference perturbation theory (MRPT) can be applied to account for the latter effect [15]. Such methods offer an excellent balance between computational effort and accuracy. In perturbative approaches, in a first step approximate zeroth order solutions of the energy and the wave function are determined and fist order, second order, etc. corrections are added from series developments in a further step.

The complete active space second order perturbation theory (CASPT2) implementation of MRPT [16] is one of the most widely applied schemes to improve upon the CASSCF wave function. The zeroth order Hamiltonian ($H^{(0)}$) is defined as a sum of Fock-type operators (effective one-electron operators) that reduces exactly to the Møller-Plesset [17] choice for $H^{(0)}$ in the limit of zero active orbitals. The first order wave function is constructed by applying single and double excitation operators on the CASSCF wave function (the reference or zeroth order wave function) as a whole. This so-called contracted manner to produce the first order wave function greatly reduces the number of parameters to be determined but makes it very difficult to estimate the influence of dynamic correlation on the relative importance of the different configurations in the CAS.

The denominator of the second order correction to the energy is given by the difference of the expectation values of $H^{(0)}$ of the CAS wave function and a configuration outside the CAS. The approximate nature of $H^{(0)}$ makes that this denominator can become very small, causing a breakdown of the perturbative estimate for the energy. Including this configuration in the CAS is the most rigorous solution to this problem but not always possible due to the limitation on the size of the CAS. A pragmatic solution to this intruder state problem is to add an artificial shift to the denominator and later correct the so-obtained estimate for the application of the shift [18, 19].

Among the other implementations of MRPT it is worth to mention the n-electron valence state second order perturbation theory (NEVPT2) [20]. This method completely eliminates the intruder state problem by using a zeroth order Hamiltonian with two-electron terms among the active orbitals. The first order wave function can be constructed in a similar way as for CASPT2 although it also offers an even more compact expansion for further speed-up.

2.4 Density functional methods

2.4.1 Density functional theory

The original idea of density functional theory (DFT) was to circumvent the necessity of the construction of an N-electron wave function to obtain information about the energy (and other properties) of the system and use the much simpler electronic density instead. The advantage of this approach is obvious; while the N-electron wave function depends on 4N coordinates (N times three spatial plus one spin coordinates), the electron density is the square of the wave function integrated over N-1 spatial coordinates and only depends on one electron coordinates. Therefore, the complexity of a density based approach is in principle independent on the system size. Although it has been formally proven that one can calculate the energy from the density, the problem of this approach is of course that the exact functional that connects the electron density with the energy is unknown.

Considering that the nuclear repulsion is constant in the Born-Oppenheimer approximation, the density functional to calculate the energy $E[\rho]$ can be split in a kinetic energy $T[\rho]$, a electron-nucleus attraction $V_{Ne}[\rho]$ and a electron-electron repulsion $V_{ee}[\rho]$ term. The latter term can be separated in a Coulomb $J[\rho]$ and a exchange $K[\rho]$ part. While $V_{Ne}[\rho]$ is defined as

$$V_{Ne}[\rho] = -\sum_{a}^{N_{nuclei}} \int \frac{Z_a(R_a)\rho(r)}{|R_a - r|} dr, \tag{2.11}$$

and the Coulomb part of the electron-electron repulsion functional as

$$\mathrm{J}[\rho] = \frac{1}{2}\int\int \frac{\rho(\mathrm{r})\rho(\mathrm{r}')}{|\mathrm{r}-\mathrm{r}'|}\mathrm{d}\mathrm{r}\mathrm{d}\mathrm{r}', \tag{2.12}$$

there are no exact expressions available for the kinetic energy and the exchange part. The first attempts to define expressions for these unknown parts of the functional were based on the exact solution of the uniform electron gas. Thomas and Fermi derived the $\mathrm{T}[\rho]$ for this model system, establishing what is known as Thomas-Fermi DFT. Despite being associated with the name of Dirac [21], it was Bloch [22] who derived an expression for $\mathrm{K}[\rho]$ constituting the Thomas-Fermi-Dirac model. However, this approach is far too approximate and can in fact not even describe any bond formation. In other words, molecules are unstable in this model. The addition of higher order terms depending on the gradient of ρ does not lead to significant improvements.

Hohenberg and Kohn laid the rigorous foundations for DFT [23] with two theorems. In the first one –known as existence theorem– they showed via *reductio ad absurdum* that in a non-degenerate ground state the density entirely determines the external potential. Let us suppose that this is not true and we have the exact density ($\rho(\mathrm{r})$) of a non-degenerate ground state and that this $\rho(\mathrm{r})$ can be obtained from two different external potentials ($\mathrm{V}_1(\mathrm{r})$ and $\mathrm{V}_2(\mathrm{r})$). These two external potentials generate two different Hamiltonians $\hat{\mathrm{H}}_1$ and $\hat{\mathrm{H}}_2$ which at the same time generate two different wave functions Ψ_1 and Ψ_2. Calculating the expected value of the energy of Ψ_2 with $\hat{\mathrm{H}}_1$ and of Ψ_1 with $\hat{\mathrm{H}}_2$, from the variational principle we have that

$$\mathrm{E}_1 < \langle\Psi_2|\hat{\mathrm{H}}_1|\Psi_2\rangle = \langle\Psi_2|\hat{\mathrm{H}}_2|\Psi_2\rangle + \langle\Psi_2|\hat{\mathrm{H}}_1 - \hat{\mathrm{H}}_2|\Psi_2\rangle = \mathrm{E}_2 - \int(\rho(\mathrm{r})[\mathrm{V}_1(\mathrm{r}) - \mathrm{V}_2(\mathrm{r})]\mathrm{dv}_1(\mathrm{r}) \tag{2.13}$$

$$\mathrm{E}_2 < \langle\Psi_1|\hat{\mathrm{H}}_2|\Psi_1\rangle = \langle\Psi_1|\hat{\mathrm{H}}_1|\Psi_1\rangle + \langle\Psi_1|\hat{\mathrm{H}}_2 - \hat{\mathrm{H}}_1|\Psi_1\rangle = \mathrm{E}_1 - \int(\rho(\mathrm{r})[\mathrm{V}_2(\mathrm{r}) - \mathrm{V}_1(\mathrm{r})]\mathrm{dv}_2(\mathrm{r}). \tag{2.14}$$

Summing up equations (2.13) and (2.14) we arrive to

$$\mathrm{E}_1 + \mathrm{E}_2 < \mathrm{E}_2 + \mathrm{E}_1, \tag{2.15}$$

which is inconsistent and proves that $\rho(\mathrm{r})$ of a non-degenerate ground state associated to $\mathrm{V}(\mathrm{r})$ cannot be reproduced with a different potential. Therefore,

providing the number of electrons and the external potential, electron density determines the Hamiltonian operator and the wave function of the ground state.

In their second theorem, Hohenberg and Kohn established how to predict the electron density of a system. In a similar way as the molecular orbitals, $\rho(\mathrm{r})$ is governed by a variational principle. Given a trial electron density $\rho_{\mathrm{trial}}(\mathrm{r})$ which defines $\hat{\mathrm{H}}_{\mathrm{trial}}$ and Ψ_{trial},

$$\langle\Psi_{\mathrm{trial}}|\hat{\mathrm{H}}_{\mathrm{trial}}|\Psi_{\mathrm{trial}}\rangle = \mathrm{E}_{\mathrm{trial}} \geq \mathrm{E}_0 \tag{2.16}$$

where E_0 is the exact energy of the system. Following this principle, the exact density will be the one which minimizes the energy.

A major step forward was made by Kohn and Sham by writing $\mathrm{T}[\rho]$ as the sum of the kinetic energy of non-interacting particles $\mathrm{T_S}[\rho]$ and the remainder $\mathrm{T_{xc}}[\rho]$ [24]. The first contribution is by far the largest and can be calculated exactly by introducing a set of orbitals to decompose the electron density

$$\mathrm{T_S}[\rho] = \sum_{\mathrm{i}=1}^{\mathrm{N_{elec}}} \langle\phi_{\mathrm{i}}| - \frac{1}{2}\hat{\nabla}^2|\phi_{\mathrm{i}}\rangle. \tag{2.17}$$

The difference between the exact kinetic energy with the electrons interacting and $\mathrm{T_S}$ is very small and is absorbed in the exchange-correlation $\mathrm{V_{xc}}[\rho]$ correction term, which also includes the difference between $\mathrm{V_{ee}}[\rho]$ and $\mathrm{J}[\rho]$,

$$\mathrm{V_{xc}}[\rho] = (\mathrm{T}[\rho] - \mathrm{T_S}[\rho]) + (\mathrm{V_{ee}}[\rho] - \mathrm{J}[\rho]). \tag{2.18}$$

In this way, the only part of the energy functional that has to be approximated is the exchange-correlation term

$$\mathrm{E_{DFT}}[\rho] = \mathrm{T_S}[\rho] + \mathrm{V_{Ne}}[\rho] + \mathrm{J}[\rho] + \mathrm{V_{xc}}[\rho]. \tag{2.19}$$

Orbital-free models can be considered as 'true' DFT approaches that only depend on four variables, but the extreme difficulties on finding an accurate functional for the kinetic energy makes this approach unviable nowadays. On

the other hand, the use of orbitals in Kohn-Sham DFT increases the number of variables to 4N but the improvement in the description of the kinetic energy provides computational chemists with a reliable and relatively cheap procedure to study the electronic structure of a wide variety of systems.

In the KS context the different DFT methods are characterized by the choice of how the functional for $V_{xc}[\rho]$ is represented. The simplest model, known as Local Density Approximation (LDA) [25, 26] considers the density to be constant in small intervals around r. It uses the expression of the uniform electron gas for the exchange part of V_{xc}, while a more elaborate expression is used for the correlation part. LDA can be extended to open-shell considering the α and β densities separately in the Local Spin Density Approximation (LSDA).

Next step to improve this representation is to take into account that the local density locally changes by making $V_{xc}[\rho]$ also dependent on the derivative of ρ, which is known as the Generalized-Gradient Approximation (GGA) [27]. Over the years a large number of GGA functionals have been published. Often the acronym used to identify the functional reflects the fact that V_{xc} can be written as an exchange part V_x and a correlation part V_c. For example, the BLYP functional accounts for exchange interaction with the Becke functional for exchange and uses the Lee, Yang and Parr correlation functional. Inclusion of not only the gradient but also the second derivative of the density results in the so-called meta-GGA functionals.

Finally, hybrid functionals include exact exchange energy as calculated in a standard HF calculation, with the difference that here Kohn-Sham orbitals are used. PBE0 and B3LYP [28, 29] are of this class and have become the most used functionals during the last decades, since they perform very well analyzing problems in general chemistry.

2.4.2 Time-dependent density functional theory

Although DFT has been proven to be accurate and rather cost-effective for the description of electronic ground states, the treatment of excited states is

not covered by the formulation of DFT discussed so far. In this sense, Time-Dependent DFT (TD-DFT) extends the Hohenberg-Kohn-Sham DFT to cases in which the stationary ground state is exposed to a time-dependent perturbation and the external potential is modified.

TD-DFT is based on Runge and Gross theorem [30] which, similarly to Hohenberg -Kohn, shows the existence of a unique correspondence between the time-dependent density and the time-dependent potential. In other words, ρ(r,t) and the initial wave function Ψ_0 at some time t_0 determine V_{ext}(r,t) which in consequence is a functional of the time-dependent density. Moreover, ρ(r,t) fixes the number of electrons of the system, which together with the external potential define the time-dependent Hamiltonian operator. Since this is true both for the real system and a system of non-interacting electrons, the equation

$$i\frac{\partial}{\partial t}\psi_i(r,t) = [-\frac{\hat{\nabla}^2}{2} + \hat{J}(r,t) + \hat{V}_{ext}(r,t) + \hat{V}_{xc}(r,t)]\psi_i(r,t) \tag{2.20}$$

is the T-D Kohn-Sham equation, where $\hat{J}$(r,t) is the classical electrostatic potential and $\hat{V}_{ext}$(r,t) includes the nucleus-electron interaction and any other potential which depends on time. Since approximations for $\hat{V}_{xc}$(r,t) are still under development, the same exchange-correlation potential as in time-independent DFT is used, which is known as adiabatic approximation.

The dynamic polarizability α is the tendency of a charge distribution to be distorted due to an external electric field ($\varepsilon(t) = \varepsilon\cos(\omega t)$). TD-DFT allows us to calculate the difference between the permanent dipole moment and a time-dependent dipole moment when the system is under the influence of a small dynamic perturbation. This induced dipole moment is a linear term defined as

$$\triangle\mu(t) = \int \alpha(t - t')\varepsilon(t')dt' \tag{2.21}$$

if the time-dependent potential is weak and the Linear-Response (LR) theory can be applied neglecting higher-order terms. After a Fourier transformation Eq. 2.21 becomes

$$\triangle\mu(\omega) = \alpha(\omega)\varepsilon(\omega) \tag{2.22}$$

and the dynamic polarizability is

$$\alpha(\omega) = \sum_{\mathrm{I}\neq 0} \frac{f_{\mathrm{I}}}{\omega_{\mathrm{I}}^2 - \omega^2} \tag{2.23}$$

where ω_{I} is defined as the vertical excitation energy (ω_{I} = $\mathrm{E_I}$ - $\mathrm{E_0}$) and f_{I} is the corresponding oscillator strength.

Therefore, vertical excitation energies and oscillator strengths can be obtained from the poles of the dynamic polarizability with LR TD-DFT. Since the response function has poles in all the excitation energies of a system it contains the required information to calculate all the excited states. For further information about TD-DFT the reader is referred to reviews [31–34] which provide deeper information about this methodology.

2.5 Estimation of intersystem crossing rates

As seen in Chapter 1 some transition metal complexes exhibit spin-crossover induced by light. In these systems the absorption of light induces an excitation to a state with the same spin multiplicity as the ground state. In such cases spin-crossover implies the relaxation from the excited state to a state with different spin multiplicity. This process is known as intersystem crossing (ISC) and its rate will determine the magnetic properties of the complex. In this work, Fermi's golden rule is used to compute ISC rates [35–37]. The expression to calculate ISC rate constants ($\mathrm{k_{ISC}}$) from Fermi's golden rule is

$$\mathrm{k_{ISC}} = 2\pi \sum_{\mathrm{k}} |\, \langle \Psi_{\mathrm{I}}, \{\nu_{\mathrm{Ia}}\} | \hat{\mathrm{H}}_{\mathrm{SO}} | \Psi_{\mathrm{F}}, \{\nu_{\mathrm{Fk}}\} \rangle \,|^2 \delta(\mathrm{E_{Ia}} - \mathrm{E_{Fk}}) \tag{2.24}$$

where Ψ_{I} and Ψ_{F} are electronic wave functions of the initial and final states, and $\{\nu_{(\mathrm{I,F})\mathrm{i}}\}$ represents the collection of vibrational wave functions of the initial and final states. $\hat{\mathrm{H}}_{\mathrm{SO}}$ is the spin-orbit coupling operator. Assuming that SO coupling is independent of the vibrational level (Condon approximation), equation 2.24 can be written as a product of the electronic and the vibrational part

$$\mathrm{k_{ISC}} = 2\pi |\, \langle \Psi_{\mathrm{I}} | \hat{\mathrm{H}}_{\mathrm{SO}} | \Psi_{\mathrm{F}} \rangle \,|^2 \times \sum_{\mathrm{k}} |\, \langle \{\nu_{\mathrm{Ia}}\} | \{\nu_{\mathrm{Fk}}\} \rangle \,|^2 \delta(\mathrm{E_{Ia}} - \mathrm{E_{Fk}}). \tag{2.25}$$

Equation 2.25 corresponds to the time-independent approach and becomes computationally very demanding for large systems since it requires the calculation of a huge amount of Franck-Condon integrals. Instead, when Fermi's golden rule is transformed to the time domain, that is, adopting the Heisenberg picture, k_{ISC} can be calculated from a time integration

$$k_{ISC} = |\langle \Psi_I | \hat{H}_{SO} | \Psi_F \rangle|^2 \int_{-\infty}^{\infty} dt G(t) e^{it(\triangle E_{IF} + (\frac{1}{2})Tr\Omega_1}, \qquad (2.26)$$

where the time-dependent correlation function G(t) contains information related to the vibrational frequencies and the normal coordinates of the initial and final states and Ω_1 is a matrix with the vibrational frequencies of the initial state.

From Equation 2.26 the ingredients to calculate ISC rate constants can be deduced. To obtain the vibrational information contained in G(t) and Ω_1 the frequencies of the initial and final states are required. Furthermore, an accurate estimation of the energy difference between these states $\triangle E_{IF}$ and their spin-orbit coupling ($|\langle \Psi_I | \hat{H}_{SO} | \Psi_F \rangle|^2$) have to be computed.

2.6 Computational strategy

The main goal of this thesis is to study spin-crossover in complexes with different transition metals using the computational methods described above. To this purpose, geometries, relative energies, spin-orbit coupling, vibrational frequencies among other properties have to be calculated for all the relevant spin states of the complexes considered. Ideally, one would use CASPT2 using large active spaces to calculate all these properties but the high computational cost of such procedure makes it unavoidable to opt for alternative methods in some cases. Throughout this thesis we have employed the following strategy to obtain an accurate description of the spin crossover process.

The first and most important question concerns the geometry. In many cases, experimental structures are only available for one of the spin states. Therefore, geometries are optimized with DFT using either a GGA or a hybrid functional.

Experience shows that the Ahlrichs basis sets of split-valence + polarization quality [38] are large enough to give accurate geometries in most cases. Furthermore, we use the resolution of the identity approximation to speed up the calculations. This is especially useful for the calculation of the frequencies of the vibrational modes, which is also always done with DFT. The calculation of the vibrational frequencies for excited states requires some extra attention. In the first place, one needs to resort to the TD variant of DFT. In the second place, TD-DFT analytical gradients are not available for all the functionals in the program packages we have used. In these cases, the gradients are obtained from numerical differentiation. When available, the calculated data bond distances and angles, dihedrals, and frequencies are compared to experimental data.

Once the geometries of all spin states are calculated, we turn our attention to the accurate determination of the relative energies. For this purpose, we first construct a CASSCF wave function with the by now standard active space for transition metal complexes. When all metal ligand bonds are simple coordination bonds, the active space has to contain the five TM-3d orbitals, five more TM-d orbitals to account for the double shell effect (TM-3d' or 4d orbitals) and one or two ligand orbitals to account for the sigma interaction between the TM and the N-atoms in the first coordination sphere [39]. When metal-to-ligand or ligand-to-metal charge transfer states are studied, this basic active space is extended with the appropriate ligand orbitals. In case of covalent TM-ligand bonds, the active space should contain the molecular orbitals corresponding to the bonding and antibonding combinations of the orbitals centred on the covalently bonded atoms. Furthermore, one has to add the remaining, basically non-bonding TM-3d orbitals, the second d-shell and the N_σ orbitals, provided this does not lead to too large an active space. In this step, we typically use the ANO-RCC basis sets of Roos and co-workers [40–42]. These generally contracted basis sets are specially designed to recover the maximal amount of correlation energy and give an accurate account of the scalar relativistic effects through the Douglas-Kroll-Hess Hamiltonian. In the CASPT2 step, we typically exclude the deep core electrons (TM-$1s^2..2p^6$; C,N,O-$1s^2$) from the correlation treatment and apply a level shift of 0.10 au to eliminate the effect of intruder states. In all the calculations, we have used the standard CASPT2

zeroth-order Hamiltonian with an IPEA-shift of 0.25 au.

As said before, a full geometry optimization with CASPT2 is unaffordable in any but the smallest model TM complexes. However, it has been observed that certain key parameters of spin crossover are rather strongly influenced by the TM-L distance. The most prominent changes are observed for the vertical excitation energies of the metal-centred (ligand-field or d-d) excitations, but the HS-LS adiabatic energy difference is also sensitive to small changes in the geometry of the first coordination sphere. For this reason, we re-optimize the distance between the TM and the N-atoms in the first coordination sphere by performing a series of single point calculations with different TM-N distances [39]. These geometries are obtained from restricted geometry optimization with DFT. In some cases, we have also re-optimized the TM-N-R angle with CASPT2.

After the calculation of the energies of the different spin states, a step is made to analyze the multiconfigurational wave functions. For this purpose, we use the orthogonal Valence Bond procedure [43–46]. First the canonical (delocalized) active orbitals undergo a unitary transformation to localize them either on the TM or the ligand. The multiconfigurational wave function expansion is re-expressed in Slater determinants constructed with localized orbitals. Since the orbital transformation is unitary this procedure does not affect the energy of the system, and the CAS matrix is simply diagonalized to obtain the coeficients of the expansion in this basis. Due to the localized nature of the orbitals, the Slater determinants can be univocally labelled as $TM^{n+i}L^{m-i}$ electronic configurations and by summing up the weights of all the Slater determinants that belong to one electronic configuration one can easily determine the relative importance of each configuration in the total wave function, count the number of electrons on the TM, and the number of electrons transferred from the TM to the ligand (or *vice-versa*) with respect to a purely ionic description.

The final step of the computational strategy concerns the calculation of the intersystem crossing rates when studying the deactivation of excited states in light induced spin crossover. As explained in the previous section, this is done through the time-dependent formulation of Fermi's golden rule and requires

apart from the vibrational frequencies, normal modes and relative energies, also the spin-orbit coupling between initial and final states. The matrix elements are calculated by adding the spin-orbit operator to the Hamiltonian and writing down the matrix representation of the resulting operator in the basis of the explicit M_S components of the CASSCF wave function of the different spin states. The required spin-orbital integrals are obtained within the atomic mean-field approximation, which implies discarding all two-centre two-electron spin orbit couplings and assuming a fixed average atomic electronic configuration [47]. Furthermore, it is assumed that the spin-orbit coupling is only weakly dependent on the geometry of the complex. This has been extensively tested in earlier studies on similar complexes [48].

2.7 References

[1] A. Szabo and N. Ostlund, Modern Quantum Chemistry (Dover publications Inc., 1947).

[2] J. Miralles, J. Daudey, and R. Caballol, Chem. Phys. Lett. **198**, 555 (1992).

[3] J. Miralles, O. Castell, R. Caballol, and J. Malrieu, Chem. Phys. **172**, 33 (1993).

[4] R. Bartlett, I. Shavitt, and G. Purvis, J. Chem. Phys. **71**, 281 (1979).

[5] R. Bartlett, Ann. Rev. Phys. Chem. **32**, 359 (1981).

[6] R. Bartlett, Recent Advances in Coupled-Cluster Methods (World Scientific Publ., 1997).

[7] I. Shavitt and R. Bartlett, Many-Body Methods in Chemistry and Physics. (Cambridge University Press, 2000).

[8] B. Roos, Adv. Chem. Phys. **69**, 399 (1987).

[9] R. Shepard, Adv. Chem. Phys. **69**, 63 (1987).

[10] B. Roos, P. Taylor, and P. Siegbahn, Chem. Phys. **48**, 157 (1980).

[11] T. Helgaker, P. Jargensen, and J. Olsen, Molecular Electronic Structure Theory (Jhon Wiley and Sons, 2000).

[12] L. Gagliardi and B. Roos, Chem. Soc. Rev. **36**, 893 (2007).

[13] K. Pierloot, Int. J. Quantum Chem. **111**, 3291 (2011).

[14] V. Veryazov, P. Malmqvist, and B. Roos, Int. J. Quantum Chem. **111**, 3329 (2011).

[15] B. Huron, J. Malrieu, and P. Rancurel, J. Chem. Phys. **58**, 5745 (1973).

[16] K. Andersson, P. Malmqvist, B. Roos, A. Sadlej, and K. Wolinski, J. Phys. Chem. **94**, 5483 (1990).

[17] C. Møller and M. Plesset, Phys. Rev. **46**, 618 (1934).

[18] K. Andersson, B. Roos, P. Malmqvist, and P. Widmark, Chem. Phys. Lett. **230**, 391 (1994).

[19] J. Finley, P. Malmqvist, B. Roos, and L. Serrano-Andres, Chem. Phys. Lett. **288**, 299 (1998).

References

[20] C. Angeli, R. Cimiraglia, S. Evangelisti, T. Leininger, and J.-P. Malrieu, J. Chem. Phys. **114**, 10252 (2001).

[21] P. Dirac, Proc. Cambridge Phil. Soc. **26**, 376 (1930).

[22] F. Bloch, Z. Physik **57**, 545 (1929).

[23] P. Hohenberg and W. Kohn, Phys. Rev. B **136**, B864 (1964).

[24] W. Kohn and L. Sham, Phys. Rev. **140**, 1133 (1965).

[25] F. Della Sala and A. Gorling, J. Chem. Phys. **115**, 5718 (2001).

[26] S. Kummel and J. Perdew, Phys. Rev. B **68**, 035103 (2003).

[27] J. Antony and S. Grimme, Phys. Chem. Chem. Phys. **8**, 5287 (2006).

[28] P. Stephens, F. Devlin, C. Chabalowski, and M. Frisch, J. Phys. Chem. **98**, 11623 (1994).

[29] A. Becke, J. Chem. Phys. **98**, 5648 (1993).

[30] E. Runge and E. Gross, Phys. Rev. Lett. **52**, 997 (1984).

[31] G. Onida, L. Reining, and A. Rubio, Rev. Mod. Phys. **74**, 601 (2002).

[32] M. Casida, J. Mol. Struct. **914**, 3 (2009).

[33] M. Casida and M. Huix-Rotllant, Annu. Rev. Phys. Chem. **63**, 287 (2012).

[34] N. Ferré, M. Filatov, and M. Huix-Rotllant, Density-Functional Methods for Excited States (Springer International Publishing, 2016).

[35] M. Etinski, J. Tatchen, and C. Marian, J. Chem. Phys. **134**, 154105 (2011).

[36] C. Marian, WIREs. Comput. Mol. Sci. **2**, 187 (2012).

[37] C. Sousa, C. de Graaf, A. Rudavskyi, R. Broer, J. Tatchen, M. Etinski, and C. Marian, Chem. Eur. J. **19**, 17541 (2013).

[38] A. Schafer, H. Horn, and R. Ahlrichs, J. Chem. Phys. **97**, 2571 (1992).

[39] K. Pierloot and S. Vancoillie, J. Chem. Phys. **125**, 124303 (2006).

[40] P.-O. Widmark, M. P.-Å., and B. O. Roos, Theor. Chim. Acta **77**, 291 (1990).

[41] B. O. Roos, R. Lindh, P.-Å. Malmqvist, V. Veryazov, and P.-O. Widmark, J. Phys. Chem. A **108**, 2851 (2004).

[42] B. O. Roos, R. Lindh, P.-A. Malmqvist, V. Veryazov, and P.-O. Widmark, J. Phys. Chem. A **109**, 6575 (2005).

[43] M. Radon, E. Broclawik, and K. Pierloot, J. Phys. Chem. B **114**, 1518 (2010).

[44] J. Zapata-Rivera, R. Caballol, and C. Calzado, Phys. Chem. Chem. Phys. **13**, 20241 (2011).

[45] J. Zapata-Rivera, R. Caballol, and C. Calzado, J. Comput. Chem. **32**, 1144 (2011).

[46] J. Zapata-Rivera, R. Caballol, and C. Calzado, J. Comput. Chem. **33**, 1407 (2012).

[47] B. Hess, C. Marian, U. Wahlgren, and O. Gropen, Chem. Phys. Lett. **251**, 365 (1996).

[48] A. Rudavskyi, Spin crossover mechanisms unravelled by theory ((Doctoral thesis, University of Groningen, The Netherlands), 2014).

Chapter 3

Photochemistry of Ru polypyridyl complexes

3.1 Introduction

Ru^{II} polypyridyl complexes have attracted interest due to their applications in the conversion of light in chemical energy. These complexes are easily reduced in the excited state and the released electron can be captured by acceptor molecules and used in secondary reactions. The excited state is accessible upon light irradiation including solar energy, coining the basis of the solar energy cells [1–8]. As a consequence, these Ru complexes have been extensively studied using as prototype their simplest tris(2,2'-bipyridine) derivative $[Ru(bpy)_3]^{2+}$ (see Fig. 3.1). The ground state of Ru^{II} in this octahedral ligand-field is characterized by a closed shell singlet (S_0) with the 6 electrons paired in the 4d t_{2g} orbitals. Three different kinds of excited states are possible depending on the orbitals involved. The metal centred (MC) d-d states are generated by excitation of the t_{2g} electrons to the 4d e_g orbitals. Ligand centred (LC) π-π^* excitations can also occur in the aromatic bipyridine ligand. Finally, the metal-to-ligand charge transfer (MLCT) states arise from the promotion of one 4d electron to a π^* orbital on the pyridyl ligands.

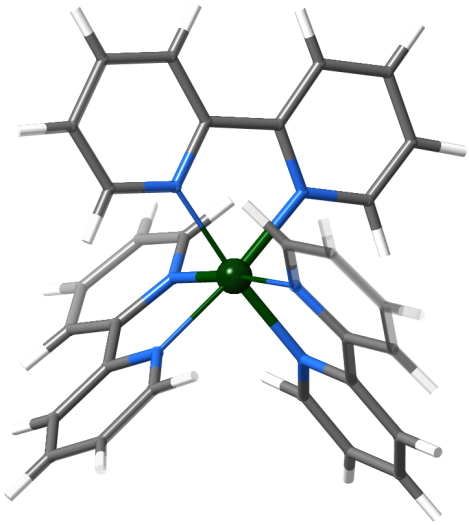

Figure 3.1. Schematic representation of $[Ru(bpy)_3]^{2+}$, studied in this chapter.

During the 1970s and 1980s, the photochemistry of $[Ru(bpy)_3]^{2+}$ was extensively studied [9]. The absorption spectrum of the complex presents two intense bands around 4.3 eV (285 nm) and 2.7 eV (455 nm), respectively [10]. The 455 nm absorption band corresponds to a spin allowed transition to the ^{1}MLCT excited state which rapidly converts by intersystem crossing (ISC) to the ^{3}MLCT triplet, the lowest excited state (see Fig. 3.2) [11, 12]. The ISC efficiency is expected to be close to 1. The easy electron transfer to acceptor molecules from the efficiently populated ^{3}MLCT state makes these complexes very suitable for charge transfer processes [13]. This state decays to the ground state emitting light of 2.0 eV (610 nm), and hence, the complex is luminescent [14].

Although several DFT and TD-DFT studies have been published on $[Ru(bpy)_3]^{2+}$ photochemistry in the last two decades [15–21], some important aspects need to be reviewed. The nature of the MLCT lowest excited state is still unclear. Whether the unpaired electron in this state is localized on a single bipyridine or delocalized over the three ligands may determine the electron transfer rate if the acceptor molecule interacts with one of the ligands [22]. On one hand, experimental evidences point to an initial photoinduced delocalized MLCT state followed by localization to a single ligand [23]. This process is known as inter-ligand electron transfer (ILET) and from a mixed time-

dependent quantum-classical dynamics computational method is predicted to take place in the range of hundreds of fs depending on the solvent [24]. On the other hand, several TD-DFT results stress that the electron is delocalized over the three bipyridine ligands and therefore no ILET is expected [25–27]. Finally, a quantum mechanics/molecular mechanics study indicates delocalized MLCT states in gas phase and localization on two ligands when the effects of the solvent are included [28].

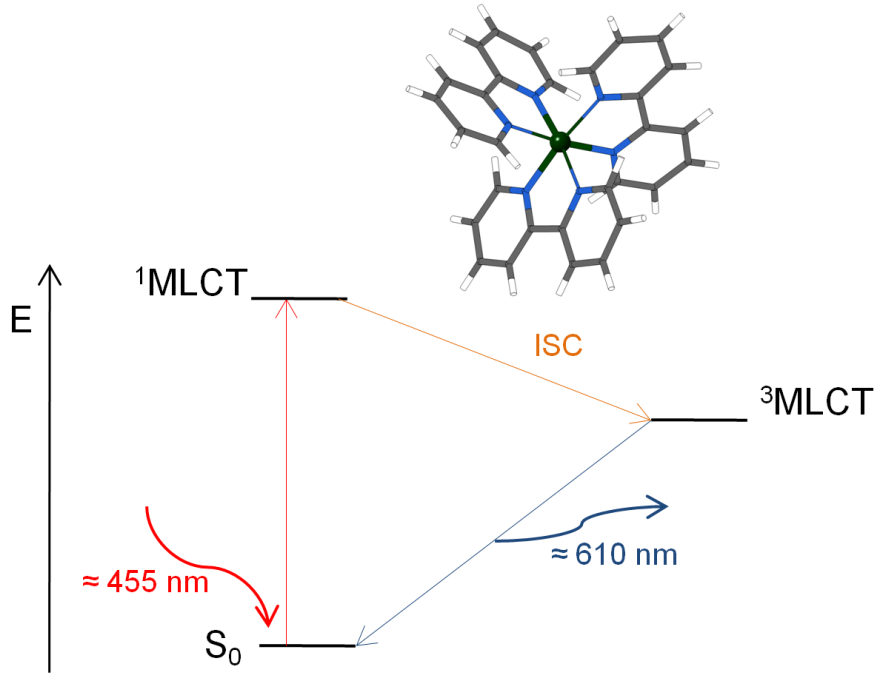

Figure 3.2. Schematic representation of the absorption and emission processes in $[Ru(bpy)_3]^{2+}$.

Moreover, the processes after the excitation and before the ISC to the ^{3}MLCT are also unclear because they occur on an ultrafast timescale [29]. The Franck-Condon ^{1}MLCT, for instance, has never been directly observed since this state is very short-lived and rapidly evolves to the triplet state. This behaviour is attributed to the large spin-orbit coupling (SOC) between the two excited states with different total spin moment. The ISC is experimentally supposed to occur in 100-300 fs [30, 31], 40 ± 15 fs [32] or 15 ± 10 fs [33] depending on the spectroscopic technique and hence is also a controversial issue.

The lowest d-d excited state ^{3}MC is proposed to be 0.45 eV above the emitting ^{3}MLCT from the study of temperature dependence of the photochemical properties of the complex [34]. This ^{3}MC is a short-lived state that can be thermally accessible *via* the ^{3}MLCT depending on the energy spacing of these states and its equilibrium geometry is expected to be strongly distorted with respect to both the ^{3}MLCT and the ground state [35]. DFT calculations also indicate that the ^{3}MC state energy is stabilized by substitutions at the 6 and 6' positions of bipyridine [36] and eventually become lower in energy than the ^{3}MLCT state.

This chapter presents a discussion on these points based on *ab initio* computational calculations. The geometry of the most relevant states in the photochemistry of $[Ru(bpy)_3]^{2+}$ is optimized at the DFT level, their vertical absorption and emission spectra are estimated with TD-DFT and multireferential calculations. Furthermore, the character of the excited states, the effect of the solvent and the processes involved in the excited states relaxation are analyzed.

3.2 The vertical absorption

3.2.1 Optimization of the S_0 state

The S_0 geometry has been optimized with DFT using the BP86 [37, 38], B3LYP [39, 40], and PBE0 [41–43] functionals as implemented in the Turbomole package [44], and with CAM-B3LYP [45] using the Gaussian package [46]. The def2-SVP [47] basis set for all the atoms has been used in the calculations. A comparison of the resulting Ru-N distance and the four N-Ru-N different angles with the experimental X-ray data [48] is shown in Table 3.1. While the optimized angles with all the functionals are in good agreement with experimental data, only BP86 and PBE0 give accurate distances since both B3LYP and CAM-B3LYP tend to overestimate them.

For all the optimized geometries listed, the first 30 singlet excited states have been computed with TD-DFT. In all cases, the states with highest oscillator

strength have been compared with the experimental absorption spectrum of the complex [10, 11]. Surprisingly, B3LYP is in better agreement with the experimental data than CAM-B3LYP, which has been reported to perform well for charge transfer excitations [45]. BP86 excited state energies are lower than the expected ones. Since the best DFT geometrical and TD-DFT energetic description is obtained using PBE0, this functional will be used in the remainder of this chapter.

Table 3.1. DFT S_0 optimized Ru-N distances (in Å) and angles (in degrees) and TD-DFT absorption bands (eV). X-ray parameters [48] and experimental absorption bands [10, 11] are reported for comparison.

	Ru-N distance	N-Ru-N angles				Absorption bands	
exp.	2.056	78.7	89.2	96.2	173.0	$\simeq 2.7$	$\simeq 4.3$
BP86	2.071	78.8	88.4	96.6	173.6	2.2	3.3
B3LYP	2.097	78.2	88.4	96.9	173.2	2.8	4.0
CAM-B3LYP	2.091	78.3	88.2	96.9	173.4	3.3	4.7
PBE0	2.067	78.7	88.1	96.8	173.7	3.1	4.2

The PBE0 geometry optimization and TD-DFT absorption spectrum estimation have been repeated using def2-TZVP [49] in the Ru metal centre and def2-SVP in the rest of the atoms in order to check the effect of the basis set. No significant differences with respect to the previous results have been detected and therefore the def2-SVP basis set in all the atoms has been used along all the study.

3.2.2 TD-DFT Absorption Spectrum

The first 30 singlet excited states have been computed on the ground state PBE0 optimized geometry at TD-DFT level of calculation. All the states with considerable oscillator strength are of MLCT character. The excited electron is promoted from a d-orbital of the metal centre to ligand orbitals delocalized over the three bipyridine ligands (see Fig. 3.3).

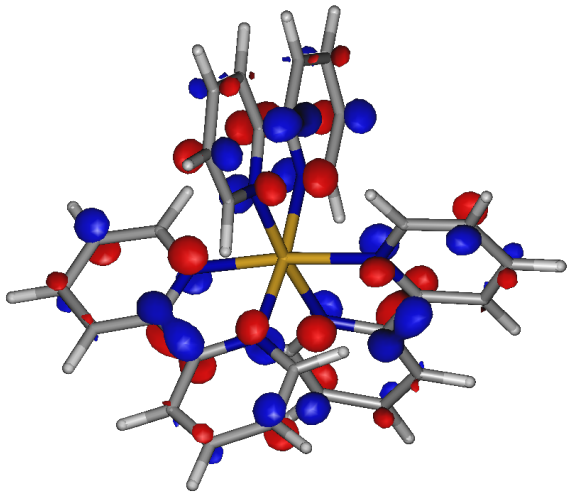

Figure 3.3. Anti-bonding orbital delocalized over the three bipyridine ligands.

The absorption spectrum of the complex has been simulated by adding gaussian functions with height proportional to the oscillator strength in each transition (see Fig. 3.4).

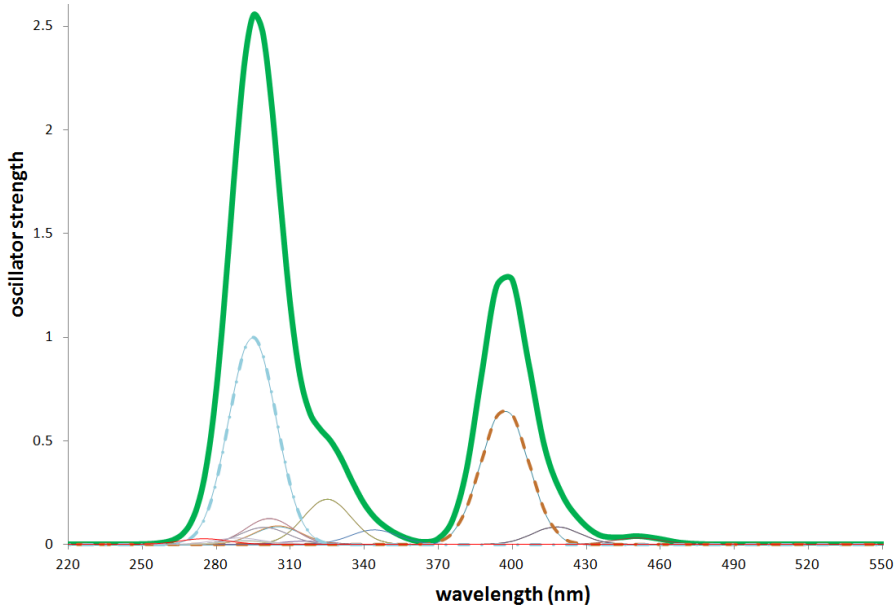

Figure 3.4. TD-DFT first 30 singlet excited states of the PBE0 ground state optimized geometry (thin lines) and sum of the individual contribution to simulate the $[Ru(bpy)_3]^{2+}$ absorption spectrum (green line).

The first band in the computed spectrum (green line in Fig. 3.4) has a maximum at 280 nm and a weak shoulder at 340 nm. This band results from the overlap of several transitions, the most intense two at 294 nm and at 325 nm respectively (thin lines in Fig. 3.4). Both states are of MLCT character with the excited electron delocalized on the three bipyridine ligands. In contrast with the first band of the spectrum, the second one between 370 nm and 460 nm arises from the overlap of various transitions, two at 397 nm and another at 418 nm. Finally, the weak transition at 451 nm also gives a small contribution. As a result, this band is wider with respect to the first one but less intense.

In Fig. 3.5 the calculated absorption spectrum (green line) is compared with experimental data (black line) [22].

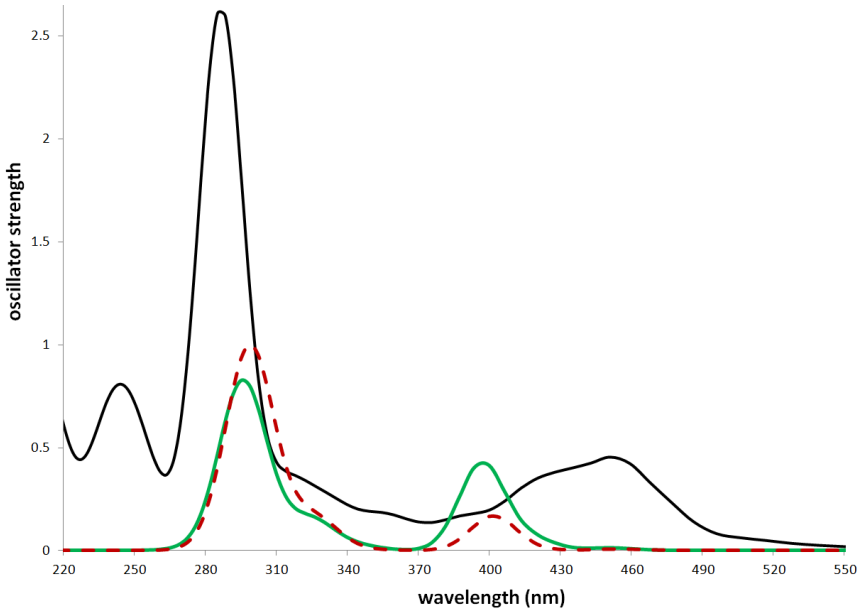

Figure 3.5. Comparison of the TD-DFT $[Ru(bpy)_3]^{2+}$ spectrum in gas phase (green line), in acetonitrile accounted with the COSMO model (red dashed line) and the experimental one in acetonitrile (black line) [22].

The bands appearing at the very-left side of the experimental spectrum are considerably high in energy and are not detected with our TD-DFT calculations which consider only the first 30 excited states. The calculated brightest band (between 280 nm and 340 nm) is predicted to appear practically in the

same energy region as the experimental one (around 260 nm and 310 nm). In contrast, the Q band, which is experimentally expected between 400 nm and 496 nm is 30 nm blue-shifted in our calculations (between 370 nm and 460 nm). Although the TD-DFT predicted oscillator strengths are smaller, in a qualitative manner the shape of the predicted spectrum is similar to the experimental one. In general terms one can consider that our results are in good agreement with the experiment. The lower intensity of the band between 280 nm and 340 nm is most probably caused by limiting the number of excited states to 30 in the TD-DFT calculation. More roots would lead to more intensity at higher energy.

Since the TD-DFT are performed in gas phase and the experimental measurements are carried out in acetontrile, the solvent effects on the computed spectrum need to be reviewed. In this sense, using the COSMO model in Turbomole [50, 51], the ground state geometry has been optimized with DFT and the TD-DFT spectrum on the obtained structure has been recalculated adding the effect of the solvent. To be consistent with the experiment, acetonitrile ($\epsilon = 35.69$) has been considered. As shown in Fig. 3.5, the absorption bands taking into account the effect of the solvent (red dashed line) appear at practically the same wave length as in gas phase (green line). This non influence of the solvent on the TD-DFT spectrum is attributed to the fact that in the ^{1}MLCT states the excited electron is delocalized over the three ligands, and hence, the dipole moment is small. In ^{1}MLCT states localized in a single ligand one could expect higher dipole moments which would be more stabilized by the solvent effects, with the consequent change in the excitation wavelengths. In contrast with the excitation wavelengths, the oscillator strengths with the COSMO calculations slightly differ from the gas phase, making the shape of the absorption spectrum even closer to the experimental one.

3.2.3 CASPT2/DFT Ru-N distances reoptimization

In order to validate the ground state PBE0 optimized geometry, the Ru-N distances in the singlet ground state have been re-optimized in terms of CASPT2/

DFT calculations following the procedure outlined in Sec. 2.6. In each calculation, the Ru-N distances have been frozen and the rest of the geometrical parameters have been relaxed with PBE0. The energy of the obtained structures has been estimated by CASPT2 single point calculations. The [10,7]-CASSCF reference wave function used in this calculations consists of 10 electrons in the 4d-orbitals of Ru and two σ orbitals resulting from bonding mixing of the 4d metal orbitals and 2p orbitals of the bypiridine ligands. As pointed out in Chapter 2, it is common practice to add a second d-shell to the active space in the calculations for TM-3d ions with five or more d-electrons. This extension of the active space is necessary to account for the large radial electron correlation in the crowded 3d shell; many electrons share a relatively small volume [52]. However, it is also well-known that the importance of the second d-shell drastically diminishes for 4d and 5d TM ions. In fact, we have converged the wave function including a 4d' shell in the active space, but the results obtained showed no difference with those obtained with the [10,7]-CASSCF calculations. In the present chapter all the multireferential calculations are performed with the Molcas package [53, 54]. The basis set used is of natural orbitals type [55–57] contracted to [8s7p5d] for Ru, [5s4p] for N, [2s1p] for C and [2s] for H.

The above-mentioned distance has been scanned between 2.05 Å and 2.08 Å. The minimal energy of this re-optimization has been found at 2.07 Å, confirming the prediction of the previous PBE0 optimization. This is somewhat unexpected given the fact that a shortening of $\sim$ 0.1 Å in the metal-ligand distance occurs for the $[Fe(bpy)_3]^{2+}$ complex [58, 59]. A systematic study including more cases should be performed to check how general this observation is.

3.2.4 CASSCF vertical absorption energies

The vertical excited singlet energies have been estimated on the ground state PBE0 optimized geometry with CASSCF calculations. To obtain the MLCT excited states, the [10,7]-CASSCF wave function used in Sec. 3.2.3 needs to be expanded with three bipyridine empty orbitals resulting in a [10,10]-CAS. Two of these three ligand anti-bonding orbitals included into the active space

are placed on two bipyridines and the third one is delocalized over the three ligands (see Fig. 3.6).

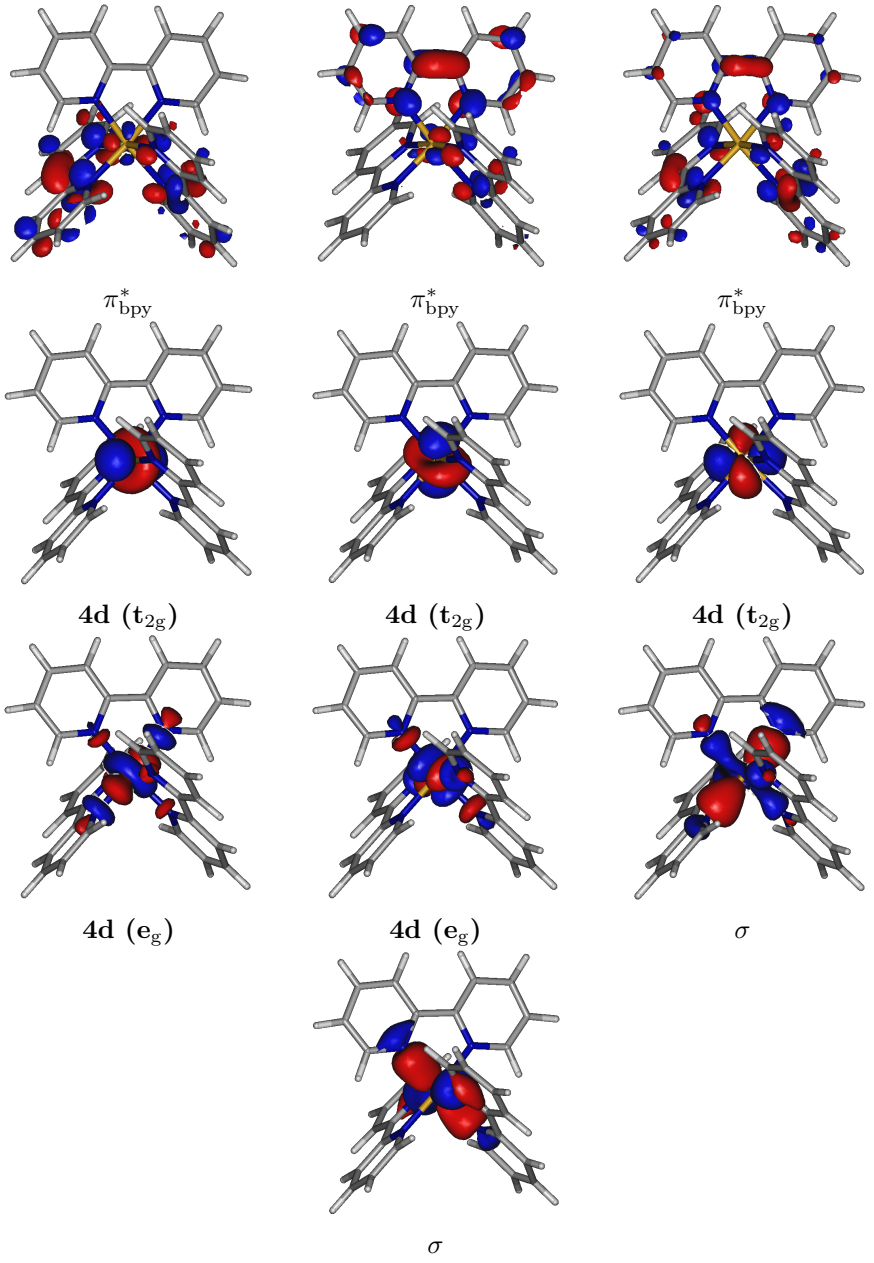

Figure 3.6. Metal-ligand orbitals included in the [10,10]-CASSCF estimation of the vertical singlet excited state energies.

The basis set used in these calculations is of atomic natural orbitals type [55–57], and contracted to [8s7p5d3f2g] for Ru, to [4s3p2d1f] for C and N and to [3s1p] for H. The effect of the solvent has been evaluated in the CASSCF energy estimations with the PCM model using the dielectric constant of acetonitrile ($\epsilon = 35.69$).

In a similar way as in the TD-DFT reproduction of the vertical absorption spectrum, the solvent effects with CASSCF are negligible since the ^{1}MLCT states in acetonitrile are in all cases only 0.03 eV lower with respect to the gas phase calculation (see Table 3.2). The dipole moment of the ground and excited states are small, explaining why the solvent does not affect the absorption spectrum of the system and confirming the observations in section 3.2.2. CASSCF calculations predict two degenerate ^{1}MLCT states at 3.12 eV (397 nm) with high oscillator strength corresponding to the Q band of the experimental absorption spectrum expected between 400 nm and 496 nm. In contrast, the two states with highest oscillator strength at 3.29 eV (377 nm) are red-shifted with respect to the experimental Soret band between 280 nm and 340 nm. Interestingly, CASSCF calculations behave in an opposite way as TD-DFT, which agreed with the experimental data in the Soret band estimation and failed with the Q band. The states involved in the Q band present higher multiconfigurational character and hence are better estimated with CASSCF. Probably, an expansion of the active space with bonding and antibonding orbitals of the ligands is required to improve the description of the states involved in the Soret band.

The first three near-degenerate ^{1}MLCT states in Table 3.2 are characterized by the mono-occupation of these three ligand orbitals and one can consider that the excited electron in the lowest singlet excited state is delocalized over the three bipyridine ligands. The rest of MLCT states are also linear combinations of Slater determinants with singly occupied ligand π^* orbitals, and hence are labelled as delocalized.

Table 3.2. [10,10]-CASSCF vertical absorption energies (in eV) and oscillator strengths for the ground state PBE0 optimized geometry in gas phase and in acetonitrile, accounted by PCM. Dipole moments (in debye) for the gas phase calculation.

	gas phase			**acetonitrile**	
	energy	**osc. strength**	μ	**energy**	**osc. strength**
S_0	0.00		0.28	0.00	
^{1}MLCT	2.87	$3.9{\cdot}10^{-3}$	0.11	2.84	$3.9{\cdot}10^{-3}$
^{1}MLCT	2.95	$5.3{\cdot}10^{-4}$	5.69	2.92	$4.5{\cdot}10^{-4}$
^{1}MLCT	2.95	$5.2{\cdot}10^{-4}$	6.33	2.92	$4.4{\cdot}10^{-4}$
^{1}MLCT	3.12	$1.4{\cdot}10^{-1}$	2.04	3.09	$1.4{\cdot}10^{-1}$
^{1}MLCT	3.12	$1.5{\cdot}10^{-1}$	2.32	3.09	$1.6{\cdot}10^{-1}$
^{1}MLCT	3.25	$9.2{\cdot}10^{-4}$	0.30	3.22	$4.6{\cdot}10^{-3}$
^{1}MLCT	3.29	$3.4{\cdot}10^{-1}$	1.32	3.26	$3.4{\cdot}10^{-1}$
^{1}MLCT	3.29	$3.4{\cdot}10^{-1}$	2.01	3.26	$3.5{\cdot}10^{-1}$

3.2.5 The metal centred states

Excitations from the ground state to metal centred excited states are forbidden by symmetry and therefore they are optically silent and not detected in the absorption spectrum. However, if these states are energetically close to the MLCT they can play an important role on the relaxation mechanisms of the complex, influencing its photochemistry. Furthermore, if the ^{3}MC state is available through any relaxation path, the compound may be a good candidate to experiment SCO.

The six Ru^{II} d-electrons in an octahedral ligand-field are paired in the 4d t_{2g} orbitals in a closed shell singlet ground state. These orbitals are lower in energy than the e_g ones, which are anti-bonding with respect to the Ru-N coordination bond (see Fig. 3.7). The three lowest-lying ^{3}MC states ($^3T_{1g}$ in O_h symmetry) arise from the promotion of an electron from the occupied t_{2g} to the e_g empty orbitals.

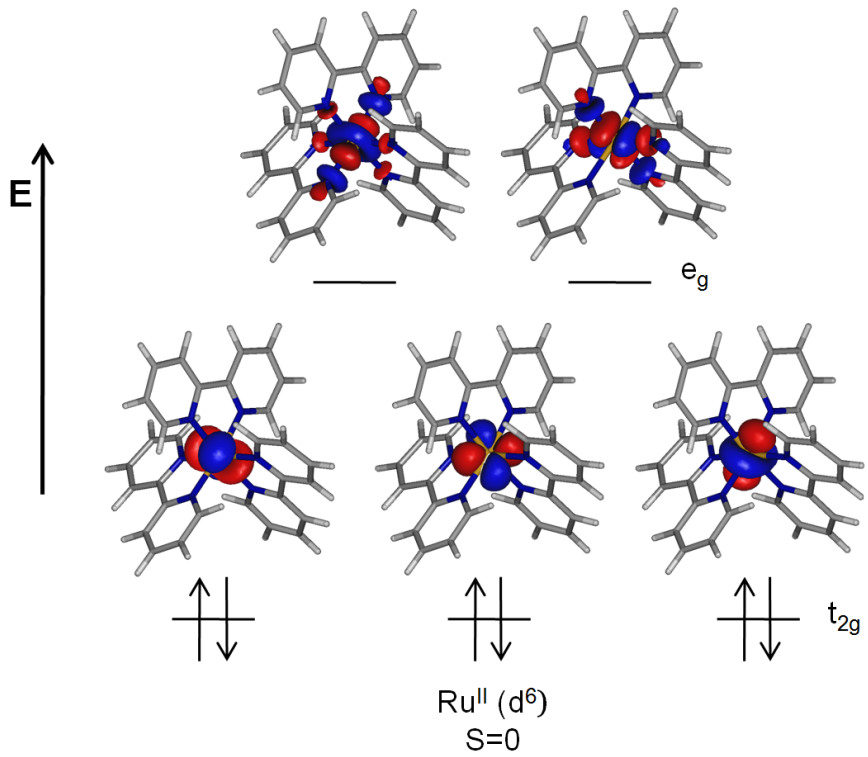

Figure 3.7. 4d orbitals and electronic configuration of the singlet ground state of Ru^{II} in an octahedral ligand-field.

Table 3.3 lists the lowest triplet states estimated with TD-DFT and CASSCF. Both methods place the lowest ^{3}MC states at higher energy than the lowest ^{3}MLCT states, almost 1 eV for TD-DFT and 0.5 eV for CASSCF. Due to the large basis set applied, the CASPT2 calculation is rather costly and we have only determined the correction to the relative energy of the lowest ^{3}MC state. CASPT2 lowers the excitation by 0.1 eV, similarly to what was found for the same excitation in $[Fe(bpy)_3]^{2+}$ [59]. The discrepancy between CASSCF and TD-DFT concerning the ^{3}MLCT excitation energy can largely be attributed to the lack of electron correlation in the CASSCF description of the ^{3}MLCT state. Previous studies indicate that the relative energy will be lowered by 0.5-1.0 eV when these effects are accounted for. Some of the low-lying triplet states in the TD-DFT calculation arise from excitations between π and π^* orbitals on the ligand (^{3}LC). Given the fact that the active space does not contain ligand π orbitals, we cannot reproduce these excitations with CASSCF.

Table 3.3. TD-DFT, [10,10]-CASSCF and CASPT2 energy estimation (in eV) of the triplet vertical excited states in the gas phase optimized ground state geometry.

	TD-DFT	**[10,10]-CASSCF**	**CASPT2**
^{3}MLCT	2.57 (2x), 2.63, 2.64, 2.74 (2x), 2.86 (2x), 2.89	2.86, 2.90 (2x), 3.06, 3.09 (2x), 3.17 (2x), 3.25	2.47
^{3}LC	3.40 (2x), 3.41		
^{3}MC	3.48 (2x)	3.29, 3.30	3.21
^{3}MLCT	3.53, 3.62 (2x)		
^{3}MC	3.73	3.60	
^{3}MLCT	3.73, 3.80 (2x)		
^{3}MC	3.85	3.91	

3.3 Geometry relaxation in the excited states

3.3.1 Optimization of the ^{1}MLCT and ^{3}MLCT states

The geometries of the lowest ^{1}MLCT and ^{3}MLCT states have been optimized at TD-DFT and DFT level respectively, using PBE0 (see Tables 3.4 and 3.5). While in the S_0 geometry all six Ru-N distances are identical, 2.067 Å, the RuN_6 core of the complex suffers small distortions in the singlet and triplet MLCT states. The average Ru-N distance is very close to the one calculated for the ground state but in both states we observe two longer and four shorter distances. This has two possible explanations. In the first place, the Ru-4d$(t_{2g})^5$ configuration is Jahn-Teller active and induces in principle a spontaneous distortion of the geometry to lower the energy. In the second place, there is a tendency of the excited electron to localize on one of the bipyridine ligands. This localization is accompanied by a distortion of the geometry that traps the electron. To quantify the importance of the Jahn-Teller distortion we have optimized the geometry of the ionized system $[Ru(bpy)_3]^{3+}$, corresponding to a Ru^{3+} ion with a 4d$(t_{2g})^5$ electronic configuration. The resulting geometry shows a nearly octahedral RuN_6 core with a difference between the long and the short Ru-N distance of less than 0.01 Å, too small to explain the distortion observed in the optimized MLCT geometries of the di-cation. Hence

inter-ligand electron transfer (ILET) appears to be the dominant factor in the geometry distortion. Both singlet and triplet MLCT states have the electron localized on one of the bipyridines and show an important dipole moment of 6.96 D and 6.60 D respectively. The ligand with the extra electron (bpy_1) has the shortest Ru-N distances listed in Table 3.4, while the opposite Ru-N bonds are enlarged as schematically shown in Fig. 3.8.

Table 3.4. Coordination distances (in Å) for the S_0, ^{1}MLCT and ^{3}MLCT PBE0 relaxed states.

	Ru-N distances					
	bpy$_1$		**bpy$_2$**		**bpy$_3$**	
S_0	2.067	2.067	2.067	2.067	2.067	2.067
^{1}MLCT	2.055	2.055	2.081	2.062	2.081	2.062
^{3}MLCT	2.026	2.026	2.099	2.070	2.099	2.070

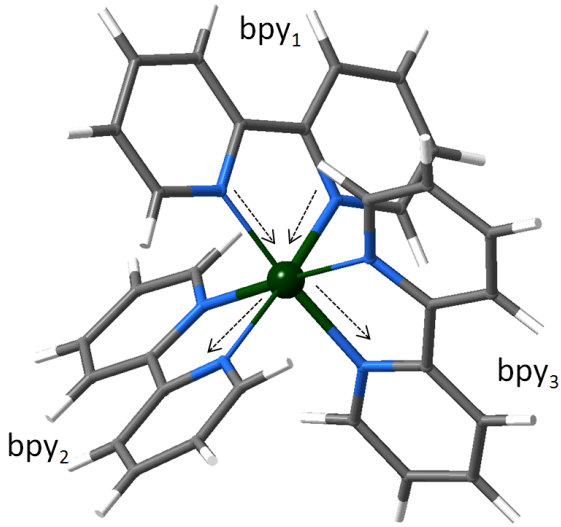

Figure 3.8. Schematic representation of the changes in the Ru-N coordination distances suffered by the relaxed singlet and triplet MLCT states with respect to the S_0 ground state optimized geometry.

Consistently with experimental observations, DFT/TD-DFT results predict the relaxed ^{3}MLCT to be more stable than ^{1}MLCT (see Table 3.5). Both states have the same electronic configuration and the main difference in the

energy is the lack of intersite exchange interaction in the singlet. CASSCF and CASPT2 also predict a slightly more stable ^{3}MLCT state. The geometry relaxation causes a stabilization of the lowest MLCT states by approximately 0.2 eV. The relative energies are similar for all three computational schemes and in good agreement with the photochemical behaviour.

Table 3.5. Relative energies (in eV) for the S_0, ^{1}MLCT and ^{3}MLCT PBE0 relaxed states. [10,10]-CASSCF and CASPT2 single point relative energies (in eV).

	Relative energy		
	PBE0	**[10,10]-CASSCF**	**CASPT2**
S_0	0.00	0.00	0.00
^{1}MLCT	2.52	2.61	2.34
^{3}MLCT	2.24	2.60	2.33

3.3.2 Character of the MLCT relaxed states

The excited electron in the ^{1}MLCT vertical excited states has been predicted to be delocalized over the three ligands at both PBE0 and CASSCF levels. In contrast, the coordination distances in the ^{1}MLCT and ^{3}MLCT optimized geometries indicate that the character of these states changes during the relaxation process. Fig. 3.9 maps the spin density of the ^{3}MLCT relaxed state. An important part of this density is located on the metal centre confirming that the excited electron comes from a 4d Ru orbital. The excited electron is localized on the bipyridine moiety whose Ru-N distances decrease (see Fig. 3.8).

In order to check the solvent effects, the ^{3}MLCT geometry has been re-optimized with the COSMO model [50, 51] and acetonitrile as solvent ($\epsilon = 35.69$). In a similar way as in gas phase, in solution the unpaired electron is localized on a single ligand. The optimized geometry in solution slightly differs from the one in gas phase, resulting in an increase of the dipole moment from 6.60 D in gase phase (see Sec. 3.3.1) to 9.90 D in solution. The COSMO results confirm the experimental observations by McCusker et al. which state that in nitrile

solution the unpaired electron is delocalized in the vertical excitation and localized in the triplet state after ILET process [23]. In accordance with the DFT results, [10,10]-CASSCF single point calculations on the ^{3}MLCT PBE0 optimized geometry confirm confinement of the excited electron in a single ligand in both gas phase and acetonitrile accounted by the PCM model.

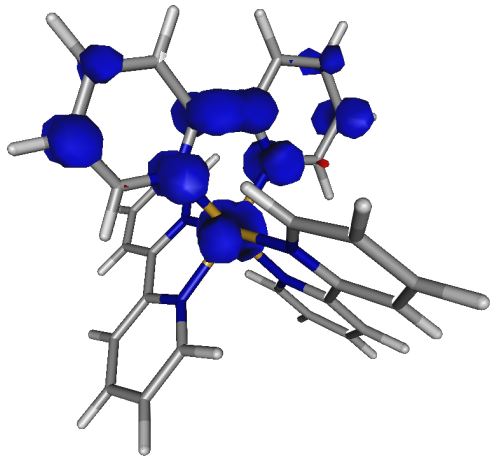

Figure 3.9. Spin density for the ^{3}MLCT optimized geometry.

The probability of ILET between bipyridines can be estimated with *ab initio* calculations by the hopping integral, t. To this purpose, two ^{1}MLCT states Φ_a and Φ_b, with the excited electron localized in different bipyridines, and two ^{1}MLCT states Φ_c and Φ_d, with the electron delocalized over the two and three bipyridines respectively, have been separately optimized with CASSCF calculations using the ground state geometry with three equivalent ligands (see Fig. 3.10). The [6,6]-CAS included the five 4d orbitals of Ru and the anti-bonding orbital of the bipyridine containing the excited electron in each case.

The t term corresponds to the coupling between two states, $t =< \Phi_1|\hat{H}|\Phi_2 >$. In the present case Φ_a, Φ_b, Φ_c and Φ_d are described with CASSCF wave functions using orbitals optimized independently which, in consequence are nonorthogonal. Given two nonorthogonal states Φ_i and Φ_j, the hopping integral is estimated with $t = \frac{1}{2}\sqrt{\triangle E^2 - \frac{(H_{ii}-H_{jj})^2}{1-S_{ij}^2}}$, where H_{ii} and H_{jj} denote Hamiltonian

and S_{ij} overlap matrix elements [60–63] which are determined in a CAS State Interaction calculation [64].

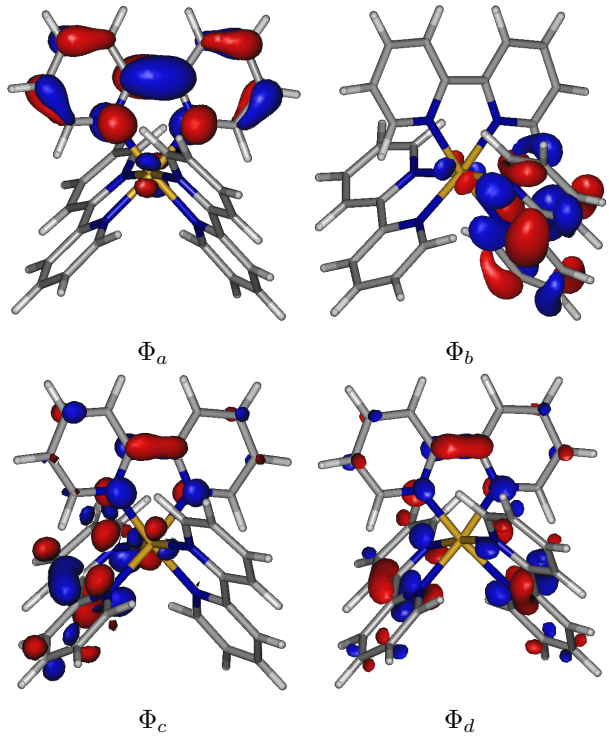

Figure 3.10. Ligand mono-occupied orbitals in the ^{1}MLCT states Φ_a, Φ_b, Φ_c and Φ_d states accounted to estimate ILET probability with [6,6]-CASSCF calculations.

Results of these calculations are summarized in Table 3.6. Starting from the delocalized states described with Φ_c and Φ_d, there is a large probability for localization as shown by the large hopping integrals between these two states and Φ_a, which describes the situation with the excited electron localized on one ligand. In an opposite way, the interaction between Φ_a and Φ_b is considerably smaller, giving a hopping integral of 0.04 eV and denoting small coupling between ^{1}MLCT states with the excited electron localized on two different ligands. In this case, low ILET probabilities indicate that after being localized during the relaxation path the electron is held in a single ligand. This favours electron capture by acceptor molecules.

Table 3.6. Energy difference (in hartree), Hamiltonian matrix (shifted upward by 6004 hartree) and overlap matrix elements from the State Interaction calculation between the different states used to estimated the hopping integral, t (in eV) for the inter-ligand electron transfer between bipyridines.

Φ_I	Φ_F	$\triangle E^2$	H_{ii}	H_{jj}	S_{ij}	t
Φ_a	Φ_b	$7.7{\cdot}10^{-6}$	-0.864503	-0.863864	0.088904	**0.04**
Φ_a	Φ_c	0.30	-0.864503	-0.838482	0.598667	**7.44**
Φ_a	Φ_d	0.04	-0.864503	-0.828890	0.479617	**2.72**
Φ_b	Φ_c	$6.7{\cdot}10^{-4}$	-0.863864	-0.838482	-0.144260	**0.04**
Φ_b	Φ_d	$2.2{\cdot}10^{-3}$	-0.863864	-0.828890	-0.480540	**0.33**

3.3.3 Intersystem crossing and emission

To estimate the ^{1}MLCT $\rightarrow$ ^{3}MLCT ISC rate in $[Ru(bpy)_3]^{2+}$ with the Fermi's golden rule approach discussed in Chapter 2, the ^{3}MLCT DFT and ^{1}MLCT TD-DFT frequencies at the optimized geometries have been used. The spin-orbit coupling (SOC) and the energy difference between the states also required to this purpose have been obtained, respectively, from the [10,10]-CASSCF and CASPT2 single point calculations in Sec. 3.3.1. Table 3.7 reports the vibrational and SOC terms and the estimated rate, k_{ISC}=$1.01{\cdot}10^{14}$ s^{-1}. The large rate obtained indicates an ultrafast ISC favoured by the considerably high SOC estimated between the singlet and triplet MLCT states. Our calculations predict a lifetime of 10 fs for the ^{1}MLCT state, supporting the Chergui et al. experimental observations [33].

Table 3.7. Estimation of the ^{1}MLCT $\rightarrow$ ^{3}MLCT ISC rate. Vibrational term in $cm^2{\cdot}s^{-1}$, spin-orbit coupling in cm^{-1}, k_{ISC} rate constant in s^{-1} and lifetime in fs.

	vibrational term	SOC term	k_{ISC}	lifetime
^{1}MLCT $\rightarrow$ ^{3}MLCT	348774970	539	$1.01{\cdot}10^{14}$	10

The emission spectrum of $[Ru(bpy)_3]^{2+}$ has been predicted with DFT, [10,10]-CASSCF and CASPT2 single point energy calculations and compared with the experimental one which presents a band around 2.03 eV (610 nm) [14].

The emission energy is estimated as the vertical transition from the ^{3}MLCT emitting state at the optimized geometry to S_0 and, as shown in Table 3.8 is in good agreement with the experiment at all levels. Taking into account the spin-orbit coupling between these states with a CAS State Interaction calculation the lifetime of the emitting ^{3}MLCT has been determinetd to be 9 μs, close to the experimental value 5.21 μs [11]. ^{3}MLCT is longer-lived compared to ^{1}MLCT indicating that the one-electron transfer to an acceptor molecule will be held after the intersystem crossing and at the triplet excited state.

Table 3.8. DFT, [10,10]-CASSCF and CASPT2 energies at the relaxed ^{3}MLCT PBE0 optimized geometry, relative to S_0 at the optimized geometry. State Interaction calculation of the ^{3}MLCT lifetime in μs.

	DFT	[10,10]-CASSCF	CASPT2	lifetime
^{3}MLCT	2.24	2.60	2.33	
vertical S_0	0.13	0.46	0.17	
emission	2.11 (588 nm)	2.14 (579 nm)	2.16 (574 nm)	9

3.3.4 Reduction potentials for the ground and ^{3}MLCT states

The electron transfer to acceptor molecules implies the oxidation of the complex, which transfers one electron to the acceptor molecule. This transfer is favoured in the ^{3}MLCT excited state. Equations (3.1) and (3.2) summarize this process where A labels the acceptor molecule and $[Ru(bpy)_3]^{2+}$ and $*[Ru(bpy)_3]^{2+}$ the ground and ^{3}MLCT states respectively.

$$[Ru(bpy)_3]^{2+}(S = 0) + A \longrightarrow [Ru(bpy)_3]^{3+}(S = 1/2) + A^- \tag{3.1}$$

$$*[Ru(bpy)_3]^{2+}(S = 1) + A \longrightarrow [Ru(bpy)_3]^{3+}(S = 1/2) + A^- \tag{3.2}$$

Although in the present case an oxidation reaction is being studied, the electrodic potentials in electrochemistry are typically referred to reduction, which is the inverse process

$$[Ru(bpy)_3]^{3+} + 1e^- \longrightarrow [Ru(bpy)_3]^{2+}. \tag{3.3}$$

The reduction potentials (E in V) are proportional to the Gibss free energy variation (ΔG)

$$\Delta G = -nFE, \tag{3.4}$$

where F is the Faraday constant and n the number of electrons implied in the reduction reaction. A favoured reduction ($\Delta G << 0$) gives a high E. Usually, the redox potentials are referred to the Normal Hydrogen Electrode (NHE). From thermodynamical experiments and theoretical considerations, the absolute reduction potential of NHE has been estimated to be 4.43 V [65]. As available experimental data in this complex are referred to Saturated Calomel Electrode (SCE) whose reduction potential is 0.2412 V with respect to NHE [66], our results will be presented vs SCE for comparison.

The redox potentials for $[Ru(bpy)_3]^{2+}$ and $[Ru(bpy)_3]^{2+*}$ in acetonitrile and 298 K have been computed at the PBE0 level. The free energy contributions have been estimated from the analytic frequencies of the ground state $[Ru(bpy)_3]^{2+}$, ^{3}MLCT $*[Ru(bpy)_3]^{2+}$ and the three-charged doublet state $[Ru(bpy)_3]^{3+}$ optimized geometries. Table 3.9 summarizes the results of these calculations. Reduction potentials for both ground and excited species are in good agreement with experimental data [67]. As expected, the oxidation process and the capture of an electron by an acceptor are clearly favoured in the ^{3}MLCT state with a negative reduction potential in contrast with the ground state.

Table 3.9. PBE0 computed Gibss free energy variation (in eV) and reduction potentials (in V) for the ground and ^{3}MLCT states of $[Ru(bpy)_3]^{2+}$ vs SCE in acetonitrile at 298 K. Experimental reduction potentials [67] are given for comparison.

	ΔG	E	E (exp.)
$[Ru(bpy)_3]^{3+} + 1e^- \longrightarrow [Ru(bpy)_3]^{2+}$	-1.07	1.07	1.29
$[Ru(bpy)_3]^{3+} + 1e^- \longrightarrow *[Ru(bpy)_3]^{2+}$	0.84	-0.84	-0.81

3.4 Conclusions

The present chapter provides DFT, CASSCF and CASPT2 insights on the photochemistry and ability of $[Ru(bpy)_3]^{2+}$ to transfer electrons to capturing molecules. First of all, the ground state geometry has been optimized at PBE0 level and its vertical absorption spectrum has been computed with TD-DFT and [10,10]-CASSCF and determined to be in good agreement with the experiment. Due to its multiconfigurational character the Q band is better described with CASSCF and slightly blue-shifted with TD-DFT. In an opposite way, the Soret band match better with the experimental spectrum and is red-shifted with CASSCF which would require and expansion of the CAS with bipyridine anti-bonding orbitals in order to improve its description. At both levels of calculation, the ^{1}MLCT states are characterized by the excited electron delocalized over the three bipyridine ligands. This observation is supported by CASSCF small dipole moments which are responsible for no changes when the solvent is taken into account with COSMO for TD-DFT and with PCM for CASSCF.

In the second part of the chapter all the processes involved in the relaxation from the vertical ^{1}MLCT to the recovery of the ground state are analyzed. While in the ground state all the coordination distances are similar, in the PBE0 ^{1}MLCT and ^{3}MLCT optimized geometries some distances are shortened indicating changes in the electronic structure of these states in their relaxed geometries. The unpaired electron in the MLCT optimized geometries is localized on a single bipyridine in gas phase and in acetonitrile. Taking into account that the vertical ^{1}MLCT is delocalized, during the relaxation and ISC to the ^{3}MLCT state the excited electron is localized by ILET, process which has been estimated to be highly probable by state interaction calculations. The small hopping integral for ILET between two states localized in one bipyridine shows that once localized the electron will be confined in a single ligand. The ISC rate has been predicted to be 11 fs with the Fermi's golden rule approach. The calculated emission spectrum of the complex is in good agreement with the experiment. Our PBE0 estimations of the reduction potentials for the ground and ^{3}MLCT states confirm that the electron transfer to capturing molecules is favoured in the triplet excited state.

3.5 Future work

One of the most interesting features of $[Ru(bpy)_3]^{2+}$ and derivatives is their ability to transfer electrons to acceptor molecules. This opens the door to a wide range of applications for these compounds. In the present chapter we have taken advantage of the CAS State Interaction calculations in order to obtain the probability of ILET between different ligands. In this sense one could use the same approach to calculate the hopping integral between $[Ru(bpy)_3]^{2+}$-A and $[Ru(bpy)_3]^{3+}$-A^- states and estimate the electron-transfer probability. The acceptor molecule is usually an organic cation as 1,1'-dimethyl-4,4'-bipyridine^{2+} [1]. To this purpose, proper geometries with the complex interacting with the acceptor molecule are required. Molecular Dynamics which are out of the scope of this thesis are known to be a good method.

3.6 References

[1] C. Bock, T. Meyer, and D. Whitten, J. Am. Chem. Soc. **96**, 4710 (1974).

[2] C. Lin and N. SutinBock, J. Am. Chem. Soc. **97**, 3543 (1975).

[3] S.-M. Huang and H. Gafney, J. Phys. Chem. **81**, 2602 (1977).

[4] D. Meisel, M. Matheson, W. Mulac, and J. Rabani, J. Phys. Chem. **81**, 1449 (1977).

[5] R. Ballardini, G. Varani, M. Indelli, F. Scandola, and V. Balzani, J. Am. Chem. Soc. **100**, 7219 (1978).

[6] G. Favaro and F. Masetti, J. Phys. Chem. **83**, 2129 (1979).

[7] H. Sun and M. Hoffman, J. Phys. Chem. **98**, 11719 (1994).

[8] L. Hammarstrom, J. Alsins, A. Borje, T. Norrby, L. Zhang, and B. Akermark, J. Photochem. Photobiol., A **102**, 139 (1997).

[9] R. Watts, J. Chem. Educ. **60**, 834 (1983).

[10] I. Fujita and H. Kobayashi, Inorg. Chem. **12**, 2758 (1973).

[11] J. Demas and G. Crosby, J. Am. Chem. Soc. **93**, 2841 (1971).

[12] F. Bolletta, M. Maestri, and V. Balzani, J. Phys. Chem. **80**, 2499 (1976).

[13] J. Demas and D. Taylor, Inorg. Chem. **18**, 3177 (1979).

[14] R. Bensasson, C. Salet, and V. Balzani, J. Am. Chem. Soc. **98**, 3722 (1976).

[15] C. Daul, E. Baerends, and P. Vernooijs, Inorg. Chem. **33**, 3538 (1994).

[16] K. Zheng, J. Wang, W. Peng, X. Liu, and F. Yun, J. Mol. Struc.-Theochem **582**, 1 (2002).

[17] Z. Xie and W. Fang, J. Mol. Struc.-Theochem **717**, 179 (2005).

[18] A. Vlcek Jr. and S. Zalis, Coord. Chem. Rev. **251**, 258 (2007).

[19] T. Mukuta, N. Fukazawa, K. Murata, A. Inagaki, M. Akita, S. Tanaka, S. Koshihara, and K. Onda, Inorg. Chem. **53**, 2481 (2014).

[20] E. Ronca, F. De Angelis, and S. Fantacci, J. Phys. Chem. C **118**, 17067 (2014).

References

[21] C. Wawire, D. Jouvenot, F. Loiseau, P. Baudin, S. Liatard, L. Njenga, G. Kamau, and M. Casida, J. Photochem. Photobiol. A **276**, 8 (2014).

[22] S. Wallin, J. Davidsson, J. Modin, and L. Hammarstrom, J. Phys. Chem. A **109**, 4697 (2005).

[23] A. Yeh, C. Shank, and J. McCusker, Science **289**, 935 (2000).

[24] D. Hoff, R. Silva, and L. Rego, J. Phys. Chem. C **115**, 15617 (2011).

[25] F. Alary, J.-L. Heully, L. Bijeire, and P. Vicendo, Inorg. Chem. **46**, 3154 (2007).

[26] F. Alary, M. Boggio-Pasqua, J.-L. Heully, C. Marsden, and P. Vicendo, Inorg. Chem. **47**, 5259 (2008).

[27] J.-L. Heully, F. Alary, and M. Boggio-Pasqua, J. Chem. Phys. **131** (2009).

[28] M.-E. Moret, I. Tavernelli, M. Chergui, and U. Rothlisberger, Chem. Eur. J. **16**, 5889 (2010).

[29] J. McCusker, Acc. Chem. Res. **36**, 876 (2003).

[30] B. Dietzek, D. Akimov, W. Kiefer, S. Rau, J. Popp, and M. Schmitt, Laser Phys. Lett. **4**, 121 (2007).

[31] W. Henry, C. Coates, C. Brady, K. Ronayne, P. Matousek, M. Towrie, S. Botchway, A. Parker, J. Vos, W. Browne, et al., J. Phys. Chem. A **112**, 4537 (2008).

[32] A. Bhasikuttan, M. Suzuki, S. Nakashima, and T. Okada, J. Am. Chem. Soc. **124**, 8398 (2002).

[33] A. Cannizzo, F. van Mourik, W. Gawelda, G. Zgrablic, C. Bressler, and M. Chergui, Angew. Chem. Int. Ed. **45**, 3174 (2006).

[34] J. Van Houten and R. Watts, J. Am. Chem. Soc. **98**, 4853 (1976).

[35] P. Wagenknecht and P. Ford, Coord. Chem. Rev. **255**, 591 (2011).

[36] Q. Sun, S. Mosquera-Vazquez, L. Daku, L. Guenee, H. Goodwin, E. Vauthey, and A. Hausert, J. Am. Chem. Soc. **135**, 13660 (2013).

[37] J. Perdew, Phys. Rev. B **33**, 8822 (1986).

[38] A. Becke, Phys. Rev. A **38**, 3098 (1988).

[39] C. Lee, W. Yang, and R. Parr, Phys. Rev. B **37**, 785 (1988).

[40] A. Becke, J. Chem. Phys. **98**, 5648 (1993).

[41] J. Perdew and Y. Wang, Phys. Rev. B **45**, 13244 (1992).

[42] J. Perdew, K. Burke, and M. Ernzerhof, Phys. Rev. Lett. **77**, 3865 (1996).

[43] J. Perdew, M. Ernzerhof, and K. Burke, J. Chem. Phys. **105**, 9982 (1996).

[44] TURBOMOLE V6.6 2014, a development of University of Karlsruhe http://www.turbomole.com.

[45] T. Yanai, D. Tew, and N. Handy, Chem. Phys. Lett. **393**, 51 (2004).

[46] M. J. Frisch, G. W. Trucks, H. B. Schlegel, G. E. Scuseria, M. A. Robb, J. R. Cheeseman, G. Scalmani, V. Barone, B. Mennucci, G. A. Petersson, et al., Gaussian09, gaussian Inc. Wallingford CT 2009.

[47] A. Schafer, H. Horn, and R. Ahlrichs, J. Chem. Phys. **97**, 2571 (1992).

[48] D. Rillema and D. Jones, J. Chem. Soc. Chem. Commun. pp. 849–851 (1979).

[49] F. Weigend and R. Ahlrichs, Phys. Chem. Chem. Phys. **7**, 3297 (2005).

[50] A. Klamt and G. Schuurmann, J. Chem. Soc. Perkin Trans. 2 pp. 799–805 (1993).

[51] A. Schafer, A. Klamt, D. Sattel, J. Lohrenz, and F. Eckert, Phys. Chem. Chem. Phys. **2**, 2187 (2000).

[52] K. Pierloot, Int. J. Quantum Chem. **111**, 3291 (2011).

[53] G. Karlström, R. Lindh, P.-Å. Malmqvist, B. O. Roos, U. Ryde, V. Veryazov, P.-O. Widmark, M. Cossi, B. Schimmelpfennig, P. Neogrady, et al., Comput. Mater. Sci. **28**, 222 (2003).

[54] F. Aquilante, L. De Vico, N. Ferré, G. Ghigo, P.-Å. Malmqvist, P. Neogrady, T. B. Pedersen, M. Pitoňák, M. Reiher, B. O. Roos, et al., J. Comput. Chem. **31**, 224 (2010).

[55] P.-O. Widmark, M. P.-Å., and B. O. Roos, Theor. Chim. Acta **77**, 291 (1990).

[56] B. O. Roos, R. Lindh, P.-Å. Malmqvist, V. Veryazov, and P.-O. Widmark, J. Phys. Chem. A **108**, 2851 (2004).

[57] B. O. Roos, R. Lindh, P.-A. Malmqvist, V. Veryazov, and P.-O. Widmark, J. Phys. Chem. A **109**, 6575 (2005).

References

[58] K. Pierloot and S. Vancoillie, J. Chem. Phys. **125**, 124303 (2006).

[59] C. de Graaf and C. Sousa, Chem. Eur. J. **16**, 4550 (2010).

[60] A. Stoyanova, C. Sousa, C. De Graaf, and R. Broer, Int. J. Quantum Chem. **106**, 2444 (2006).

[61] L. Hozoi, S. Nishimoto, and C. de Graaf, Phys. Rev. B **75**, 1745051 (2007).

[62] L. Hozoi and M. Laad, Phys. Rev. Lett. **99**, 2564041 (2007).

[63] J. Malrieu, R. Caballol, C. Calzado, C. de Graaf, and N. Guihery, Chem. Rev. **114**, 429 (2013).

[64] P. Malmqvist and B. Roos, Chem. Phys. Lett. **155**, 189 (1989).

[65] H. Reiss and A. Heller, J. Phys. Chem. pp. 4207–4213 (1985).

[66] A. Bard and R. Larry, Electrochemical methods: Fundamentals and Applications (John Wiley & Sons, Inc., 2001).

[67] C. Bock, T. Meyer, and D. Whitten, J. Am. Chem. Soc. **97**, 2909 (1975).

Chapter 4

Light-induced excited state spin trapping in Ni porphyrin complexes

4.1 Introduction

Metalloporphyrins play a crucial role in many important biological processes. When they contain closed-shell metal centres their photochemistry is governed by the π electrons of the porphyrin ligand and the excited states can easily be detected by absorption spectroscopy. However, open-shell transition metal ions are much more frequent and in addition to the porphyrin $\pi - \pi^*$ excited states, low-lying d-d excitations may also play an important role in the photochemical reaction. These states are optically silent and complicate the study of the photo-processes of these complexes [1]. A typical metalloporphyrin of biological interest is the heme group in the active centre of myoglobin, hemoglobin and other synthetic functional analogues. The photochemistry of the Fe-porphyrin system has been subject of numerous studies and turns out to be rather complicated due to the presence of a large number of excited states in a narrow energy window. The smaller number of unpaired electrons in Ni^{II} ions should

in principle simplify the study of the photochemistry of Ni porphyrins. Moreover, the ionic radii of Ni and Fe are similar making the study of Ni porphyrins relevant to gain insight on the effect of the solvent or the intramolecular interactions on the proteins structure [2]. Therefore, Ni porphyrins have been extensively investigated during the 1980-90s decades as models to understand the structure and the photochemistry of the species involved in biological reactions [3–7]. After this initial boom the interest declined but the discovery of spin crossover in 2011 [8] put the Ni porphyrins back in the spotlights, now as a system of interest on its own [9–12].

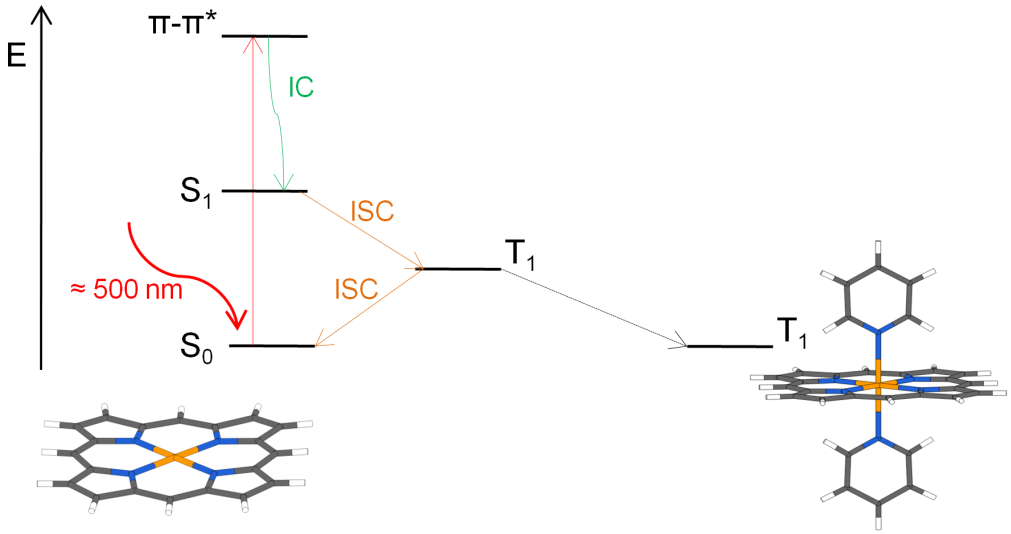

Figure 4.1. Schematic representation of the photochemical processes of Ni^{II} porphyrins. In non-coordinative solvents as toluene the system recovers the S_0 state by ISC from T_1 while in solvents as pyridine two molecules axially coordinate stabilizing the T_1 state.

When the $3d^8$ Ni^{II} ion is coordinated to a porphyrin ligand the $3d_{xy}$, $3d_{xz}$ and $3d_{yz}$ orbitals are always doubly occupied regardless of the spin coupling of the ground state. In contrast, the occupation of the $3d_{z^2}$ and $3d_{x^2-y^2}$ orbitals is not fixed. In non-coordinating solvents such as toluene the much larger stability of the $3d_{z^2}$ orbital induces a singlet ground state (S_0) characterized by doubly occupation of this orbital. Upon irradiation with light of around 500 nm wavelength a porphyrin π-π^* singlet excited state is triggered, which decays

in a few picoseconds by internal conversion (IC) to a metal centred excited singlet state (S_1) with $(3d_{z^2})^1$-$(3d_{x^2-y^2})^1$ electronic configuration. After less than 15 ps this state is converted through an intersystem crossing (ISC) to a triplet state (T_1) with the same electronic configuration. The ground state is recovered after approximately 250 ps and implies an ISC from T_1 to S_0 (see right part of Fig. 4.1) [13].

The situation is more complicated in solvents as pyridine because of the possibility to bind one or two axial ligands to the metal centre. This coordination is based on the σ interaction between the lone pair of the pyridine nitrogen (N_{py}) and electrons in the $3d_{z^2}$ Ni orbital. The interaction is large in the T_1 state due to the single-occupation of $3d_{z^2}$ orbital and rather weak in the closed shell singlet configuration with no electrons in this orbital. The Ni porphyrin remains in a four-fold coordination sphere in the ground state but two pyridines from the solvent coordinate to the Ni when the system reaches the T_1 state after irradiating it [14]. The coordination of the axial ligands closes the gap between the $3d_{z^2}$ and the $3d_{x^2-y^2}$ orbitals and stabilizes the square-pyramid T_1 state with respect to the square planar coordination. In consequence, the lifetime of the triplet state is considerably longer (10-20 ns [15, 16]) and can be considered to be trapped as in the LIESST process described in Chapter 1.

The existence of an intermediate five-coordinated Ni porphyrin in the relaxation path from the exited states of the square-planar complex to the octahedral T_1 structure is a controversial subject. Although the coexistence of five- and six-fold species is accepted in strong coordinating solvents like piperidine, the square-pyramidal complex has not been directly observed [17–19]. Only few theoretical studies have been reported, most of them based on DFT calculations, and only focusing on the square-planar Ni porphyrin, leaving unsolved the existence of the five-coordinated species [20–25].

This chapter describes the photochemistry of Ni porphyrins with four- and five-fold coordinated Ni^{II} ions. The geometrical changes upon pyridine coordination are studied with DFT and the relative energies of the singlet and triplet states are calculated by means of TD-DFT and CASPT2. The lifetimes of S_1 and T_1 in the four-coordinated complex are estimated with Fermi's golden rule and the thermal axial coordination mechanism is analyzed by potential energy scans.

4.2 The four-coordinated complex

4.2.1 S_0 ground state geometry optimization

DFT geometry optimizations have been carried out to elucidate the structural parameters of the Ni porphyrin S_0 ground state. Since one of the objectives of the chapter is to study the interactions of the complex with pyridine, one molecule of this ligand has been added to the calculations. Both porphyrin and pyridine are aromatic systems and π-π stacking is expected to play an important role. To evaluate it, the BP86 functional [26, 27] which does not take into account this effect and B3LYP [27–29] including the Grimme empirical dispersion correction (B3LYP+D3) [30–32] have been used, by means of the Turbomole package [33]. The def2-SVP [34] basis set has been used in the BP86 calculations and two basis sets have been compared in the B3LYP ones, the first one with def2-SVP for all atoms and the second one increasing to def2-TZVP [35, 36] the basis set of the Ni and N atoms.

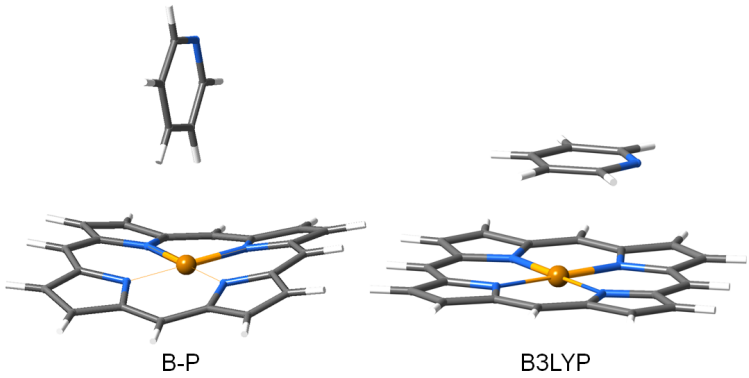

Figure 4.2. Comparison of the BP86 and B3LYP+D3 optimized S_0 geometries.

The effect of dispersion is shown in Fig. 4.2. Starting with the pyridine ring parallel to the Ni porphyrin, the poor description of the π-π interaction in the BP86 functional rotates the pyridine molecule to a perpendicular orientation to minimize the steric repulsion. Moreover, the porphyrin adopts a ruffled conformation with a Ni-N_{porph} distance of 1.95 Å. B3LYP+D3 maintains the parallel

orientation and a flat porphyrin conformation with d(Ni-N_{porph}) equal to 1.98 Å. The effect of adding a second pyridine molecule has been only analyzed with B3LYP+D3. The second ligand behaves in a similar way, remaining parallel on the other side of the porphyrin plane. Although no important differences have been detected when increasing the basis set size, the larger basis set in the dispersion corrected B3LYP functional does not imply important computational problems and will be used in this study.

4.2.2 Estimation of the excited states energetics and optimization of S_1 and T_1

Table 4.1 reports the TD-DFT/B3LYP vertical excitation energies of the lowest triplet (T_1) and several excited singlet states. As expected, T_1 is characterized by the promotion of one electron from the $3d_{z^2}$ to the $3d_{x^2-y^2}$ orbitals and is 0.53 eV above the singlet ground state. TD-DFT is required to evaluate the energies of the vertical singlet excited states. Since the full version of TD-DFT presents triplet instabilities, we have used the Tamm-Dancoff approximation [37] to calculate the energies of the excited states. As shown in Table 4.1, two degenerate S_5 and S_6 states are detected at 2.54 eV (488 nm), corresponding to excitations involving the π and π^* orbitals of porphyrin. The excited states with the highest oscillator strength are also of π-π^* nature and correspond to S_{17} and S_{18}, with energy around 3.8 eV (326 nm).

The four singlets found below the first π-π^* excitations are metal centred optically silent states which are expected to be populated by IC after the initial π-π^* excitation. The relative energies of these four singlets is in accordance with the ordering of the 3d-orbitals shown in Fig. 4.3 following from the ligand field reasoning for a square planar coordination.

Table 4.1. Vertical energies in eV and oscillator strengths from the S_0 ground state geometry (DFT for T_1 and TD-DFT for singlet excited states).

	configuration	relative energy	oscillator strength
S_0	$(3d_{z^2})^2$	0.00	
T_1	$(3d_{z^2})^1$-$(3d_{x^2-y^2})^1$	0.53	
S_1	$(3d_{z^2})^1$-$(3d_{x^2-y^2})^1$	1.80	0.00
S_2	$(3d_{xz})^1$-$(3d_{x^2-y^2})^1$	1.96	0.00
S_3	$(3d_{yz})^1$-$(3d_{x^2-y^2})^1$	1.97	0.00
S_4	$(3d_{xy})^1$-$(3d_{x^2-y^2})^1$	2.47	0.00
S_5	$(\pi_{porph})^1$-$(\pi_{porph}^*)^1$	2.54	$1.6{\cdot}10^{-3}$
S_6	$(\pi_{porph})^1$-$(\pi_{porph}^*)^1$	2.54	$2.0{\cdot}10^{-3}$
S_7	$(\pi_{porph})^1$-$(3d_{x^2-y^2})^1$	2.76	0.00
S_8	$(\pi_{porph})^1$-$(3d_{x^2-y^2})^1$	2.83	0.00
S_9	$(3d_{z^2})$-$(\pi_{porph}^*)^1$	3.11	$9.5{\cdot}10^{-4}$
S_{10}	$(3d_{z^2})^1$-$(\pi_{porph}^*)^1$	3.12	$9.5{\cdot}10^{-4}$
S_{11}	$(3d_{xz,yz})^1$-$(\pi_{porph}^*)^1$	3.14	0.00
S_{12}	$(3d_{xz,yz})^1$-$(\pi_{porph}^*)^1$	3.20	$5.0{\cdot}10^{-5}$
S_{13}	$(3d_{xz,yz})^1$-$(\pi_{porph}^*)^1$	3.27	$3.0{\cdot}10^{-5}$
S_{14}	$(3d_{xz,yz})^1$-$(\pi_{porph}^*)^1$	3.54	$7.7{\cdot}10^{-4}$
S_{15}	$(\pi_{porph})^1$-$(n_{py}^*)^1$	3.73	$5.5{\cdot}10^{-2}$
S_{16}	$(\pi_{porph})^1$-$(n_{py}^*)^1$	3.73	$5.7{\cdot}10^{-2}$
S_{17}	$(\pi_{porph})^1$-$(\pi_{porph}^*)^1$	3.83	0.21
S_{18}	$(\pi_{porph})^1$-$(\pi_{porph}^*)^1$	3.85	0.39
S_{19}	$(\pi_{porph})^1$-$(\pi_{porph}^*)^1$	3.88	$7.2{\cdot}10^{-3}$
S_{20}	$(\pi_{porph})^1$-$(\pi_{porph}^*)^1$	3.90	0.18
S_{21}	$(\pi_{porph})^1$-$(\pi_{porph}^*)^1$	4.02	$3.0{\cdot}10^{-2}$
S_{22}	$(\pi_{porph})^1$-$(\pi_{porph}^*)^1$	4.03	$4.3{\cdot}10^{-2}$

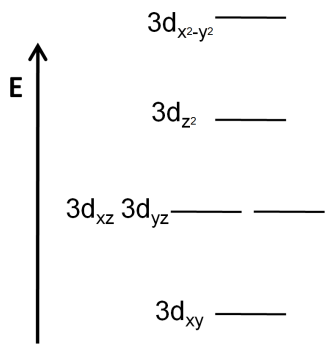

Figure 4.3. Ordering of the 3d-orbitals of a metal centre in a square-planar ligand field.

The geometries of T_1 and S_1 have been optimized with DFT and TD-DFT respectively. Since both states present the same electronic configuration, their structures are practically identical although it should be stressed that the T_1 structure is a local minimum. In the global minimum the pyridine is axially coordinated to Ni, but this will be discussed later in this chapter. The most important difference with respect to the ground state geometry is the increase of the Ni-N_{porph} distance from 1.98 Å in S_0 to 2.05 Å. The lengthening of the coordination distance is reasonable taking into account that in S_1 and T_1 one electron occupies the $3d_{x^2-y^2}$ orbital, which is anti-bonding with respect to the Ni-N_{porph} bond [38] as illustrated in Fig. 4.4 on the right. More intriguing is the fact that the carbon atoms of the pyridine ring get slightly closer to the complex and in consequence the ligand is no longer completely parallel to the porphyrin plane. This behaviour can be explained by looking at the second orbital with an unpaired electron shown on the left in Fig. 4.4. This orbital is basically of Ni-$3d_{z^2}$ character but has an out-of-phase contribution from a π orbital of the pyridine. Among the doubly occupied orbitals one can find the corresponding in-phase combination, largely localized on pyridine but with a non-negligible contribution of the Ni-$3d_{z^2}$ orbital. This mixing is completely absent in the S_0 state. The geometry relaxation stabilizes both states by 0.24 eV with respect to the vertical energies previously reported in Table 4.1.

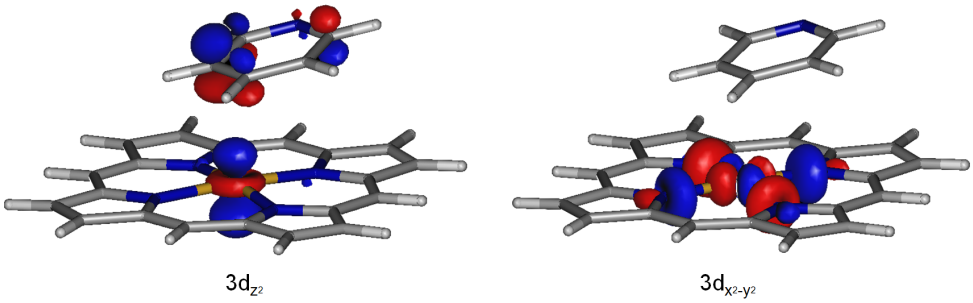

Figure 4.4. Representation of $3d_{z^2}$ and $3d_{x^2-y^2}$ orbitals in the T_1 and S_1 optimized geometry.

4.2.3 Multiconfigurational calculations

We now turn our attention to the multiconfigurational description of the electronic structure. Provided that the basis set and wave function expansion are

properly chosen, CASPT2 gives very accurate relative energies in most cases. As will be shown below, the basic Gouterman model [39–41], which only considers the two highest π and the two lowest π^* orbitals, is not good enough to describe the porphyrin centred π-π^* excitations and more orbitals have to be included in the active space of the CASSCF calculations. The 'minimal' active space for correctly addressing the vertical spectrum of porphyrins consists of 8 π and 6 π^* orbitals [42]. On the other hand, to correctly describe the metal centred excited states (most importantly, S_0 and T_1) 10 electrons in 11 orbitals need to be included. Hence, a complete account of the excited states of Ni porphyrin requires a [26,25]-CAS. This is clearly beyond the limits of CASSCF and the excited states have to be calculated by parts.

All the calculations presented here have been performed with the Molcas package [43, 44]. The basis sets used are of the atomic natural orbitals type [45–47]. For the porphyrin centred excited states, the most relevant atoms in the Ni porphyrin system (Ni and N) are described with a TZVP basis set, while the more peripheral atoms (C and H) have a basis set of double-zeta quality. The metal centred excited states require a more accurate description and in this case the basis set for carbon atoms is also of TZVP quality.

The π-π^* vertical excitation

The characterization of excited states is easier if symmetry is used. For this purpose, the pyridine moiety has been omitted in the calculations from the present section and the Ni-porphyrin presents D_{2h} point group symmetry. Two different active spaces have been compared to describe the π-π^* vertical excitation energies. The first one is a [4,4]-CAS and corresponds to the Gouterman model [39–41] including two π orbitals with b_{2g} and b_{3g} and two π^* orbitals with a_u and b_{1u} symmetries, respectively. The second one expands the set to 14 active orbitals by adding two pairs of π-π^* orbitals (b_{2g} and b_{3g}), a pair of π-π^* orbitals (a_u) and a set of 3 π and 1 π^* orbitals (b_{1u}).

Table 4.2 lists the four lowest $\pi \rightarrow \pi^*$ excitations of the Ni-porphyrin system. The first 1^1B_{2u} and 1^1B_{3u} states correspond to the S_5 and S_6 excitations

calculated with TD-DFT (see Table 4.1) and are assigned to the Q band of the Ni porphyrin absorption spectrum. Taking into account that the experimental energy of these excitations is around 2.5 eV (500 nm) depending on the peripheral substituents of the porphyrin ring and the solvent [16], one can conclude that the Gouterman model is insufficient to describe these energies and the description needs to be improved. The extension of the active space to 16 electrons in 14 orbitals lowers the CASPT2 relative energies of these states by ≈ 0.6 eV and brings them in good agreement with experiment and TD-DFT. A similar behaviour is found for the higher-lying singlet states 2^1B_{2u} and 2^1B_{3u}. The final CASPT2 energies and the large oscillator strength of these excitations are compatible with the assignment to the intense Soret band which experimentally appears around 3.2 eV (390 nm) in the Ni porphyrin spectrum.

Table 4.2. [4,4]- and [16,14]-CASSCF and CASPT2 vertical excitation energies in eV of Ni porphyrin.

	CASSCF	CASPT2	Oscillator strength
[4,4] active space			
$1\ ^1B_{2u}$	3.77	3.30	$8.26{\cdot}10^{-2}$
$1\ ^1B_{3u}$	3.80	3.29	$2.34{\cdot}10^{-2}$
$2\ ^1B_{2u}$	5.34	4.66	2.51
$2\ ^1B_{3u}$	5.30	4.66	2.51
[16,14] active space			
$1\ ^1B_{2u}$	3.72	2.66	$1.45{\cdot}10^{-2}$
$1\ ^1B_{3u}$	3.09	2.73	$1.58{\cdot}10^{-2}$
$2\ ^1B_{2u}$	5.54	3.70	1.18
$2\ ^1B_{3u}$	4.42	4.08	0.22

The d-d states

The d-d excited states relative energies will be compared for the four- and five-coordinated Ni porphyrin further in this work. For this reason, in the present section the DFT and TD-DFT optimized geometries incorporating a pyridine are used. As a consequence, the system does not present any symmetry. To select the appropriate size of the active space the energy difference between the S_0 ground state and the vertical T_1 state has been calculated using three

different active spaces. The first one only includes the $3d_{z^2}$ and $3d_{x^2-y^2}$ orbitals which are singly occupied in T_1. The second extends the first by including the five 3d orbitals and an extra set of 4d orbitals to account for the double-shell effect (8 electrons in 10 orbitals). In the third a σ orbital of the N_{porph} is added to the 3d and 4d orbitals (10 electrons in 11 orbitals). With all three active spaces T_1 is more stable than S_0 at the CASSCF level. However, the increase of the active space and the inclusion of the external electron correlation up to second order tends to lower the energy gap between these states. [10,11]-CASPT2 is the only calculation which gives S_0 more stable than T_1.

Table 4.3 shows the results of the multiconfigurational calculations performed using the DFT (for S_0 and T_1) and TD-DFT (for S_1) optimized geometries. As mentioned, T_1 is lower than the ground state at the [10,11]-CASSCF level but this relative stability is inverted with CASPT2. The optimized S_1 and T_1 geometries are very close and so are the corresponding relative energies of the different states at these two points.

Table 4.3. [10,11]-CASSCF and CASPT2 energies in eV of four-coordinated Ni porphyrin S_0, S_1 and T_1 states.

	configuration	[10,11]-CASSCF	CASPT2
S_0 geometry			
S_0	$(3d_{z^2})^2$	0.00	0.00
S_1	$(3d_{z^2})^1$-$(3d_{x^2-y^2})^1$	1.80	1.89
T_1	$(3d_{z^2})^1$-$(3d_{x^2-y^2})^1$	-0.28	0.23
S_1 geometry			
S_0	$(3d_{z^2})^2$	0.48	0.31
S_1	$(3d_{z^2})^1$-$(3d_{x^2-y^2})^1$	1.85	1.75
T_1	$(3d_{z^2})^1$-$(3d_{x^2-y^2})^1$	-0.26	0.08
T_1 geometry			
S_0	$(3d_{z^2})^2$	0.47	0.31
S_1	$(3d_{z^2})^1$-$(3d_{x^2-y^2})^1$	1.84	1.74
T_1	$(3d_{z^2})^1$-$(3d_{x^2-y^2})^1$	-0.27	0.08

These results provide a precise map of the position of the d-d states on the B3LYP/CASPT2 potential energy surface. S_1 is located 1.89 eV higher than S_0 in the Franck-Condon geometry and 1.75 eV after geometry relaxation. T_1 lies

0.23 eV above S_0 in the ground state geometry but becomes the most stable state in its relaxed geometry. The energy of the relaxed T_1 is 0.08 eV higher than the relaxed S_0 and it confirms that the closed-shell configuration is the global minimum, and hence, the ground state.

4.2.4 Intersystem crossing rates

The lifetime of excited states is an important feature to get a complete view of the photochemistry of square-planar Ni porphyrins. The ISC rates are estimated following the scheme explained in Chapter 2. The frequencies required for this estimation are taken from the DFT and TD-DFT optimizations of the different states while the energy differences and spin-orbit coupling (SOC) between them are calculated using the [10,11]-CASSCF wave function and the corresponding CASPT2 energies.

After the π-π^* bright excitation, the system decays *via* IC to the S_1 state. This process is experimentally expected to happen in approximately 10 ps. One has to go beyond the formalism of the Fermi's golden rule to address IC computationally. This is beyond the scope of this work. Once at S_1, the system undergoes an ISC to T_1 and recovers S_0 after a second ISC. The rates of $S_1 \rightarrow T_1$ and $T_1 \rightarrow S_0$ are the objective of this section. The ISCs are possible due to the SOC between the states with different spin multiplicity. Table 4.4 summarizes the results of the two ISC processes. The SOC between S_1 and T_1 with the same configuration is considerably larger than between T_1 and S_0. Furthermore, the practically identical geometry of S_1 and T_1 makes that the vibrational term in the expression of the ISC rate is an order of magnitude larger than for the ISC from T_1 to S_0. In consequence, the calculated $S_1 \rightarrow T_1$ ISC rate is considerably larger than for the $T_1 \rightarrow S_0$ process. The computational estimates are in good agreement with experimental values.

Table 4.4. Estimation of the ISC rates. Vibrational term in $cm^2 \cdot s^{-1}$, spin-orbit coupling in cm^{-1}, rate constant (k_{ISC}) in s^{-1} and lifetime in ps. Experimental values in parenthesis [16].

	vibrational term	SOC term	k_{ISC}	lifetime
$S_1 \rightarrow T_1$	475808893	23	$2.5 \cdot 10^{11}$	4 ($\approx$ 10)
$T_1 \rightarrow S_0$	64104829	6	$2.3 \cdot 10^{9}$	433 ($\approx$ 250)

4.3 The five-coordinated complex

4.3.1 T_1 ground state geometry optimization

Following the same computational scheme, the five-coordinated geometry in its T_1 ground state has been optimized at the B3LYP level of calculation. The Ni-N_{porph} distance is 2.08 Å, similar to the four-coordinated T_1. The axial coordination distance (Ni-N_{py}) is 2.09 Å. The coordination of the axial ligand pushes the Ni atom out of the porphyrin plane resulting in a small doming distortion of the porphyrin plane. The axial coordination bond is formed by σ-interaction from the doubly-occupied N_{py} lone pair orbital to the singly-occupied $3d_{z^2}$ orbital. Furthermore, π interactions involving the doubly-occupied $3d_{xz,yz}$ and pyridine orbitals reinforce the Ni-N bond (see Fig. 4.5) [48].

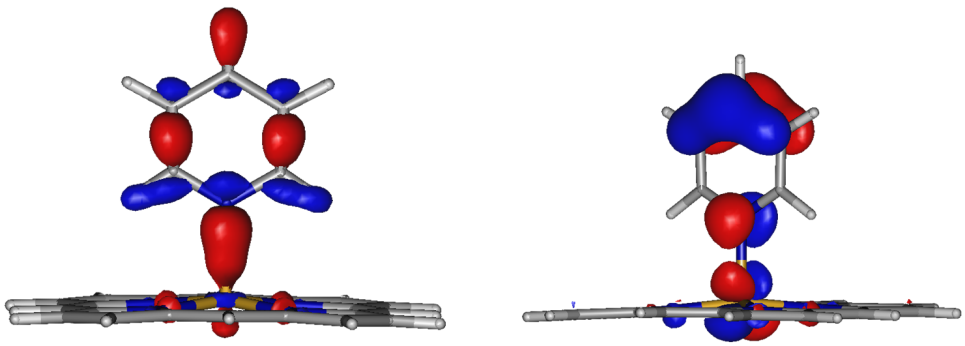

Figure 4.5. Representation of σ (left) and π orbitals (right) in the five-coordinated complex.

No five-coordinated minimum has been found on the S_0 potential energy surface. When this geometry is optimized in the singlet state the pyridine is released and placed parallel to the porphyrin ring so that the four-coordinated geometry is recovered. The instability of the five-coordinated complex in S_0 is due to the double occupancy of $3d_{z^2}$ [15]. The five-coordinated T_1 ground state is 0.21 eV more stable than the four-coordinated S_0 at this level of calculation, and hence, is the global minimum.

DFT geometry optimizations are not completely reliable since they have been performed in gas phase. The solvent is expected to stabilize the four-coordinated

singlet with respect to the five-coordinated triplet. For this reason, the S_0 uncoordinated and the T_1 coordinated geometries have been re-optimized including the effects of the solvent. The COSMO model [49, 50] implemented in the Turbomole package has been used with pyridine as solvent. The obtained geometries are practically identical with respect to those resulting from the gas phase optimizations. The four-coordinated S_0 is stabilized only 0.03 eV by the solvent effect.

4.3.2 Multiconfigurational calculations

In a similar way as for the four-coordinated complex, [10,11]-CASSCF and CASPT2 calculations have been carried out using the optimized geometry of the pentacoordinated T_1 state (see Table 4.5). In accordance with the previous DFT results, at the CASPT2 level the five-coordinated T_1 is more stable than the four-coordinated S_0 by 0.33 eV. The axial coordination involves the interaction of the singly occupied $3d_{z^2}$ and the doubly occupied pyridine lone pair orbital. This interaction results in two electrons in the bonding and one in the anti-bonding combination of these orbitals and the overall energy decreases with respect to the unbounded situation [51]. Apparently the π-π interactions do not sufficiently stabilize the S_0 state to make this state the global minimum in the chosen representation of the system.

Table 4.5. [10,11]-CASSCF and CASPT2 energies in eV relative to the four-coordinated S_0 of five-coordinated Ni porphyrin T_1, S_0 and S_1 states.

	configuration	[10,11]-CASSCF	CASPT2
five-coordinated T_1			
T_1	$(3d_{z^2})^1$-$(3d_{x^2-y^2})^1$	-0.83	-0.33
S_0	$(3d_{z^2})^2$	0.63	0.71
S_1	$(3d_{z^2})^1$-$(3d_{x^2-y^2})^1$	1.31	1.37

Since the global minimum corresponds to the five-coordinated complex instead of the four-coordinated system, the Ni porphyrin should become five-coordinated in a pyridine solution without the necessity of exciting the complex. This observation is in contradiction with the expected LIESST mechanism in

these systems, and hence, the thermal axial coordination of the pyridine ligand to the Ni metal centre requires to be explored.

4.3.3 Thermal pyridine axial coordination

To obtain more information about the thermal axial coordination mechanism of the Ni porphyrin in pyridine the Ni-N_{py} distance has been scanned in both S_0 and T_1 states. In each point of the coordinate the structure has been relaxed in the singlet and triplet states at B3LYP level and the energies have been calculated with [10,11]-CASPT2. The results are plotted in Fig. 4.6.

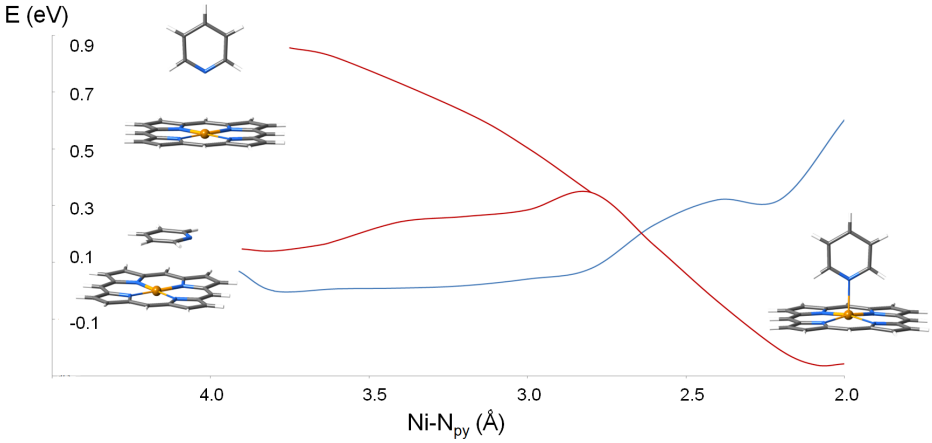

Figure 4.6. [10,12]-CASPT2 energies at B3LYP optimized S_0 (blue line) and T_1 (red lines) geometries for fixed Ni-N_{py} distances.

The blue curve shows the energy profile of the S_0 state, which is steadily increasing from the minimum with the pyridine molecule parallel to the porphyrin plane to the situation with a tilted pyridine. The loss of π-π interactions destabilizes the S_0 state. The red lines show two different profiles of the T_1 state. The upper one represents the perpendicular approach of the pyridine to the Ni ion while in the lower one the pyridine is initially oriented in a parallel manner. Due to a tilting movement, the two situations converge. The coordination of the pyridine at the axial position leads to a rather large energy gain and

makes the pentacoordinated T_1 state 0.33 eV more stable than the S_0 state in concordance with the DFT findings discussed above.

The S_0 and T_1 potential energy curves cross at a Ni-N_{py} distance close to 2.6 Å. This point gives an estimate of 0.2 eV for the barrier of the thermal pyridine coordination. This suggests a low thermal rate for axial coordination and the need of light irradiation to make effective the coordination of one or two pyridine ligands. Interestingly enough, the barrier for the release of the pyridine ligand is even higher, implying that the pentacoordinated T_1 state populated after the light pulse is thermally trapped as occurs in the LIESST process described in Chapter 1 for the Fe^{II} complexes.

4.4 Conclusions

This chapter discusses a computational scheme to study the photochemistry of Ni porphyrin complexes in pyridine, which is key in the LIESST of these systems. Comparison of the DFT optimized geometries with and without taking into account the dispersion forces reveals the importance of π-π stacking between the porphyrin and the pyridine aromatic rings. For this reason, the use of a functional with dispersion correction is strongly recommended. In order to obtain accurate estimations of the energy of the states involved in the LIESST process, CASSCF and CASPT2 calculations have been carried out. Since the size of the calculation required to study all states simultaneously makes it unfeasible two different active spaces have been used. On one hand, a [16,14] active space is required to estimate the porphyrin π-π^* excitations. On the other hand, a [10,11] active space is the best choice to calculate the metal centre d-d states.

DFT and TD-DFT optimizations of the four-fold T_1 and S_1 lead to practically identical geometries since both states present the same electronic configuration. For this reason the SOC between them is larger than the coupling between T_1 and S_0. As a consequence, the ISC rate is considerably larger in the $S_1 \rightarrow T_1$ process.

The five-coordinated Ni porphyrin has been optimized in its T_1 ground state and estimated to be the global minimum. Since no stable geometry has been found for the five-coordinated S_0 it is confirmed that with closed-shell configurations no axial ligand can be bound to the Ni porphyrin complex. The system remains uncoordinated in pyridine solution since a significant energy barrier has been detected for the thermal axial coordination mechanism. Even larger is the barrier for the ligand release in the T_1 five-coordinated geometry and one can conclude that the triplet state is trapped by axial coordination of a pyridine molecule.

4.5 References

[1] P. Brodard and E. Vauthey, Chem. Phys. Lett. **309**, 198 (1999).

[2] A. Cupane, M. Leone, L. Cordone, H. Gilch, W. Dreybrodt, E. Unger, and R. Schweitzer-Stenner, J. Phys. Chem. **100**, 14192 (1996).

[3] M. Hoshino, Inorg. Chem. **25**, 2476 (1986).

[4] J. Rodriguez, C. Kirmaier, and D. Holten, J. Am. Chem. Soc. **111**, 6500 (1989).

[5] S. Kruglik, Y. Mizutani, and T. Kitagawa, Chem. Phys. Lett. **266**, 283 (1997).

[6] C. Drain, S. Gentemann, J. Roberts, N. Nelson, C. Medforth, S. Jia, M. Simpson, K. Smith, J. Fajer, J. Shelnutt, et al., J. Am. Chem. Soc. **120**, 3781 (1998).

[7] Y. Mizutani, Y. Uesugi, and T. Kitagawa, J. Chem. Phys. **111**, 8950 (1999).

[8] S. Thies, H. Sell, C. Schuett, C. Bornholdt, C. Naether, F. Tuczek, and R. Herges, J. Am. Chem. Soc. **133**, 16243 (2011).

[9] D. Achey and G. Meyer, Inog. Chem. **52**, 9574 (2013).

[10] H. Ma, J. Petersen, V. Young, Jr., G. Yee, and M. Jensen, J. Am. Chem. Soc. **133**, 5644 (2011).

[11] M. Dommaschk, F. Gutzeit, S. Boretius, R. Haagc, and R. Herges, Chem. Commun. **50**, 12476 (2014).

[12] M. Dommaschk, M. Peters, F. Gutzeit, C. Schuett, C. Naether, F. Soennichsen, S. Tiwar, C. Riedel, S. Boretius, and R. Herges, J. Am. Chem. Soc. **137**, 7552 (2015).

[13] E. Findsen, J. Shelnutt, and M. Ondrias, J. Phys. Chem. **92**, 307 (1988).

[14] J. Rodriguez and D. Holten, J. Chem. Phys. **92**, 5944 (1990).

[15] D. Kim and D. Holten, Chem. Phys. Lett. **98**, 584 (1983).

[16] D. Kim, C. Kirmaier, and D. Holten, Chem. Phys. **75**, 305 (1983).

[17] S. Jia, W. Jentzen, M. Shang, X. Song, J. Ma, W. Scheidt, and J. Shelnutt, Inorg. Chem. **37**, 4402 (1998).

[18] S. Kruglik, V. Ermolenkov, V. Orlovich, and P. Turpin, Chem. Phys. **286**, 97 (2003).

[19] L. Campbell, S. Tanaka, and S. Mukamel, Chem. Phys. **299**, 225 (2004).

[20] M. Liao and S. Scheiner, J. Chem. Phys. **117**, 205 (2002).

[21] A. Rosa, G. Ricciardi, E. Baerends, and S. van Gisbergen, J. Phys. Chem. A **105**, 3311 (2001).

[22] S. Patchkovskii, P. Kozlowski, and M. Zgierski, J. Chem. Phys. **121**, 1317 (2004).

[23] A. Rosa, G. Ricciardi, E. Baerends, M. Zimin, M. Rodgers, S. Matsumoto, and N. Ono, Inorg. Chem. **44**, 6609 (2005).

[24] E. Baerends, G. Ricciardi, A. Rosa, and S. van Gisbergen, Coord. Chem. Rev. **230**, 5 (2002).

[25] A. Zamyatin, A. Soldatova, and M. Rodgers, Inorg. Chim. Acta **360**, 857 (2007).

[26] J. Perdew, Phys. Rev. B **33**, 8822 (1986).

[27] A. Becke, Phys. Rev. A **38**, 3098 (1988).

[28] C. Lee, W. Yang, and R. Parr, Phys. Rev. B **37**, 785 (1988).

[29] A. Becke, J. Chem. Phys. **98**, 5648 (1993).

[30] S. Grimme, J. Comput. Chem. **25**, 1463 (2004).

[31] S. Grimme, J. Comput. Chem. **27**, 1787 (2006).

[32] S. Grimme, J. Antony, S. Ehrlich, and H. Krieg, J. Chem. Phys. **132**, 154104 (2010).

[33] TURBOMOLE V6.6 2014, a development of University of Karlsruhe http://www.turbomole.com.

[34] A. Schafer, H. Horn, and R. Ahlrichs, J. Chem. Phys. **97**, 2571 (1992).

[35] F. Weigend, M. Haser, H. Patzelt, and R. Ahlrichs, Chem. Phys. Lett. **294**, 143 (1998).

[36] F. Weigend and R. Ahlrichs, Phys. Chem. Chem. Phys. **7**, 3297 (2005).

[37] S. Hirata and M. Head-Gordon, Chem. Phys. Lett. **314**, 291 (1999).

[38] L. Chen, X. Zhang, E. Wasinger, K. Attenkofer, G. Jennings, A. Muresan, and J. Lindsey, J. Am. Chem. Soc. **129**, 9616 (2007).

References

[39] M. Gouterman, J. Chem. Phys. **30**, 1139 (1959).

[40] M. Gouterman, G. H. Wagnière, and L. C. Snyder, J. Mol. Spectrosc. **11**, 108 (1963).

[41] C. Weiss, H. Kobayashi, and M. Gouterman, J. Mol. Spectrosc. **16**, 415 (1965).

[42] L. Serrano-Andrés, M. Merchán, M. Rubio, and B. O. Roos, Chem. Phys. Lett. **295**, 195 (1998).

[43] G. Karlström, R. Lindh, P.-Å. Malmqvist, B. O. Roos, U. Ryde, V. Veryazov, P.-O. Widmark, M. Cossi, B. Schimmelpfennig, P. Neogrady, et al., Comput. Mater. Sci. **28**, 222 (2003).

[44] F. Aquilante, L. De Vico, N. Ferré, G. Ghigo, P.-Å. Malmqvist, P. Neogrady, T. B. Pedersen, M. Pitoňák, M. Reiher, B. O. Roos, et al., J. Comput. Chem. **31**, 224 (2010).

[45] P.-O. Widmark, M. P.-Å., and B. O. Roos, Theor. Chim. Acta **77**, 291 (1990).

[46] B. O. Roos, R. Lindh, P.-Å. Malmqvist, V. Veryazov, and P.-O. Widmark, J. Phys. Chem. A **108**, 2851 (2004).

[47] B. O. Roos, R. Lindh, P.-A. Malmqvist, V. Veryazov, and P.-O. Widmark, J. Phys. Chem. A **109**, 6575 (2005).

[48] S. Thies, C. Bornholdt, F. Koehler, F. Soennichsen, C. Naether, F. Tuczek, and R. Herges, Chem. Eur. J. **16**, 10074 (2010).

[49] A. Klamt and G. Schuurmann, J. Chem. Soc. Perkin Trans. 2 pp. 799–805 (1993).

[50] A. Schafer, A. Klamt, D. Sattel, J. Lohrenz, and F. Eckert, Phys. Chem. Chem. Phys. **2**, 2187 (2000).

[51] Y. Uesugi, Y. Mizutani, and T. Kitagawa, J. Phys. Chem. A **102**, 5809 (1998).

Light-induced excited state spin trapping in Ni porphyrin complexes

Chapter 5

Coordination-induced spin-crossover in a Ni porphyrin complex

5.1 Introduction

Room-temperature SCO has been reported for Ni-tetrakis(pentafluorophenyl)-porphyrin (NiTPP) functionalized with a phenylazopyridine (PAPy) arm [1], see Fig. 5.1. Under standard conditions, the NiTPP-PAPy complex is low-spin (S=0) and NMR experiments, among other characterization techniques, indicate a four-coordinated Ni^{II} in a square planar geometry with a *trans* configuration of the PAPy arm. Upon irradiation at 500 nm, the compound becomes paramagnetic and rearranges to a five-coordinated complex where the pyridine moiety coordinates axially to Ni, which becomes high-spin. The SCO process in this Ni-porphyrin is reversible upon irradiation at 435 nm, while the thermal back reaction is very slow.

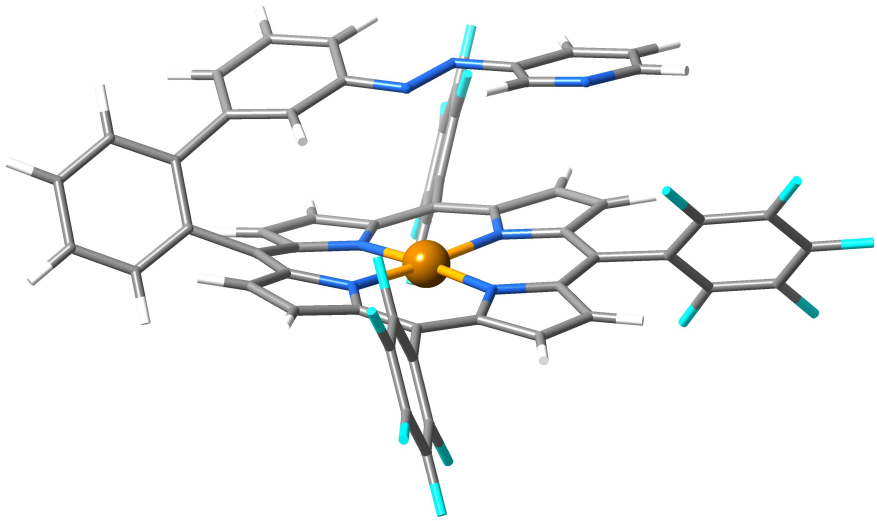

Figure 5.1. Ni-tetrakis(pentafluorophenyl)porphyrin with a phenylazopyridine functionalized axial arm (NiTPP-PAPy).

In the original study by the group of Herges, the SCO was reported to be triggered by the *trans-cis* isomerization of the N=N bond of the PAPy arm. Irradiation at 500 nm induces a π-π^* excitation on the azo group and the PAPy arm evolves to the *cis* isomer. This orients the non-bonding electron pair of pyridine nitrogen perpendicularly to the Ni-porphyrin plane, making possible the coordination of the arm to Ni. The assignment of the paramagnetic product as a five-coordinated Ni ion with the PAPy arm in the *cis* form was based on NMR Overhauser experiments, indicating that the Ni-H distance of the two hydrogen adjacent to the nitrogen of the pyridine ring is identical for both H atoms and significantly smaller than in the initial complex. The five-coordination of the Ni^{II} ion induces a spin change to S=1, further stabilized by the electron withdrawing pentafluorophenyl groups attached to the porphyrin ring that lower the energy of the $3d_{x^2-y^2}$ orbital and decrease the gap with the $3d_{z^2}$ orbital [2]. Upon irradiation with visible light (435 nm) or by heating the sample, the PAPy arm recovers the initial *trans* conformation and the pyridine group dissociates from Ni, which turns back to its initial low-spin configuration.

However, this description of the coordination-induced spin-crossover (CISCO) leaves a few points open to discussion. The most important one is the fact that

the irradiation used to induce the HS state is significantly red-shifted (∼135 nm) with respect to the wavelength normally used for *cis-trans* isomerizations of N=N double bonds. In fact, the 500 nm irradiation used in the experiments is typical for the Q band absorption of porphyrins. A second point is related to the indirect characterization of the *cis* conformation of the arm in the paramagnetic product, which is based on measurements on the diamagnetic Zn-analogue of the NiTPP-PAPy complex. Furthermore, the PBE functional used in the density functional theory (DFT) geometry optimizations may not be the most appropriate choice given the large π-systems of the porphyrin ring and the PAPy arm. The interaction between π-systems is in general not accurately described with standard GGA functionals.

Light-induced SCO in simpler Ni^{II} porphyrins in basic solvents as pyridine has been studied in Chapter 4. The mechanism goes through the 500 nm excitation in the Q band from the closed-shell singlet ground state (S_0) to a π-π^* excited singlet state. The singlet excited state relaxes through internal conversion followed by an intersystem crossing to T_1. A solvent molecule is then axially coordinated to the Ni^{II} and the five-coordinated species stabilizes the T_1 state [3–6]. This seems *a priori* a more consistent mechanism for the NiTPP-PAPy.

The aim of this chapter is to gain more insight into the details of the CISCO mechanism of NiTPP-PAPy. We clarify the origin of the 500 nm irradiation that triggers the SCO and discuss the geometries and relative stabilities of several *cis* and *trans* isomers of the complex in LS and HS configurations. For this purpose, we apply DFT/M06-2X calculations to optimize the geometries combined with CASPT2 calculations for accurate energetics.

5.2 Conformational analysis

To rationalize the SCO process, Venkataramani *et al.* [1] performed DFT calculations on a series of potentially suitable molecular structures. They used the PBE functional [7, 8] and found several minima for *cis* and *trans* four-coordinated and five-coordinated NiTPP-PAPy. For this last coordination only a stable structure was found with the *cis* configuration of the PAPy arm. Since

the π-π interactions between porphyrin and PAPy arm can be determinant for the relative stabilities of the different confomers, we compare standard BP86 [9, 10] results, which are expected to be similar to PBE, with those obtained with the dispersion corrected functional M06-2X [11]. In this way we can access the importance of the π-π interactions and locate the minimum structure of the five-coordinated complex with the PAPy arm in *trans*.

The DFT calculations are performed with the Gaussian package [12]. A triple zeta valence + polarization (TZVP) [13] basis set was used for the Ni ion and basis sets of split-valence + polarization (SVP) quality [14] for the rest of the atoms. Solvent effects were included by means of the COSMO model [15, 16] using the dielectric constant of dimethyl sulfoxide (ϵ=46.7) to mimic the experimental conditions.

Table 5.1. BP86 and M06-2X Ni-$N_{pyridine}$ distances (in Å) and relative energies (in eV) for several conformations of PAPy-NiTPP. Square planar (sqp) conformations are singlet and have four-fold Ni coordination. Square pyramid (spy) conformers are triplet and five-coordinated.

	Ni-$N_{pyridine}$ distance		**Relative energy**	
	BP86	**M06-2X**	**BP86**	**M06-2X**
trans-sqp	6.99	4.36	-0.81	0.42
trans-sqp open	12.34	11.52	-0.81	0.72
cis-sqp	4.30	2.62	-0.25	0.91
cis-sqp open	9.44	9.39	-0.23	1.32
trans-spy	2.08	2.17	0.15	0.28
cis-spy	2.08	2.16	0.00	0.00

Table 5.1 reports M06-2X relative energies and the Ni-$N_{pyridine}$ distance of the different minima found for both *cis* and *trans* PAPy arm configurations. The BP86 optimized metal-nitrogen distance and relative energies are also reported for comparison. All square planar structures (sqp) have the Ni^{2+} ion in a four-fold coordination mode and a singlet ground state and the square pyramid complexes (spy) have pentacoordinated Ni^{2+} and are triplet. The M06-2X optimized structures are represented in Fig. 5.2. The conformer with the PAPy group in *trans* (*trans*-sqp) is the most stable singlet structure, and

the triplet state of the five-coordinated structure with *cis* PAPy arm (*cis*-spy) is the absolute minimum of the whole set. As a general feature, the axial coordination slightly enlarges the distance between Ni and the N_{porph}, from 1.99 to 2.06 Å. This lengthening of the bond can be easily related to the single occupancy of the $3d_{x^2-y^2}$ orbital (of Ni-N antibonding character) in the HS state, being empty in the LS state.

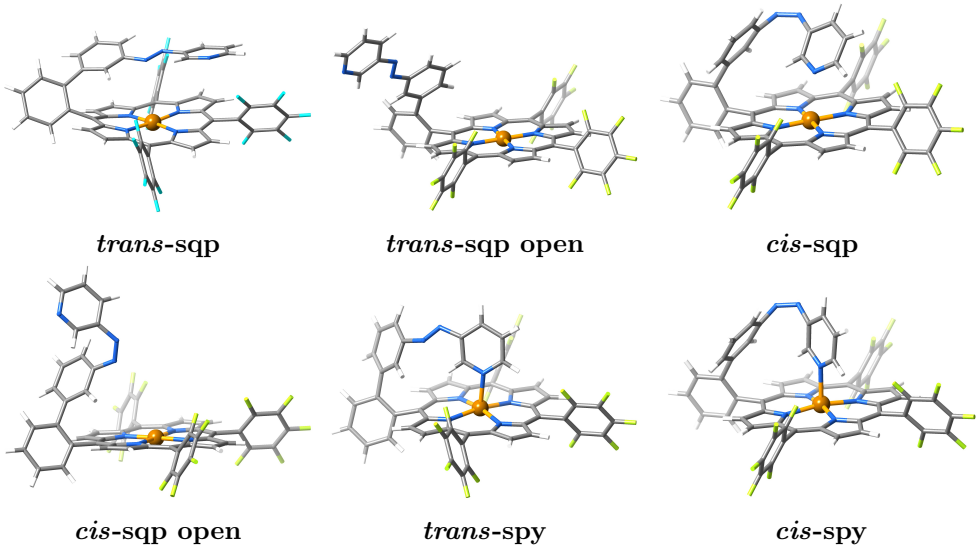

Figure 5.2. M06-2X geometries of the NiTPP-PAPy conformers listed in Table 5.1.

Geometry optimizations of *trans*-sqp and *cis*-spy with a larger basis set (TZVP on all atoms) and with the B97D functional (Grimme dispersion corrected) [17] give practically the same results; most distances and angles do not differ more than 0.1 Å and 5 degrees in both cases. The largest change is observed in the Ni-$N_{pyridine}$ distance in *trans*-sqp. The 4.36 Å predicted by the M06-2X functional changes to 4.21 Å with B97D. This 0.15 Å reduction reflects the relatively flat potential of the PAPy arm when it is not coordinated to the Ni atom.

The role of dispersion forces is particularly noticeable in the four-coordinated *trans*-sqp minimum, where the pyridine ring is found parallel to the porphyrin unit and the π-π interaction is important. The distance between Ni and the

N of the pyridine is shortened by 2.6 Å when the dispersion is included in the calculation. The influence of long-range interactions is also evident in the *cis*-sqp conformer, where the relatively short Ni-$N_{pyridine}$ distance suggests an incipient five-coordination, albeit with a singlet ground state. In this case the nitrogen lone pair is not conveniently oriented to Ni^{II}, since the angle between the pyridine and porphyrin planes is 79°. Hence, the gap between the $3d_{z^2}$ and $3d_{x^2-y^2}$ orbitals stays large and the singlet remains the ground state.

However, the most important consequence of including long-range interactions in the calculations of the present system is the strong stabilization of the *trans*-spy triplet. BP86 predicts a very high energy (0.96 eV) for this five-coordinated structure with respect to the four-coordinated *trans* conformers, while M06-2X predicts it to be 0.14 eV more stable than *trans*-sqp. Besides being close in energy, the square pyramid *cis* and *trans* isomers have also similar Ni-$N_{pyridine}$ distances, 2.16-2.17 Å, compatible with the experimentally estimated value of 2.1 Å. Recalling that the cis configuration of the product was assigned from Nuclear Overhauser experiments on a diamagnetic Zn analogue, we conclude that the *trans* structure cannot be excluded yet as a possible candidate of the five-coordinated paramagnetic product and that alternative mechanisms not involving azopyridine *trans-cis* isomerization as the key step of the SCO process should not be completely discarded.

Finally, we mention that the differences between the geometry optimizations in vacuum and those with solvent effects through the PCM model lead to virtually the same results. Neither the energies, nor the geometrical parameters show any significant changes when the complex is treated in a DMSO solvent. All the results reported below are obtained in a vacuum.

5.3 Axial coordination in *cis* and *trans* NiTPP-PAPy

The standard active space for an accurate determination of the relative stability of different spin states in (quasi-)octahedral TM-3d^n (n $\geq$ 5) complexes consists of (n + 4)-electrons and 12 orbitals [18]. In addition to the TM-3d orbitals and the extra set of d-orbitals to account for the double shell effect, one should also include the two ligand-σ orbitals of the e_g-like symmetry in the active space. However, in the present case this choice necessarily leads to an unbalanced description of the four- and five-coordinated species. The in-plane σ-orbital of the N_{porph} atoms is easily included in the active space for both species, but the second σ orbital corresponding to the axial ligand can only be included in the five-coordinated complexes. The corresponding orbital in the four-coordinated species is the lone pair orbital of the N atom on the pyridine ring, which in itself contributes very little to the electron correlation, and hence, does not stay in the active space.

Therefore we calculate the relative stability of the singlet and triplet state of the different NiTPP-PAPy species with a [10,11]-CASSCF wave function (see Fig. 5.3). The stability of the results was checked by comparing the singlet-triplet splitting of different five-coordinated species to the results obtained with the [12,12]-CASSCF calculations. The present results are also in good agreement with the [10,11]-CASSCF calculations for unsubstituted Ni porphyrin in Chapter 4.

CASSCF single point calculations are performed with the Molcas package [19, 20] using the DFT optimized structures of the most stable conformers: *trans*-sqp, *cis*-spy and *trans*-spy. The basis sets centred on the different atoms are of the atomic natural orbitals type [21–23]. Ni and N are described with a TZVP basis set, while C, F and H have a basis set of double-zeta quality.

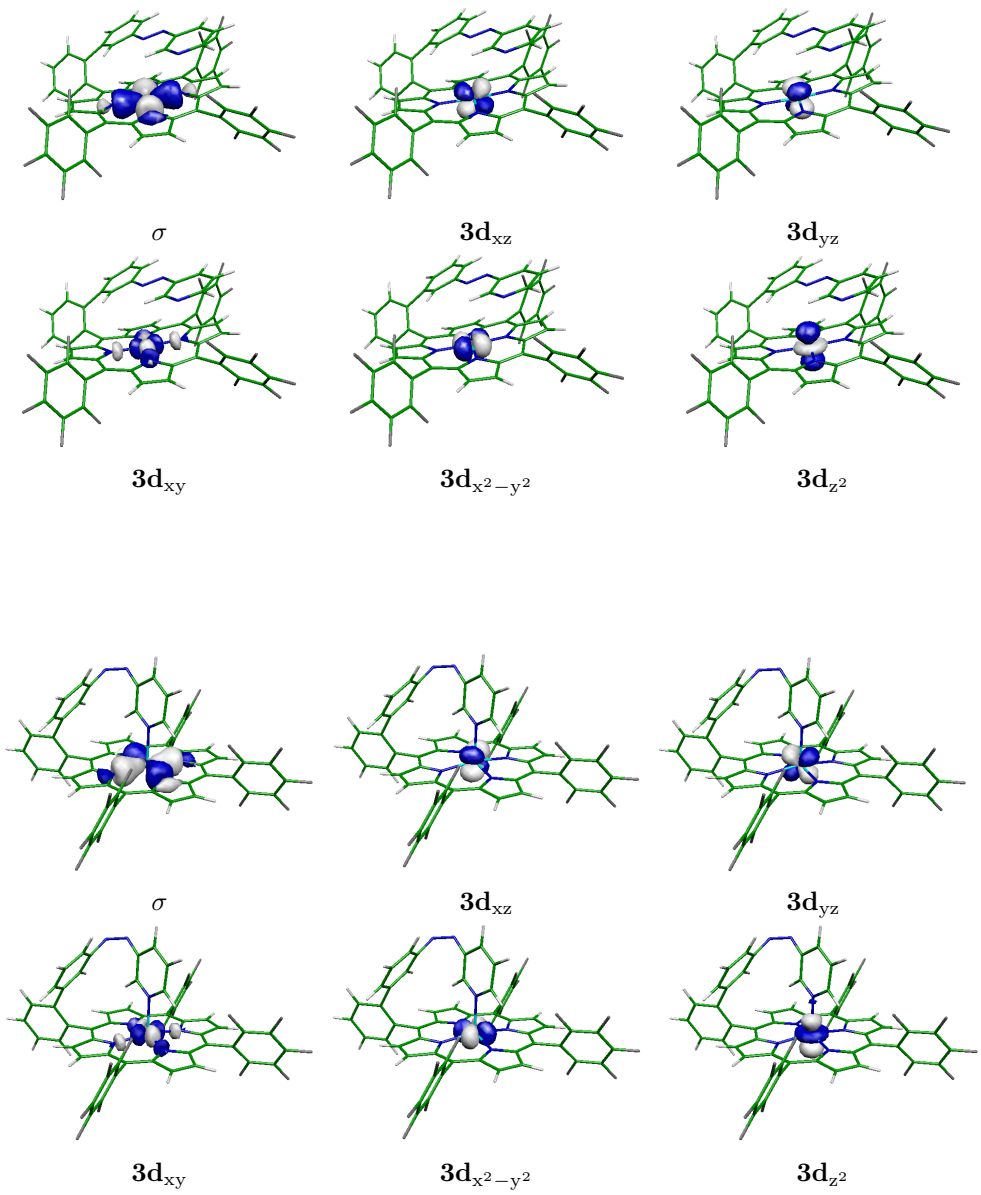

Figure 5.3. [10,11]-CASSCF active orbitals for the singlet *trans*-sqp (top) and the triplet *cis*-spy (bottom) NiTPP-PAPy species.

The relative energies listed in Table 5.2 indicate that both CASSCF and CASPT2 correctly predict a triplet ground state for the five-coordinated conformers. However, CASSCF fails to establish a singlet ground state for the four-coordinated sqp complex, which is repaired by including dynamic correlation through CAS-PT2. The results with the [12,12] active space are only slightly different to those obtained with the smaller active space. Interestingly enough, CASPT2 places the triplet of the *trans*-spy isomer energetically close to the initial singlet state of the square planar conformation, which does not discard the possibility of a SCO process without *trans-cis* isomerization.

Table 5.2. CASSCF and CASPT2 relative energies in eV of singlet and triplet states of *trans*-sqp, *cis*-spy and *trans*-spy.

		[10,11]		**[12,12]**
		CASSCF	**CASPT2**	**CASSCF**
trans-sqp	S=0	0.94	0.26	
	S=1	0.70	0.39	
cis-spy	S=0	1.34	1.07	1.39
	S=1	0.00	0.00	0.00
trans-spy	S=0	1.67	1.32	1.73
	S=1	0.36	0.29	0.36

To further settle the question about the mechanism, we have calculated triplet energies along the dissociation path of the PAPy from the Ni ion. This provides information about the thermal stability of the light-induced five-coordinated product in the *cis* and *trans* forms. The points along the scan were generated with M06-2X geometry optimizations fixing the Ni-N_{py} distances at different values. As shown in Fig. 5.4, the release of the pyridine group of the PAPy arm in the *trans*-spy form is nearly barrierless, while a steep rise in the energy is observed when the Ni-N distance is increased in the *cis*-spy isomer. The energy along this path reaches a maximum at d(Ni-N_{azo}) = 3.3 Å, where it is 0.84 eV higher than the triplet of the five-coordinated *cis* isomer. This means that a hypothetical triplet five-coordinated NiTPP-PAPy in *trans* form will release the axial ligand very rapidly at room temperature and that this process is slow for the *cis* form. Finally, we mention that the relative stability of the singlet *trans*-sqp and the triplet *cis*-spy states is opposite to what may be expected.

This can at least partially be ascribed to the limited basis set that we use in our calculation. It is well-known that larger basis sets (especially on the metal) are needed to obtain correct high-spin/low-spin energy differences in SCO processes [18, 24, 25]. However, such lowering of the singlet state(s) will not affect any of the arguments discussed above, and hence, the only plausible mechanism to explain the CISCO in this compound is via *trans-cis* isomerization. However, note that the 500 nm irradiation does not directly cause a $\pi_{azo} \rightarrow \pi^*_{azo}$ transition in PAPy and similar systems and the nature of the excitation causing the isomerization needs further clarification.

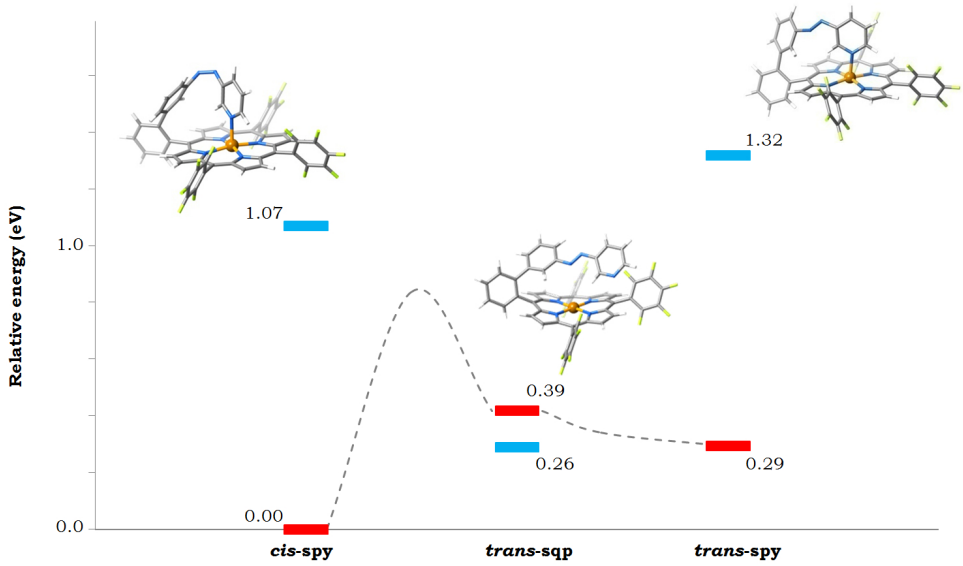

Figure 5.4. CASPT2 energies of the singlet (blue) and triplet (red) states of NiTPP-PAPy. The dashed lines connect the triplet state of the four-coordinated complex (middle) to the five-coordinated species *cis*-spy (left) and *trans*-spy (right).

5.4 Isomerization mechanism of the PAPy arm

In order to locate the $\pi_{azo} \rightarrow \pi^*_{azo}$ excitation in the absorption spectrum and to characterize the 500 nm band of the NiTPP-PAPy complex, we first calculated the vertical excitation spectrum of the PAPy arm. The minimal active space

to correctly study the vertical excitation spectrum of the PAPy arm should contain the π and π^* orbitals of the N=N bond and the lone pair orbitals (n_{azo}) of the nitrogen atoms, extended with two pairs of π and π^* orbitals of the phenyl and pyridine side groups (π_{side} and π^*_{side}), and the lone pair orbital of the pyridine nitrogen. This active space with 12 electrons and 9 orbitals (see Fig. 5.5) was used to generate the reference wave function for the subsequent CASPT2 calculations.

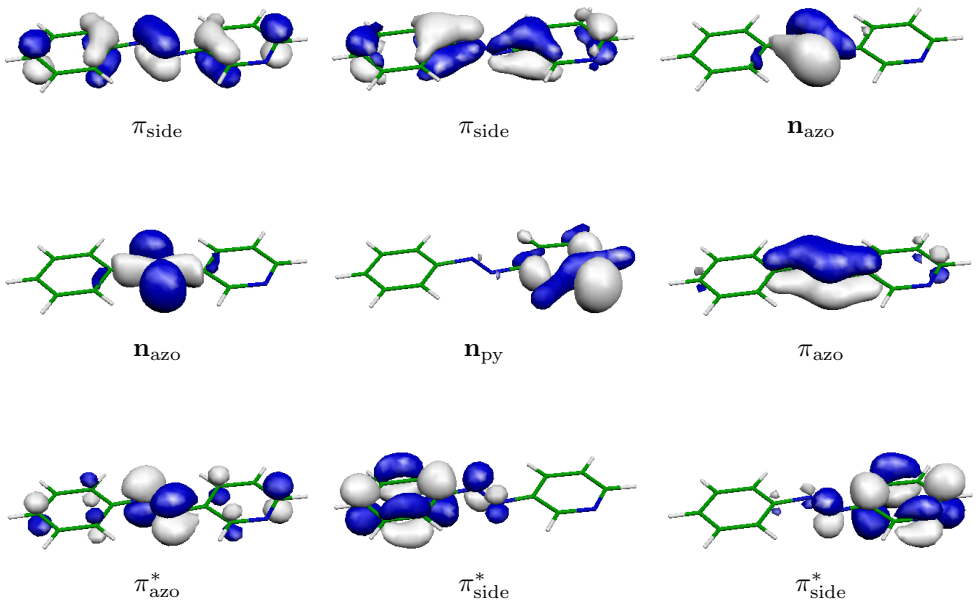

Figure 5.5. Active space for the [12,9]- CASPT2 calculation of the absorption spectrum of the PAPy arm.

The results of these calculations are summarized in Table 5.3 and compared to experimental data [26]. The effect of electron correlation on the excitation energies is large, especially for the $\pi_{side} \rightarrow \pi^*_{azo}$ transitions. The very high CASSCF energy of these states ($\sim$ 6 eV) is lowered by approximately 2.5 eV by the CASPT2 treatment of the electron correlation. The CASPT2 transition energies are in good agreement with the experimental values for all states. The most important features of the excitation spectrum are a low-lying $n_{azo} \rightarrow \pi^*_{azo}$ excitation around 2.75 eV (450 nm) and a high intensity $\pi_{side} \rightarrow \pi^*_{azo}$ transition

appearing at 3.48 eV (356 nm). The lowest CASSCF root that involves π_{azo} and π^*_{azo} orbitals is located at an energy of 7.41 eV and CASPT2 lowers the transition energy to 6.99 eV (177 nm), much higher in energy than the reported 500 nm wavelength to induce SCO in NiTPP-PAPy.

Table 5.3. [9,12]-CASPT2 vertical excitation energies in eV of *trans* 3-phenylazopyridine (3-PAPy). Experimental values [26] are given for comparison.

***trans* 3-PAPy**	**CASSCF**	**CASPT2**	**Oscillator strength**	**Exp.**
$n_{azo} \rightarrow \pi^*_{azo}$	3.15	2.75 (450 nm)	$6.22{\cdot}10^{-8}$	2.76
$\pi_{side} \rightarrow \pi^*_{azo}$	5.96	3.48 (356 nm)	0.32	3.91
$\pi_{azo} \rightarrow \pi^*_{azo}$	7.41	6.99 (177 nm)	0.28	

Although several experimental and theoretical studies have been published [27–33], the isomerization mechanism of azobenzene and its derivatives is still a controversial issue. Two possible paths have been proposed (see Fig. 5.6) based on the fact that the quantum yield for the isomerization shows a dependence on the wave length [34].

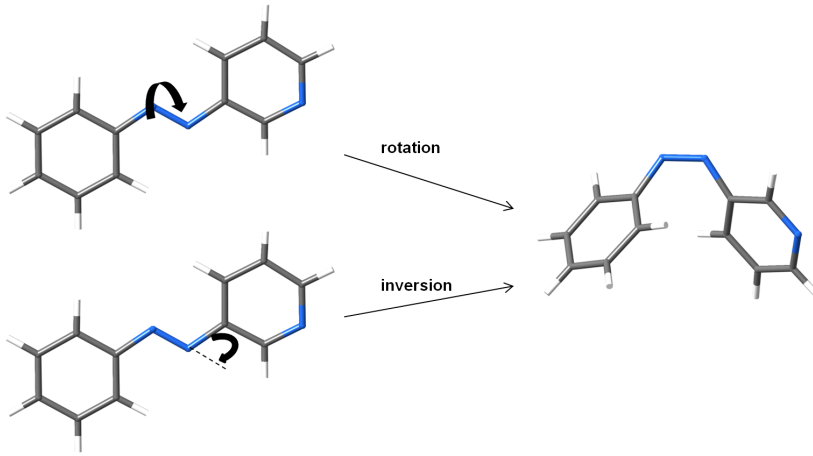

Figure 5.6. Two possible mechanisms for the *trans-cis* isomerization of PAPy and derivatives.

On one hand, the rotation mechanism implies a 180° twist of the C-N=N-C dihedral angle and traditionally has been proposed to happen when the system

is excited to the $\pi_{side}\pi^*_{azo}$ state. On the other hand, the inversion mechanism consists in an inversion of the C-N=N angle and is attributed to the $n_{azo}\pi^*_{azo}$ state. The products of these two paths are indistinguishable for unsubstituted azobenzene complicating the understanding of the isomerization mechanism.

The substitution of one phenyl moiety by a pyridine ring gives rise to a new possible excited state characterized by the excitation of one electron from the lone pair of N_{py} (n_{py}) to the π^*_{azo} antibonding orbital. In order to understand the isomerization of PAPy, the role of this state as well as the differences between PAPy and azobenzene need to be reviewed. To this purpose, scans along the rotation dihedral and the inversion angle have been performed. For each point the scanned coordinate has been frozen and the rest of the molecule has been relaxed with DFT. The energy of the obtained geometries has been estimated with [12,9]-CASPT2 single point calculations with the active space previously described. Since previous theoretical studies on azobenze [35, 36] reported B3LYP [37] and 6-31G* [38] to perform properly for these systems, these functional and basis set will be used in this part of the chapter to generate the geometries.

Figure 5.7 summarizes the inversion mechanism scan. In the [12,9]-CASPT2 single point calculation the energy of the first five singlet states has been estimated in each point of the scan. The ground state (black line) corresponds to the closed-shell singlet and the first three excited states are characterized by the promotion of one electron to the π^*_{azo} orbital. This electron is excited from a n_{azo} orbital in S_1 (red line), from a n_{py} orbital in S_2 (green line) and from a π_{side} orbital in S_3 (purple line). S_4 (blue line) corresponds to a double excitation from n_{azo} to π^*_{azo} orbitals.

From the very-left part of the scan the absorption spectrum of the *trans* minimum can be extracted. According to the results exposed in Table 5.3, the bright band corresponds to a 3.66 eV (339 nm) $\pi_{side} \rightarrow \pi^*_{azo}$ symmetry allowed excitation with an oscillator strength of 0.37. The $n_{azo} \rightarrow \pi^*_{azo}$ band appears at 2.79 eV (444 nm) but with a very small oscillator strength, $1.85{\cdot}10^{-7}$. The energy of all states increases along the inversion of the C-N=N angle except for the S_1 in which it remains practically constant. The unique plausible path

for this mechanism is through S_1 but this implies internal conversion from S_1 to the ground state at some point. Taking into account that the minimal energy gap between S_1 and the ground state is of 1.21 eV at C-N=N angle of 153° this mechanism will be highly inefficient. The role of the $n_{py}\pi^*_{azo}$ state in the inversion mechanism is negligible but in the *trans* minimum this state is accessible *via* the bright excitation and hence it must be taken into account to understand the photochemistry of the system.

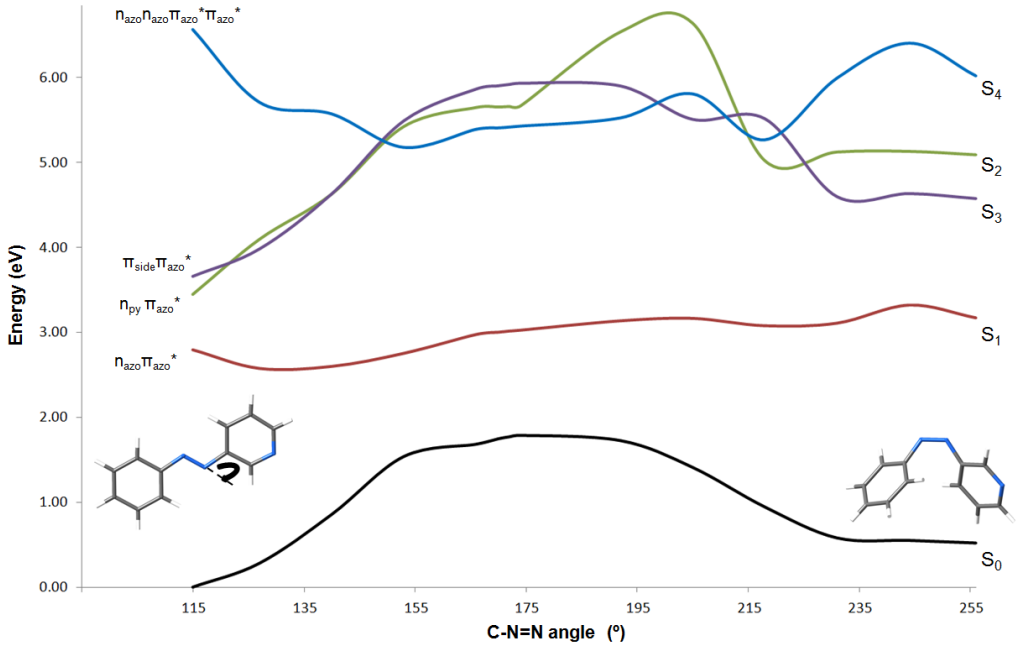

Figure 5.7. [12,9]-CASPT2/B3LYP scan over the C-N=N coordinate to reproduce the inversion mechanism for the isomerization of PAPy.

The situation is different in the rotation mechanism (see Fig. 5.8). The very-left part of the scan is exactly the same as in the inversion one since the starting point is the same *trans* minimum. In a similar way as in the inversion mechanism the energy of S_1 is practically constant along the rotation of the C-N=N-C dihedral. However, in this case the minimal energy gap between S_1 and the ground state is 0.44 eV at 90° and with this lower energy difference the internal conversion is more efficient. Therefore, the 2.79 eV excitation activates the rotation mechanism through S_1. A rotation path from the bright S_3 is also

possible since it presents a conical intersection with S_4 at 135°. After crossing to S_4 the system decays to the S_1 and ground states at 90°. This route, initiated by a 3.66 eV excitation to S_3, presents lower quantum yields since it implies a conical intersection which irradiating at 444 nm is avoided.

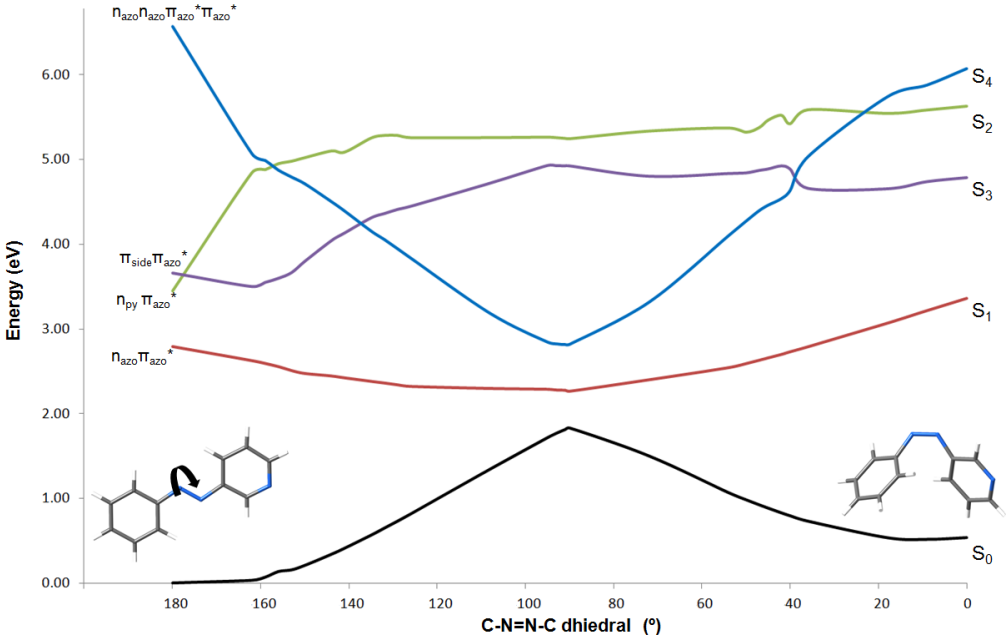

Figure 5.8. [12,9]-CASPT2/B3LYP scan over the C-N=N-C coordinate to reproduce the rotation mechanism for the isomerization of PAPy.

Although the excitation used to induce the SCO in the NiTPP-PAPy complex is lower than the required to isomerise azopyridine molecules, calculations in present section reveal that different paths can lead to this process. In this sense, excitations to π^*_{azo} weaken the N=N bond favouring its rotation.

5.5 Vertical excitation energies of NiTPP-PAPy

An important question that remains to be answered is the nature of the 500 nm excitation used to induce the SCO in the NiTPP-PAPy complex. The CASPT2 results of the PAPy subsystem place the $\pi \rightarrow \pi^*$ excitation at higher energies,

in agreement with the findings in other azobenzene derivatives, but the interaction of the PAPy arm with the porphyrin system may shift the $\pi \rightarrow \pi^*$ transition to lower energies as suggested by Venkataramani [1]. Hence, to obtain a complete description of the optical transitions of the NiTPP-PAPy system, the π system of the porphyrin ring should also be considered. Our results in Chapter 4 indicate that a [16,14] active space is required to precisely describe the optical absorption of porphyrin systems. This active space is large and its expansion with orbitals of the PAPy arm is unfeasible. However, the aim of this chapter is not to describe the absorption spectrum of the porphyrin but to estimate the PAPy-porphyrin interaction and for this purpose the original four-orbital model of Gouterman [39–41] is enough to get a qualitative picture. Adding these four orbitals (π_{porph}) to the lone pair orbitals (n_{azo}), π_{azo} and π^*_{azo} of the PAPy arm gives a [10,8]-CASSCF wave function (see Fig. 5.9). This active space does not describe any excited state involving the electrons in the Ni-3d orbitals, but the metal-centred excitations have a low oscillator strength and the charge transfer excitations appear at higher energy. Whereas the inclusion of the Ni-3d and 3d' orbitals is essential to obtain accurate estimates of the relative stability of the different species, this is rather unimportant for the vertical spin allowed excitations from the closed shell ground state.

Table 5.4 lists the lowest calculated transition energies and the corresponding oscillator strengths. The states are labelled according to the most important electron replacements involved in the excitation. The lowest two transitions have intermediate oscillator strength and can be associated to the Q bands observed at around 523 nm in the experimental work. The π orbitals involved in these transitions are well localized on the porphyrin ring, but as is shown in Fig. 5.10 the π^* orbitals have a non-negligible contribution from the antibonding combination of the N-2p orbitals of the azo bond of the PAPy arm. Hence, the Q band is not simply a porphyrin centred excitation but also causes a certain degree of occupation of the π^*_{azo} orbital. This weakens the N=N bond and could very well trigger a *trans-cis* isomerization. It is interesting to compare these orbitals with those of the *trans*-sqp optimized geometry obtained with the BP86 functional. The PAPy arm is more separated from the porphyrin ring in this geometry and the orbitals are either pure π^*_{porph} or π^*_{azo}, without any mixing. This suggest a determinant role of the $\pi - \pi$ interactions in this SCO

mechanism, revealed by the M06-2X functional. The important shortening of the porphyrin-pyridine distance (Table 5.1) induces the delocalization and the subsequent possibility of populating the π^* orbital at lower energy.

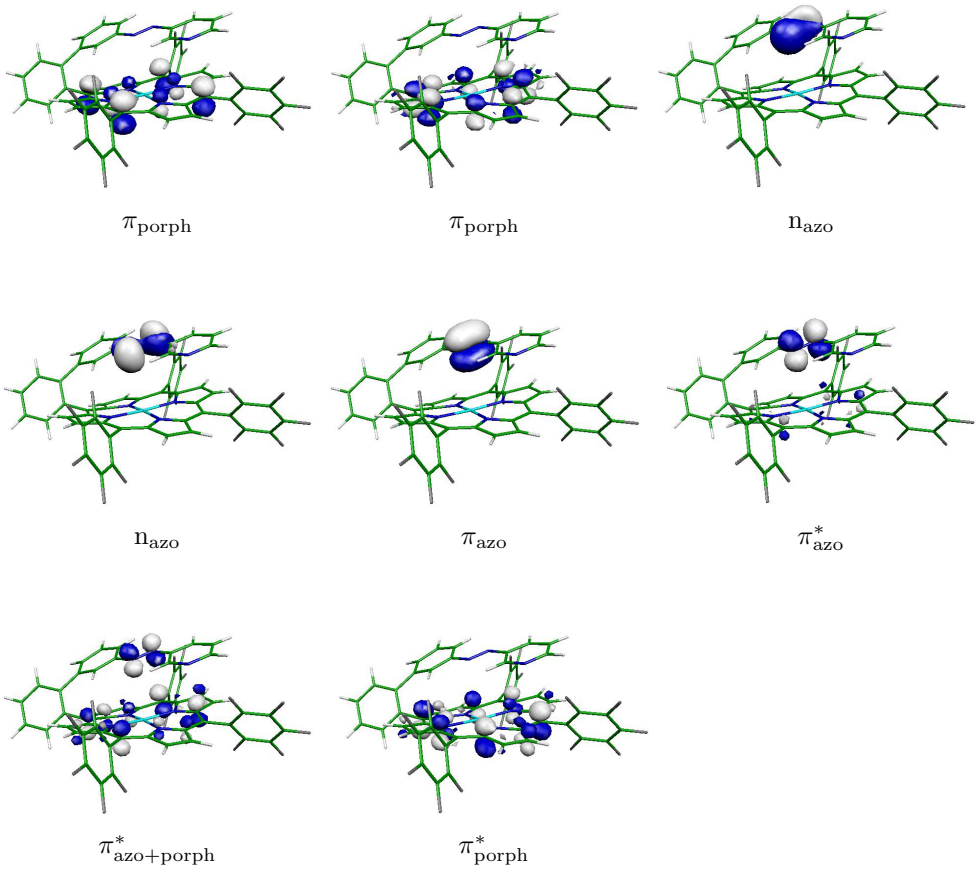

Figure 5.9. Active space for the [10,8]- CASPT2 calculation of the vertical excitation energies of NiTPP-PAPy.

Table 5.4. [10,8]-CASPT2 vertical excitation energies in eV of *trans*-sqp NiTPP-PAPy. Experimental values are given for comparison [1].

***trans* NiTPP-PAPy**	**CASSCF**	**CASPT2**	**Oscillator strength**	**Exp.**
$\pi_{porph} \rightarrow \pi^*_{azo+porph}$	3.55	2.59 (478 nm)	$3.70{\cdot}10^{-2}$	523
$\pi_{porph} \rightarrow \pi^*_{azo+porph}$	3.57	2.65 (467 nm)	$5.60{\cdot}10^{-2}$	523
$n_{azo} \rightarrow \pi^*_{azo}$	3.60	3.23 (383 nm)	$9.00{\cdot}10^{-6}$	406
$n_{azo} \rightarrow \pi^*_{azo}$ / $\pi_{porph} \rightarrow \pi^*_{azo}$	5.29	4.57 (271 nm)	$5.90{\cdot}10^{-4}$	322

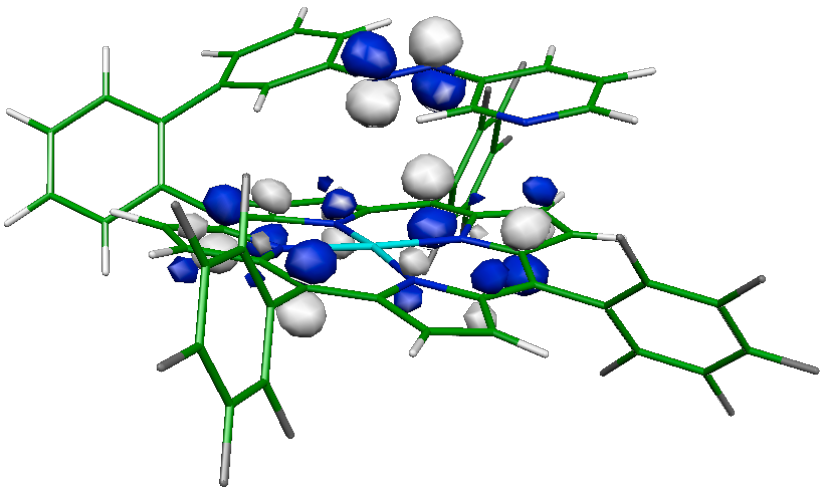

Figure 5.10. Graphical representation of the orbital that becomes occupied in the lowest two vertical excitations of NiTPP-PAPy.

Severe intruder state problems hinder the accurate description of the $\pi_{azo} \rightarrow \pi^*_{azo}$ excitation in the large complex. However, the similarity of the SA-CASSCF excitation energy (7.25 eV) with the one obtained for the PAPy arm (see Sec. 5.4) situates the $\pi_{azo} \rightarrow \pi^*_{azo}$ excitation in NiTPP-PAPy at significant higher energy than 2.5 eV (500 nm) used in the experiments to induce the SCO.

While the Q band is well reproduced by our calculations, the experimental absorption spectrum of NiTPP-PAPy shows a Soret band of high intensity at 406 nm. At this region a $n_{azo} \rightarrow \pi^*_{azo}$ excitation is found, but the low oscillator strength cannot explain the experimentally observed intense peak. Probably, this low intensity band is hidden by the optically allowed $\pi_{porph} \rightarrow \pi^*_{porph}$ excitations of the porphyrin moiety which cannot be reproduced with the present [10,8]-CAS [42]. In Chapter 4 we have estimated this Ni porphyrin excitations by means of [16,14]-CASPT2 calculations. In these calculations, the most intense $\pi_{porph} \rightarrow \pi^*_{porph}$ band appears at 335 nm. The deviation with respect to the experimental Soret band of the NiTPP-PAPy (406 nm) can be attributed to the geometrical differences between the whole system and the Ni porphyrin model. Furthermore, the calculated oscillator strength for this excitation is 1.18, showing that this band is of high intensity compared to the

bands obtained in Table 5.4. One can conclude that for the NiTPP-PAPy spectrum, the Q band corresponds to $\pi_{\text{porph}} \rightarrow \pi^*_{\text{azo+porph}}$ and the Soret band to $\pi_{\text{porph}} \rightarrow \pi^*_{\text{porph}}$ excitations which are not relevant for the SCO mechanism.

5.6 Conclusions

Although the original proposal of a *trans-cis* isomerization of the N=N double bond induced by a $\pi \rightarrow \pi^*$ excitation offers a plausible explanation for reversible room-temperature spin crossover observed in NiTPP-PAPy, the large red-shift of 150 nm of the excitation energy leaves some room for improvement. SCO in standard Ni-porphyrins is induced by a $\pi - \pi^*$ excitation of 2.5 eV (500 nm) on the porphyrin ring. The same wave length was used in the experiments on NiTPP-PAPy and therefore we first investigated the possibility of SCO induced by a $\pi - \pi^*$ excitation on the porphyrin ring without the need for *trans-cis* isomerization. The inclusion of the effect of dispersion forces in the geometry optimization using the M06-2X functional leads to *cis* and *trans* isomers with four- and five-coordinated Ni ions in a relatively small energy window. Single point CASPT2 calculations on the optimized geometries predict a near degeneracy for the low-spin state of the four-coordinated complex and the high-spin state of the five-coordinated complex with the PAPy arm in *trans* conformation. However, the absence of a barrier along the dissociation path of the PAPy arm in a hypothetical all-*trans* mechanism is incompatible with the experimental stability of the high-spin state. In contrast, a significant barrier was found for the dissociation of the PAPy-arm in the *cis* conformation.

Subsequently, we used CASSCF/CASPT2 calculations to clarify the character of the excitation that induces the *trans-cis* isomerization at 500 nm. The $\pi - \pi^*$ excitation on the azo group was found at very high energy and the excitation from the π orbitals of the six-membered rings bonded to the N=N group into the N=N π^* orbital occurs at 350 nm, also too high to be assigned to the experimental excitation. The CASPT2 results identify the 500 nm transition as an excitation involving a bonding π orbital of the porphyrin ring and an antibonding π^* orbital with important contributions from both the porphyrin

system and the N=N group. The occupation of this anti-bonding orbital of mixed character weakens the N=N bond and leads to a *trans-cis* isomerization.

Hence, the combination of DFT and multiconfigurational wave function calculations is able to firmly establish the *trans-cis* isomerism in the PAPy arm as a mechanism for the spin crossover in NiTPP-PAPy. The structures obtained with DFT/M06-2X show that the arm is closer to the porphyrin ring than in the structure without taking into account the dispersion. The character of the excitation that triggers the spin crossover is identified and involves the electron replacement from a bonding π orbital on the porphyrin to an antibonding orbital with contributions on the porphyrin and the azo group.

5.7 References

[1] S. Venkataramani, U. Jana, M. Dommaschk, F. D. Sönnichsen, F. Tuczek, and R. Herges, Science **331**, 445 (2011).

[2] S. Thies, H. Sell, C. Schütt, C. Bornholdt, C. Näther, F. Tuczek, and R. Herges, J. Am. Chem. Soc. **133**, 16243 (2011).

[3] D. Kim, C. Kirmaier, and D. Holten, Chem. Phys. **75**, 305 (1983).

[4] D. Kim and D. Holten, Chem. Phys. Lett. **98**, 584 (1983).

[5] J. Rodriguez and D. Holten, J. Chem. Phys. **92**, 5944 (1990).

[6] L. Chen, X. Zhang, E. Wasinger, K. Attenkofer, G. Jennings, A. Muresan, and J. Lindsey, J. Am. Chem. Soc. **129**, 9616 (2007).

[7] J. P. Perdew, K. Burke, and M. Ernzerhof, Phys. Rev. Lett. **78**, 1396 (1997).

[8] J. P. Perdew, K. Burke, and M. Ernzerhof, Phys. Rev. Lett. **77**, 3865 (1996).

[9] A. D. Becke, Phys. Rev. A **38**, 3098 (1988).

[10] J. P. Perdew, Phys. Rev. B **33**, 8822 (1986).

[11] Y. Zhao and D. G. Truhlar, Theor. Chem. Acc. **120**, 215 (2008).

[12] M. J. Frisch, G. W. Trucks, H. B. Schlegel, G. E. Scuseria, M. A. Robb, J. R. Cheeseman, G. Scalmani, V. Barone, B. Mennucci, G. A. Petersson, et al., Gaussian09, gaussian Inc. Wallingford CT 2009.

[13] N. Godbout, D. R. Salahub, J. Andzelm, and E. Wimmer, Can. J. Chem. **70**, 560 (1992).

[14] T. H. Dunning and P. J. Hay, in Methods of Electronic Structure Theory, edited by H. F. Schaefer III (Plenum, New York, 1977), vol. 3, p. 1.

[15] J. Tomasi, B. Mennucci, and R. Cammi, Chem. Rev. **105**, 2999 (2005).

[16] A. Klamt and G. Schüürmann, J. Chem. Soc., Perkin Trans. 2 p. 799 (1993).

[17] S. Grimme, J. Comput. Chem. **27**, 1787 (2006).

[18] K. Pierloot and S. Vancoillie, J. Chem. Phys. **125**, 124303 (2006).

[19] G. Karlström, R. Lindh, P.-Å. Malmqvist, B. O. Roos, U. Ryde, V. Veryazov, P.-O. Widmark, M. Cossi, B. Schimmelpfennig, P. Neogrady, et al., Comput. Mater. Sci. **28**, 222 (2003).

[20] F. Aquilante, L. De Vico, N. Ferré, G. Ghigo, P.-Å. Malmqvist, P. Neogrady, T. B. Pedersen, M. Pitoňák, M. Reiher, B. O. Roos, et al., J. Comput. Chem. **31**, 224 (2010).

[21] P.-O. Widmark, M. P.-Å., and B. O. Roos, Theor. Chim. Acta **77**, 291 (1990).

[22] B. O. Roos, R. Lindh, P.-Å. Malmqvist, V. Veryazov, and P.-O. Widmark, J. Phys. Chem. A **108**, 2851 (2004).

[23] B. O. Roos, R. Lindh, P.-A. Malmqvist, V. Veryazov, and P.-O. Widmark, J. Phys. Chem. A **109**, 6575 (2005).

[24] M. Kepenekian, V. Robert, B. Le Guennic, and C. De Graaf, J. Comput. Chem. **30**, 2327 (2009).

[25] B. Ordejon, C. de Graaf, and C. Sousa, J. Am. Chem. Soc. **130**, 13961 (2008).

[26] E. V. Brown and G. R. Granneman, J. Am. Chem. Soc. **97**, 621 (1975).

[27] P. Birnbaum, J. Linford, and D. Style, Trans. Faraday Soc. **49**, 735 (1953).

[28] R. Dyck and D. McClure, J. Chem. Phys. **36**, 2326 (1962).

[29] I. Lednev, T. Ye, P. Matousek, M. Towrie, P. Foggi, F. Neuwahl, S. Umapathy, R. Hester, and J. Moore, Chem. Phys. Lett. **290**, 68 (1998).

[30] T. Fujino, S. Arzhantsev, and T. Tahara, J. Phys. Chem. A **105**, 8123 (2001).

[31] L. Briquet, D. Vercauteren, E. Perpete, and D. Jacquemin, Chem. Phys. Lett. **417**, 190 (2006).

[32] G. Tiberio, L. Muccioli, R. Berardi, and C. Zannoni, ChemPhysChem **11**, 1018 (2010).

[33] O. Weingart, Z. Lan, A. Koslowski, and W. Thiel, J. Phys. Chem. Lett. **2**, 1506 (2011).

[34] H. Rau and E. Luddecke, J. Am. Chem. Soc. **104**, 1616 (1982).

[35] P. Cattaneo and M. Persico, Phys. Chem. Chem. Phys. **1**, 4739 (1999).

References

[36] L. Gagliardi, G. Orlandi, F. Bernardi, A. Cembran, and M. Garavelli, Phys. Chem. Chem. Phys. **111**, 363 (2004).

[37] A. D. Becke, J. Chem. Phys. **98**, 5648 (1993).

[38] M. Francl, W. Pietro, W. Hehre, J. Binkley, M. Gordon, D. Defrees, and J. Pople, J. Chem. Phys. **77**, 3654 (1982).

[39] M. Gouterman, J. Chem. Phys. **30**, 1139 (1959).

[40] M. Gouterman, G. H. Wagnière, and L. C. Snyder, J. Mol. Spectrosc. **11**, 108 (1963).

[41] C. Weiss, H. Kobayashi, and M. Gouterman, J. Mol. Spectrosc. **16**, 415 (1965).

[42] L. Serrano-Andrés, M. Merchán, M. Rubio, and B. O. Roos, Chem. Phys. Lett. **295**, 195 (1998).

Coordination-induced spin-crossover in a Ni porphyrin complex

Chapter 6

Spin and oxidation state of Mn corrole and corrolazine complexes

6.1 Introduction

The planar structure of transition metal (TM) porphyrins and their derivatives favours binding of axial ligands to the metal centre and is a key factor in many biological processes. Biomimetic TM porphyrins have been developed as synthetic catalysts [1–8], in which the energetics of the low-lying spin states as well as the factors stabilizing these states deserve special attention. In many cases, the axial ligand directly affects the magnetic properties and the reactivity of these compounds. For instance, in Mn porphyrin complexes reduction of the low-spin (S=0) Mn^{V} complex with a closed-shell d^2 electronic configuration (Fig. 6.1, centre right) to a d^3 Mn^{IV} complex implies not only the addition of one electron but also the promotion of an electron from $3d_{xy}$ to $3d_{xz}$ or $3d_{yz}$ and the consequent change to a high-spin (S=3/2) configuration (Fig. 6.1 centre left) [9–11]. Changes in the axial ligand can stabilize the Mn^{V} $3d_{xz,yz}$ orbitals, favouring the high-spin (S=1) state (Fig. 6.1 right) and facilitating the reduction to Mn^{IV}.

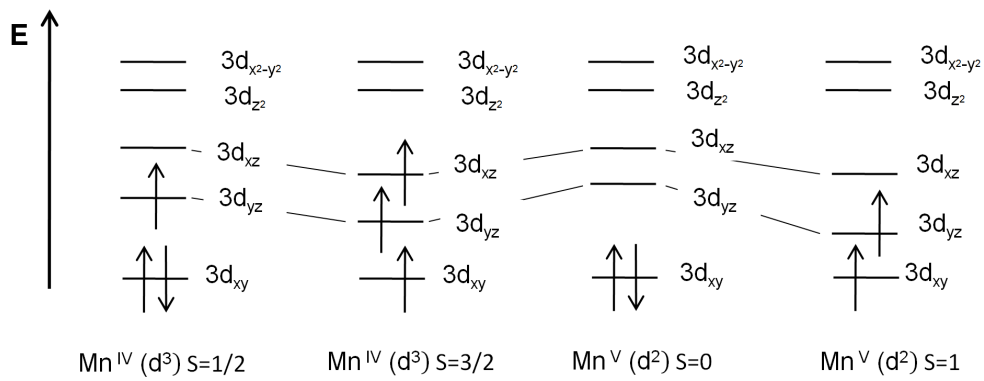

Figure 6.1. Low- (S=1/2) and high-spin (S=3/2) Mn^{IV} (left) and low- (S=0) and high-spin (S=1) Mn^{V} (right) spin configurations of the Mn ion in the quasi-square pyramid coordination sphere of the oxo-Mn(porphyrin) system with the nitrogens of the pyrrole rings placed on the x- and y-axes.

This example shows how porphyrin stabilizes transition metal ions with unusually high oxidation states [12], but corrole (Cor), one *meso* carbon atom shorter, has been postulated to be even more effective for this purpose. The most important difference in the corrole structural skeleton with respect to porphyrin (Fig.6.2) is that while the latter coordinates to the metal as a dianionic ligand, the former is trianionic [13]. Although corrole was first reported in 1964 [14], the interest in this macrocycle has increased since 1999, when simpler synthetic pathways were developed [15–17], emphasizing the large application range of corrole and its TM complexes [18, 19]. This interest has resulted in several experimental and theoretical studies on corrole X-ray structure, spectroscopy and electronic structure [20–25].

The formal oxidation states of TMs in corrole are higher than in porphyrin, but the metal center in a [TM(Cor)] is not necessarily high-valent, and sometimes corrole is expected to act as a dianionic radical instead of a closed-shell trianion. It has been suggested that low oxidation states can be stabilized by the coupling with noninnocent corrole ligands in some copper and iron complexes [25–27]. However, the electronic structure of the triplet state in Mn^{V} corroles is attributed to a high spin (S=1) Mn^{V} (Fig. 6.1 right) with an innocent, closed-shell trianionic corrole, due to the high energy of the low spin (S=1/2)

Mn^{IV} (Fig. 6.1 left) ferromagnetically coupled to a one-electron radical dianionic corrole acting as a noninnocent ligand [22]. Once again, the nature of the axial ligand is a crucial factor in this noninnocent behaviour. The capability of corrole to stabilize unusual oxidation states of TM has often been attributed both to its 3- charge and to its strong σ-donor ligand-field. The cavity size of the more recent corrolazine (Cz) derivative, first synthesized in 2001 [28], is smaller than in corrole, which enhances the σ-donation. In addition, the *meso*-substituted nitrogen atoms (Fig.6.2) are more electronegative than carbon and contribute to the electron deficiency of the coordination sphere, favouring the 3- charge of the ligand over the dianionic radical state [29, 30].

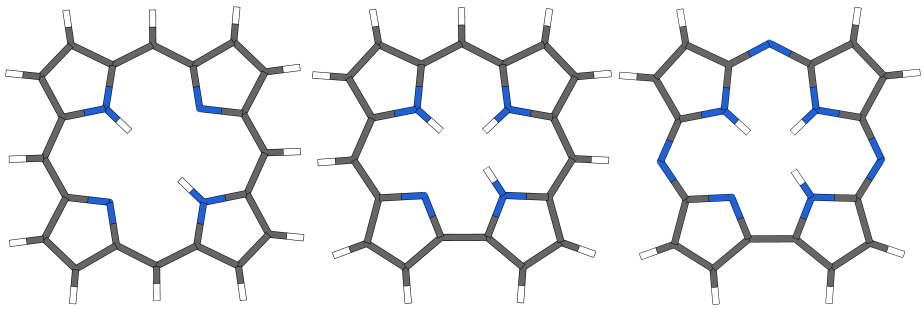

Figure 6.2. Porphyrin, the one *meso* carbon atom shorter derivative corrole, and its nitrogen *meso*-substituted derivative, corrolazine.

As seen above, small structural variations in the axial ligand and the macrocycle result in important changes in the spin and oxidation state of the metal centre, which directly affects the reactivity of the complex [31]. In order to catalyze oxygen transfer reactions, [Mn(Cor)(O)] [32–35] and [Mn(Cz)(O)] [36–38] have been synthesized. Similarly to their oxo derivatives, imido- (NR) manganese corrole and corrolazine have attracted interest due to their potential applications, but not much is known about their properties. [Mn(tpfc)(NMes)] (tpfc = tris(pentafluorophenyl)corrole, NMes = *N*-mesityl), [Mn(tpfc)(NtClPh)] (NtClPh = 2,4,6-trichlorophenyl) [39, 40], [Mn(tbpcz)(NMes)] (tbpcz = octakis(*p*-*tert*-butylphenyl)corrolazine) [41] and [Mn(tpfc)(NTs)] (NTs = *N*-tosyl) [42] are the few examples reported. NMes, NtClPh and NTs (Fig.6.3) axially coordinate to the metal as dianionic ligands with distances typically assigned to a

M≡N bond, giving rise to neutral complexes with formally high-valent Mn^{V}. Interestingly, while complexes with NMes and NtClPh are characterized as diamagnetic (S=0) by ^{1}H and ^{19}F NMR spectroscopy, magnetic measurements on the NTs derivative give a magnetic moment associated with a paramagnetic (S=1) state on the Mn^{V} [43]. No low-lying Mn^{IV} states with a radical on corrole or corrolazine are expected since they are high-lying in the oxo derivatives [22]. The present chapter describes a comprehensive DFT and CASPT2 computational study on imido-Mn corrole and corrolazine complexes. It focuses on the geometrical parameters, the lowest Mn (S=0) and (S=1) spin states, and the role of the three main actors (metal, macrocycle and imide) on the spin and oxidation states of [Mn(Cor)(NMes)], [Mn(Cz)(NMes)], [Mn(Cor)(NtClPh)] and [Mn(Cor)(NTs)].

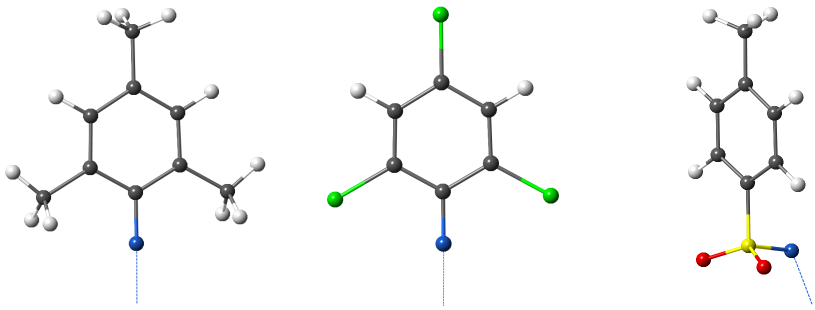

Figure 6.3. Axial imide ligands N-mesityl (NMes), N-(2,4,6-trichlorophenyl) (NtClPh) and N-tosyl (NTs).

6.2 DFT geometry optimizations

DFT geometry optimizations have been carried out for both singlet and triplet states of the four imido-complexes using def2-TZVP basis set [44, 45]. First of all, PBE0 [46–48] and BP86 [49, 50] functionals have been compared on Mn(Cor)(NMes). The triplet state in the PBE0 calculation shows a considerable spin contamination ($<\hat{S}^2> = 3.74$) resulting in a severe overestimation of the Mn-L_{axial} bond distance. On the other hand, DFT calculations with the

BP86 functional do not show such anomalous spin contamination ($<\hat{S}^2> = 2.14$) and the optimized M-L_{axial} bond distance is 1.70 Å, much shorter than the 2.03 Å PBE0 bond length. Since the axial coordination distance is expected to play a crucial role in the relative stability of the spin-states, the BP86 functional has been chosen to perform DFT geometry optimizations. To start, we have explored all possible orientations of the axial ligand for the NTs complex (see Fig. 6.4).

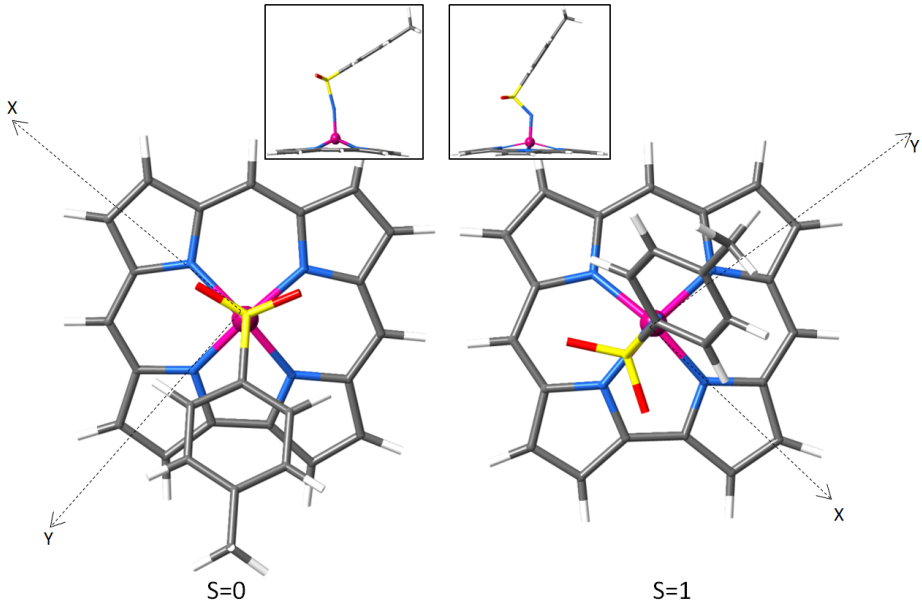

Figure 6.4. Top view of the most stable DFT conformations, with the R moiety between $N_{pyrrole}$ (alternated) for the singlet and with the R moiety aligned with $N_{pyrrole}$ (eclipsed) for the triplet. The insets give a side view of the structures.

Rotating the complex around the Mn-N_{axial} axis in intervals of 45°, four alternated and eclipsed conformations have been optimized with BP86/TZVP. Eclipsed conformations have the R moiety of the axial ligand aligned with $N_{pyrrole}$. The resulting steric repulsion lengthens the Mn–N_{axial} bond distance and closes the Mn–N_{axial}–S angle preferred by the triplet state. In contrast this repulsion is avoided in alternated conformations favouring singlet states with short axial distances and linear coordination angles. The most important struc-

tural parameters and the relative energies of the BP86/def2-TZVP geometry optimization are summarized in Table 6.1.

Table 6.1. Relevant BP86/def2-TZVP optimized geometrical parameters for the four imido-complexes. Distances and out of $N_{pyrrole}$ plane displacement ($\triangle$) in Å, angles in degrees and relative energies in eV. Experimental values are given in parenthesis [39, 41, 42].

	Mn-$N_{pyrrole}$	Mn-N_{axial}	Mn-N_{axial}-R	$\triangle$	relative energy
Mn(Cor)(NMes)					
S=0	1.92 - 1.95	1.61	179.2	0.54	0.00
	(1.89 - 1.95)	(1.61)	(170.4)	(0.51)	
S=1	1.93 - 1.95	1.70	145.9		0.67
Mn(Cz)(NMes)					
S=0	1.89 - 1.91	1.61	178.6	0.59	0.00
	(1.87 - 1.91)	(1.61)	(176.9)	(0.55)	
S=1	1.90 - 1.93	1.69	145.5		0.64
Mn(Cor)(NtClPh)					
S=0	1.91 - 1.95	1.62	179.1	0.55	0.00
S=1	1.92 - 1.95	1.70	144.1		0.52
Mn(Cor)(NTs)					
S=0	1.92 - 1.94	1.62	167.0	0.56	0.00
S=1	1.91 - 1.95	1.71	132.0		0.30
	(1.92 - 1.97)	(1.65)	(150.7)		

Mn(Cor)-(NMes) and Mn(Cz)(NMes) results are in good agreement with the experimental X-ray structures [39, 41]. Experimental data are not available for Mn(Cor)-(NtClPh) but are expected to be similar to Mn(Cor)(NMes). The structure of Mn(Cor)(NTs) has not been determined but the theoretical estimates can be compared with the X-ray structure of the chromium analogue [42]. In the low-spin state all four ligands axially bind to the Mn(Cor) and Mn(Cz) moieties in a linear fashion, forming a short Mn-N bond, typical of imido-complexes. In all cases the Mulliken spin density in the triplet state gives almost 2.3 alpha electrons on the metal centre and 0.2 beta electrons on N_{axial}, confirming that in this state the unpaired electrons are localized on Mn. This indicates that states with a radical on corrole or corrolazine are higher in energy (see Fig. 6.5).

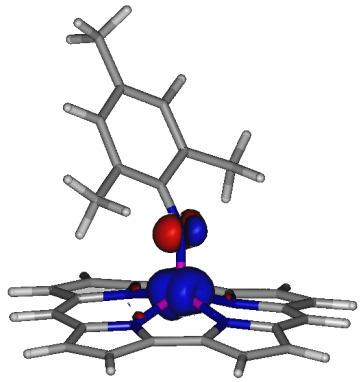

Figure 6.5. Spin density in the Mn(Cor)(NMes) triplet state BP86/def2-TZVP optimized geometry (isocontour=0.009).

As expected, corrolazine coordinates to Mn with shorter distances (Mn-$N_{pyrrole}$) due to the smaller cavity size, which is also responsible for a larger out of $N_{pyrrole}$ plane displacement of the metal centre ($\triangle$). This $\triangle$ is noticeable in all complexes and induces bonding and anti-bonding mixing between the $N_{pyrrole}$ σ and the $3d_{xz,yz}$ orbitals (see Fig. 6.6).

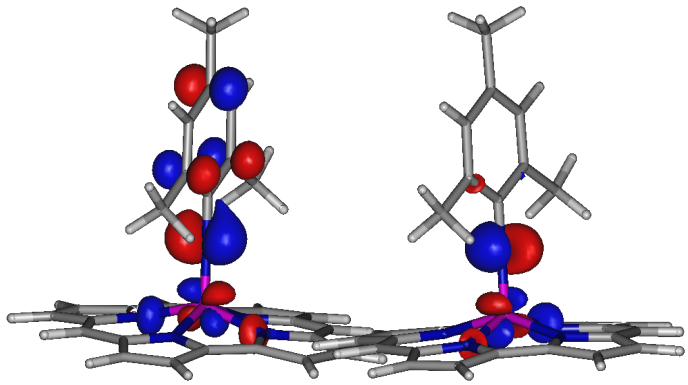

Figure 6.6. Anti-bonding mixing of $2p_{x,y}$ N_{axial} and σ $N_{pyrrole}$ orbitals with $3d_{xz,yz}$ of Mn (isocontour=0.05).

The corrole and corrolazine macrocycles show a ruffling distortion in the triplet state making it impossible to quantify $\triangle$. The increased mixing widens the gap

between the $3d_{xy}$ and the $3d_{xz,yz}$ orbitals, favouring the double occupation of the Mn-$3d_{xy}$ orbital and stabilizing the singlet state [51]. In the triplet state, the distance between Mn and the axial ligand increases due to the occupation of one of the π anti-bonding $(3d_{xz}\text{-}2p_x)^*$ or $(3d_{yz}\text{-}2p_y)^*$ orbitals.

6.3 Multiconfigurational wave function calculations

In line with the general findings with local density- and gradient-corrected functionals that tend to overestimate the stability of the low-spin states [52–54], we observe that the BP86 calculations predict singlet ground states for all the imide derivatives. However, these results are not completely consistent with experimental data in [Mn(Cor)(NTs)], which is assigned as a triplet by magnetic susceptibility measurements. Therefore, we will now proceed with the discussion of the multiconfigurational wave function calculations of the electronic states, which should improve our description.

6.3.1 Single point energy calculations

CASSCF and CASPT2 single point calculations have been carried out on top of the BP86 optimized geometries for singlet and triplet states (see Sec. 6.2). Basis I (Mn ANO-rcc [55, 56] contracted to [7s6p5d2f1g]; N, C, O, S, Cl ANO-s [57] contracted to [4s3p1d]; H ANO-s contracted to [2s]) and basis II (ANO-rcc on all atoms contracted to [7s6p5d3f2g1h] for Mn, [4s3p2d1f] for N, C, O, S, Cl and [3s1p] for H) have been compared. The [10,12] active space consists of the Mn 3d orbitals ($3d_{xz}$, $3d_{yz}$, $3d_{xy}$, $3d_{x^2-y^2}$ and $3d_{z^2}$), three diffuse orbitals that account for the double shell effect ($4d_{xz}$, $4d_{yz}$ and $4d_{xy}$), and four ligand orbitals ($2p_x$, $2p_y$ and $2p_z$ for N_{axial} and σ for $N_{pyrrole}$). This active space is required to obtain accurate reference wave function [58]. Instead of being localized, the Mn 3d and ligand orbitals form bonding and anti-bonding combinations. The orientation of the system with the $N_{pyrrole}$ on the x- and y-axes makes that Mn $3d_{xz}$, $3d_{yz}$ and $3d_{z^2}$ interact with N_{axial} $2p_x$, $2p_y$ and $2p_z$ orbitals to form

a bonding and anti-bonding pair of orbitals with occupations close to 2 and 0 respectively. Mn $3d_{x^2-y^2}$ combines with $N_{pyrrole}$ $2p_x$ and $2p_y$ to form σ and σ^* orbitals. Mn $3d_{xy}$ is non-bonding and more stable than the anti-bonding combinations. As an example, Figure 6.7 illustrates the [Mn(Cor)(NMes)] case.

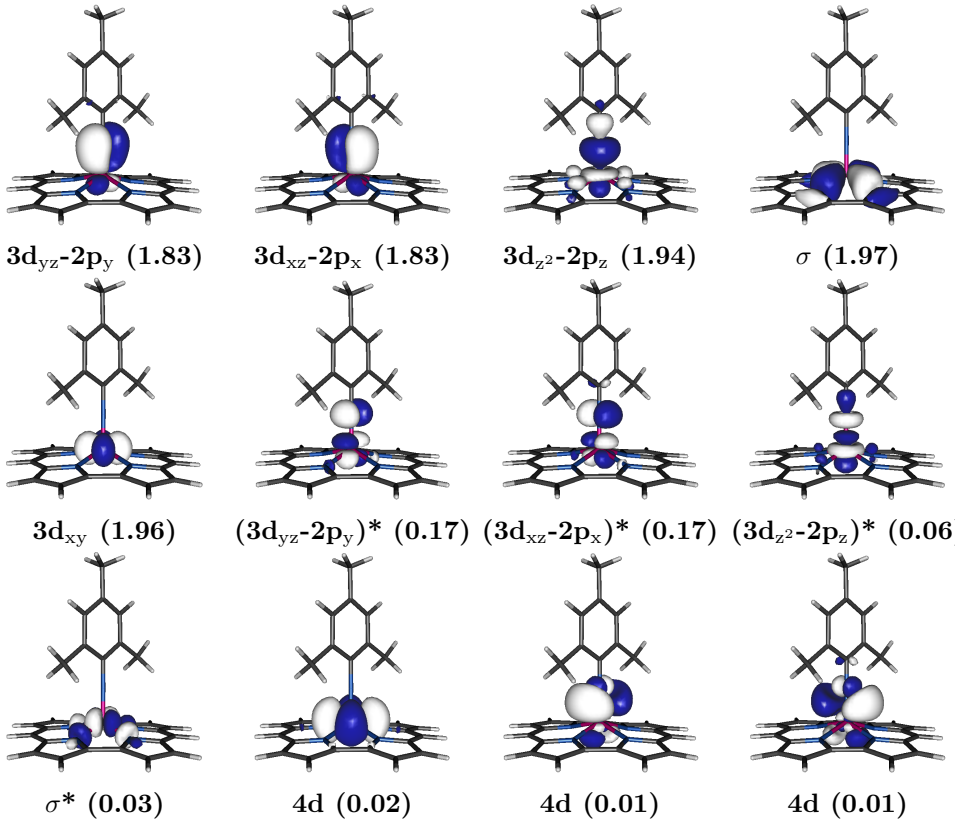

Figure 6.7. [10,12]-CASSCF active orbitals for the singlet [Mn(Cor)(NMes)]. Occupation numbers in parenthesis.

The comparison of entries [10,12]-CASSCF and CASPT2 in Table 6.2 shows that the addition of the electron correlation up to second order that is not taken into account in the CASSCF approach leads to important changes of the relative energy of the spin states in the here-studied imido complexes. Results of CASPT2 calculations predict singlet ground states for all complexes except for the NTs complex with the weakest π-donating axial ligand, for which both spin states are predicted to be nearly degenerate. The second triplet state of the

complex with the NtClPh ligand, which is of intermediate π-donating strength, has a lower relative energy than the second triplet state in the NMes complex, which has the strongest π-donating ligand. This shows that the stronger electron donation increases the $3d_{xz,yz}$ relative orbital energy. A considerable energy gap separates the first and second triplets of all imido complexes, in contrast with complexes with the cylindrically symmetric oxo axial ligands, for which the two high-spin states are degenerate [22].

Table 6.2. [10,12]-CASSCF/CASPT2 main configurations and relative energies (in eV) of the singlet and triplet states obtained with the BP86/TZVP optimized geometries.

		CASSCF		CASPT2	
	main configuration	Basis I	Basis II	Basis I	Basis II
[Mn(Cor)(NMes)]					
S=0	$(3d_{xy})^2$	0.00	0.00	0.00	0.00
S=1	$(3d_{xy})^1(3d_{xz}\text{-}2p_x)*^1$	0.61	0.60	0.17	0.18
	$(3d_{xy})^1(3d_{yz}\text{-}2p_y)*^1$	1.65	1.63	1.19	1.18
[Mn(Cz)(NMes)]					
S=0	$(3d_{xy})^2$	0.00	0.00	0.00	0.00
S=1	$(3d_{xy})^1(3d_{xz}\text{-}2p_x)*^1$	0.74	0.74	0.24	0.25
	$(3d_{xy})^1(3d_{yz}\text{-}2p_y)*^1$	1.71	1.70	1.19	1.19
[Mn(Cor)(NtClPh)]					
S=0	$(3d_{xy})^2$	0.00	0.00	0.00	0.00
S=1	$(3d_{xy})^1(3d_{xz}\text{-}2p_x)*^1$	0.43	0.42	0.16	0.17
	$(3d_{xy})^1(3d_{yz}\text{-}2p_y)*^1$	1.27	1.28	0.85	0.87
[Mn(Cor)(NTs)]					
S=0	$(3d_{xy})^2$	0.00	0.00	0.00	0.00
S=1	$(3d_{xy})^1(3d_{yz}\text{-}2p_y)*^1$	0.11	0.11	-0.02	0.00

The Mn–N_{axial}–R angle of the triplet state geometries is not linear, diminishing the overlap of the $(3d_{xz}\text{-}2p_x)$ or the $(3d_{yz}\text{-}2p_y)$ pair of orbitals. Taking as example the NTs complex in the triplet state (see Fig.6.8), the axial ligand is bend towards the y-axis and the mixing between $3d_{yz}$ and $2p_y$ is smaller than between $3d_{xz}$ and $2p_x$. As a consequence, the antibonding $(3d_{yz}\text{-}2p_y)$* orbital is stabilized and its occupation is favoured [42]. When compared to corrole, the smaller cavity size of corrolazine results in a shortening of the Mn-$N_{pyrrole}$ bond and an increase of the out of $N_{pyrrole}$ plane displacement, giving rise to an even more unstable triplet state. The energy of the triplet state of [Mn(Cor)(NTs)]

is found at a much lower energy with CASPT2 than with BP86, but the description is still not consistent with the experimental data.

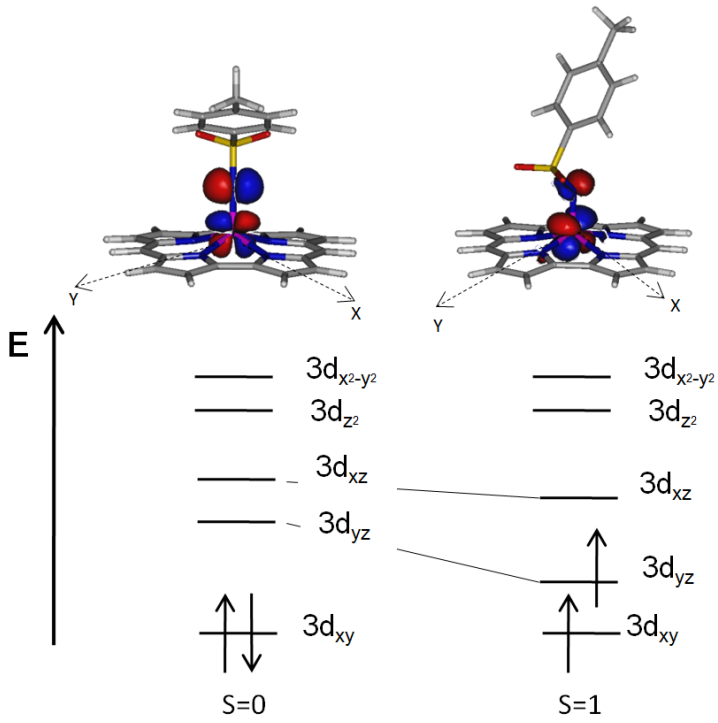

Figure 6.8. Schematic representation of the energetic ordering of the molecular orbitals for the singlet (left) and first triplet (right) states of [Mn(Cor)(NTs)] (isocontour=0.05).

6.3.2 Reoptimization of [Mn(Cor)(NTs)]

The near-degeneracy of the singlet and lowest triplet state of the NTs complex triggers the need to reconsider the geometry optimization performed with the BP86 functional. As mentioned in Chapter 2, reoptimization of some key geometrical parameters with CASPT2 can lead to important improvements in the relative energies of interest [59]. In this case the most obvious parameters to be reoptimized are the Mn–N distance and the Mn–N–S angle. The BP86 optimized geometries have been taken as starting point for the singlet and triplet states, respectively, for a [10,12]-CASPT2 scan along the axial coordination

distance. The orbitals of the active space used in these calculations are illustrated in Figure 6.9. At each point of the scan, the Mn-N_{axial} distance and the Mn–N–S angle were kept fixed at a certain value, while the rest of structural parameters were optimized with BP86/TZVP. CASPT2 single point calculations with basis I have been performed to evaluate the energy of the so-obtained geometries. Since the axial coordination angle is linear in the singlet geometry, the angle was only scanned for the triplet state.

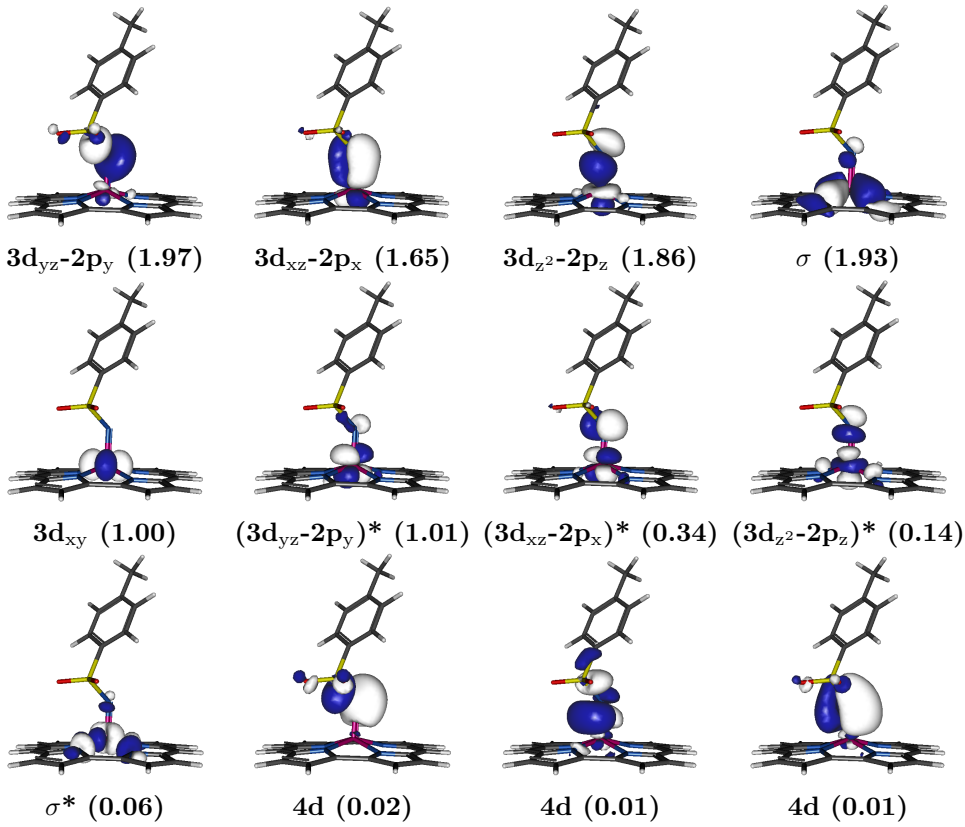

Figure 6.9. [10,12]-CASSCF active orbitals for the triplet [Mn(Cor)(NTs)]. Occupation numbers in parenthesis.

As can be seen in Table 6.3, when decreasing the Mn-N_{axial}-S angle, [10,12]-CASPT2 calculations with basis I and basis II predict the experimentally expected high-spin ground state and a reasonable gap with the singlet state. Comparison of the [10,12]-CASPT2/BP86 geometries with those reported in Table

6.1 reveals that small variations in the Mn-N_{axial} distance (on the order of 0.03 Å) and the Mn–N_{axial}–S angle ($\sim 10°$) can remove the degeneracy of the S=0 and S=1 states of these complexes. Different from the other imido-complexes, NTs contains a tetrahedral sulfur atom between N_{axial} and the phenyl ring (see Fig. 6.3), giving flexibility to the structure of the axial ligand and favouring geometries with a non-linear coordination angle. In conclusion, being the weaker π-donating ligand and favouring bent axial angles, NTs accomplishes all the factors to exhibit a triplet ground state.

Table 6.3. Main electronic configurations, reoptimized Mn–N_{axial} distances (in Å) and Mn–N_{axial}–S angles (in degrees), and relative energies (in eV) of the singlet and triplet states of the NTs imido-complex. BP86 results of Sec. 6.2 in parenthesis for comparison.

			CASPT2	
	Mn-N_{axial}	Mn-N_{axial}-S	Basis I	Basis II
$(3d_{xy})^2$	1.60	168.2	0.00	0.00
	(1.62)	(167.0)		
$(3d_{xy})^1(3d_{yz}\text{-}2p_y)*^1$	1.75	125.0	-0.08	-0.07
	(1.71)	(132.0)		

6.3.3 Core correlation: a comparison of second order and variational situations

Being of moderate computational cost, CASPT2 seems to be a very efficient computational strategy to obtain accurate relative energies of spin states. The validity of applying a level shift of 0.1 Eh to avoid the appearance of intruder states and the choice of the zeroth-order Hamiltonian with IPEA equal to 0.25 is well-established, and the only point that deserves further attention is the accuracy of the pertubative estimate of the core correlation. Typically, the core electrons of main group elements are excluded from the CASPT2 energy estimation, since they do not introduce any differential effect on the energies of spin states. In the case of first-row transition metals, the situation is slightly different because the semi-core 3s-3p electrons can change the relative energy of the spin states by ∼0.1–0.2 eV when included in the multireferential second-order perturbative correction [60] . However, recent results by Pierloot et al. [61]

indicate that the correlation energy description by CASPT2 of these electrons is probably not fully consistent, leading to wrong estimations of the high and low-spin energies in some cases.

In order to validate the multiconfigurational calculations of the present work, the Mn 3s-3p contribution up to the second order electron correlation in all the imido-complexes has been compared with a variational estimate obtained by DDCI [62, 63]. As can be seen in Table 6.4, the CASPT2 3s-3p contribution is quantitatively similar for all complexes and in all cases stabilizes the triplet state by around 0.2 eV. The importance of 3s-3p correlation is reflected in the fact that it inverts the ground state of [Mn(Cor)(NTs)]. To make feasible the DDCI calculations a significant reduction of the molecular orbital space is required. The doubly occupied and empty CASSCF orbitals have been localized following the scheme outlined in Ref. [64–66], and subsequently, classified in terms of core, σ and π orbitals to select the most relevant orbitals to be taken into account in the DDCI calculation. Two molecular orbital spaces were considered, the first contains the π and π^* orbitals in addition to the twelve active orbitals, the second space extends the first one with the Mn 3s-3p orbitals. The reference wave function for the DDCI calculation is constructed from a [2,2]-CASCI calculation using the orbitals that are singly occupied in the triplet state; $3d_{xy}$ and $(3d_{xz}\text{-}2p_x)^*$ or $(3d_{yz}\text{-}2p_y)^*$ depending on the complex. The [2,2]-DDCI estimate of the 3s-3p correlation contributions to the triplet-singlet energy difference are slightly lower than those calculated with [10,12]-CASPT2, but no relevant differences are detected. The addition of more virtual orbitals in the DDCI calculation increases the correlation energy, but has no differential effects.

Table 6.4. [10,12]-CASPT2 and [2,2]-DDCI estimates of the Mn 3s-3p electron correlation contribution (in eV) to the triplet-singlet energy difference for the four imido-complexes.

	[10,12]-CASPT2	[2,2]-DDCI
[Mn(Cor)(NMes)]	-0.24	-0.13
[Mn(Cz)(NMes)]	-0.25	-0.17
[Mn(Cor)(NtClPh)]	-0.11	-0.13
[Mn(Cor)(NTs)]	-0.21	-0.11

6.3.4 Wave function analysis

The assignment of charges to atoms (or groups of atoms) in a molecule is a delicate matter. The atomic charge is not observable, and computationally derived charges show a large dependence on the strategy applied to calculate them. Without pretending to determine *exact* charges, we have used an orthogonal valence bond reading of the multiconfigurational wave function to extract more information about the electronic structure and assign populations to the Mn atom in the different complexes. Atomic-like and fragment orbitals are ideally suited to describe many chemical concepts in terms of the valence bond theory in an intuitive manner [67], but they are computationally speaking not the most ideal choice as orbital basis. On the other hand, CASSCF wave functions are normally expressed with molecular orbitals, computationally much simpler to handle, and also because they give direct information about molecular spectroscopy and ionization potentials, among other properties. A unitary transformation of the CASSCF active orbitals is performed to maximize the weight of the metal basis functions, giving atomic-like orbitals and, as a consequence of the rotation process, the weight of the ligands in the others. The wave function is invariant upon this transformation. The re-expression of the multiconfigurational CASSCF wave function in this new orbital basis makes it possible to capture the electronic structure in similar intuitive concepts to those in traditional valence bond calculations [68]. This orthogonal valence bond analysis has been used before to study TM-ligand interactions [69–72] and to decompose the magnetic coupling in organic radicals [73]. The effect of

orbital localization is illustrated in Fig. 6.10 and transfers the covalency contained in the delocalized orbitals to the configuration expansion [74, 75]. In the present case all twelve orbitals of the active space have been localized.

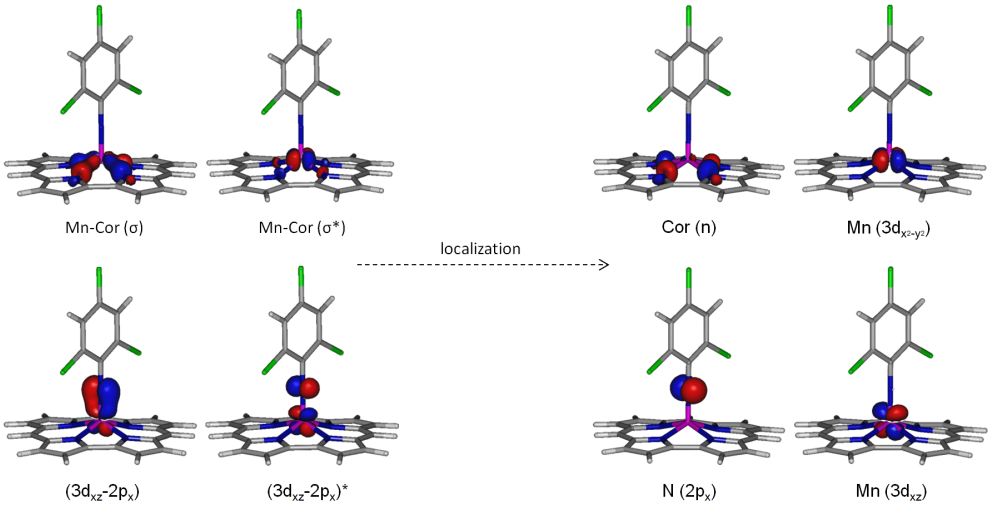

Figure 6.10. Example of orbitals before and after the localization procedure (isocontour=0.05). σ and ($3d_{xz}$-$2p_x$) bonding and anti-bonding couple of orbitals are transformed in metal, imide and corrole localized orbitals.

Table 6.5 summarizes the orthogonal valence bond analysis of the electronic structure of the four imido-complexes. For this purpose, the configurations of the CASSCF wave function have been classified by the number of electrons in the metal valence orbitals and the weight of the configurations has been summed for each subgroup, as shown in Table 6.5. The wave function is dominated by configurations with five electrons on the Mn ion, but configurations with four or six electrons also contribute significantly. The weighted sum of the d electrons in each configuration gives what we call the d-count, which is close to 5 in all complexes except for [Mn(Cor)(NTs)] in the triplet state.

Table 6.5. Orthogonal valence bond analysis of the [10,12]-CASSCF wave function of the four imido-complexes. Electronic configurations in the wave function are grouped by the number of electrons in the Mn d orbitals, and the total weight is given as a percentage. The d-count is the weighted sum of electrons on the metal centre.

	Mn^0 ($7e^-$)	Mn^+ ($6e^-$)	Mn^{2+} ($5e^-$)	Mn^{3+} ($4e^-$)	Mn^{4+} ($3e^-$)	total weight	d-count
[Mn(Cor)(NMes)]							
S=0	4.2	22.7	44.6	25.5	2.4	99.4	**5.01**
S=1	3.0	18.9	46.4	29.1	1.8	99.2	**4.92**
[Mn(Cz)(NMes)]							
S=0	4.2	22.3	43.8	26.3	2.9	99.4	**4.99**
S=1	2.7	17.9	45.9	30.5	2.2	99.2	**4.88**
[Mn(Cor)(NtClPh)]							
S=0	4.5	23.6	44.8	24.5	2.1	99.4	**5.04**
S=1	3.9	22.1	45.9	25.3	1.8	99.0	**5.01**
[Mn(Cor)(NTs)]							
S=0	4.4	23.2	45.0	24.9	2.0	99.4	**5.03**
S=1	0.9	8.7	40.1	43.6	6.1	99.3	**4.54**

As an example, for [Mn(Cor)(NMes)] in the singlet state this sum is performed as follows: [(0.042 x 7e$^-$ (Mn^0) + 0.227 x 6e$^-$ (Mn^+) + 0.446 x 5e$^-$ (Mn^{2+}) + 0.255 x 4e$^-$ (Mn^{3+}) + 0.024 x 3e$^-$ (Mn^{4+}))/0.994]. In a purely ionic model with a trianionic corrole and a dianionic imide ligand, one would rather expect a d-count of 2, corresponding to Mn^V. In the present analysis the effective charge differs from the formal charge and indicates that there is an important charge transfer from the coordination sphere to the Mn ion, which is probably better considered as an effective Mn^{2+} ion.

The electron count of the coordination sphere around the metal centre can be treated in a similar way to the assignment of the Mn charge. In the present calculations, a standard two-electron dative bond from the trianionic corrole to Mn is represented with two electrons in the corrole or corrolazine σ active orbital. As can be seen in Table 6.6, only half of the configurations correspond to this situation. The other configurations have only one electron in the corrole or corrolazine σ orbital. This corresponds to a strongly covalent Mn $3d_{x^2-y^2}$-σ bond. The present imido-Mn complexes are therefore not completely trianionic. With the same analysis the imido-to-metal charge transfer can be quantified by looking at the occupation of the three $2p_x$, $2p_y$ and $2p_z$ active orbitals localized on the nitrogen atom. The fact that the electron count of these is close to 3.5 denotes that the N–R group transfers 2.5 electrons to the d orbitals of the metal center. With more bent coordination angle and a stronger electron-withdrawing R group (SO_2), in the case of [Mn(Cor)(NTs)] in the triplet state only two electrons are transferred to the metal center. The smaller amount of charge transferred to Mn explains that although being favoured by the geometrical parameters, the triplet ground state in this complex is very close in energy to the singlet state. To sum up, the transfer of nearly three electrons (0.5 from corrole and 2.5 from imide) from the coordination sphere to the metal centre is the key to understand how TMs are stabilized in these imido complexes [25].

Table 6.6. Orthogonal valence bond analysis of the [10,12]-CASSCF wave function of the four imido complexes. Electronic configurations in the wave function are grouped by the number of electrons in the corrole, corrolazine and imide ligands, and the total weight is given as percentage.

	Cor^{3-} ($2e^-$)	Cor^{2-} ($1e^-$)	Count	R-N^- ($5e^-$)	R-N^0 ($4e^-$)	R-N^+ ($3e^-$)	R-N^{2+} ($2e^-$)	Count
[Mn(Cor)(NMes)]								
S=0	45.3	47.2	**1.38**	9.2	47.6	36.7	5.9	**3.60**
S=1	35.4	54.4	**1.26**	12.5	58.8	24.9	2.9	**3.82**
[Mn(Cz)(NMes)]								
S=0	43.7	48.3	**1.36**	10.6	48.5	34.8	5.4	**3.65**
S=1	35.3	54.3	**1.26**	14.0	59.3	23.2	2.6	**3.86**
[Mn(Cor)(NtClPh)]								
S=0	44.0	48.0	**1.36**	9.3	46.5	37.1	6.4	**3.59**
S=1	31.1	55.8	**1.19**	12.8	56.0	27.2	3.1	**3.79**
[Mn(Cor)(NTs)]								
S=0	44.8	47.6	**1.37**	9.5	46.2	36.9	6.6	**3.59**
S=1	34.7	55.2	**1.25**	30.2	57.8	9.7	0.9	**4.19**

6.4 Conclusions

The computational study presented here shows that the axial N-R ligand plays a fundamental role in the relative stability of the electronic states with different spin moment. The combination of DFT geometry optimizations and CASPT2 single-point calculations results in a description of the relative energies of the singlet and triplet coupled states that is consistent with the experimental information on four different imido-Mn corrole and corrolazine complexes. The DFT optimized geometries show identical corrole and corrolazine coordination distances in singlet and triplet, but important variations are observed in the coordination of the axial ligand. The singlet presents short distances and linear coordination, while the bond distance is longer for the triplet coupling, and the axial ligand also has a marked tendency to coordinate in a bent fashion. Furthermore, it is observed that electron-withdrawing groups in the axial ligand reduce the π interaction between metal and ligand and reduce the gap between the two singly occupied orbitals of the triplet state, hence, stabilizing it with respect to the singlet state. Hence, it is not unexpected that the system with the strongest electron-withdrawing group, the NTs complex, has a triplet ground state.

The orthogonal valence bond reading of the wave functions reveals important electron charge transfers from both the corrole/corrolazine ligand and the axial ligands to the Mn. The formal charge of Mn within an ionic model of the complexes corresponds to Mn^{5+}. However, the wave function shows that this high charge is reduced to an effective charge of 2+ by a transfer of nearly three electrons (2.5 from the axial ligand and 0.5 from the corrole/corrolazine) to the metal center.

6.5 References

[1] J. Groves, W. Kruper, and R. Haushalter, J. Am. Chem. Soc. **102**, 6375 (1980).

[2] R. Breslow and S. Gellman, J. Chem. Soc., Chem. Commun. pp. 1400–1401 (1982).

[3] R. Breslow and S. Gellman, J. Am. Chem. Soc. **105**, 6728 (1983).

[4] J. Groves and T. Takahashi, J. Am. Chem. Soc. **105**, 2073 (1983).

[5] E. Svastits, J. Dawson, R. Breslow, and S. Gellman, J. Am. Chem. Soc. **107**, 6427 (1985).

[6] N. Jin, J. Bourassa, S. Tizio, and J. Groves, Angew. Chem. Int. Ed. **39**, 3849 (2000).

[7] N. Jin, M. Ibrahim, T. Spiro, and J. Groves, J. Am. Chem. Soc. **129**, 12416 (2007).

[8] W. Song, M. Seo, S. George, T. Ohta, R. Song, M. Kang, T. Tosha, T. Kitagawa, E. Solomon, and W. Nam, J. Am. Chem. Soc. **129**, 1268 (2007).

[9] N. Jin and J. Groves, J. Am. Chem. Soc. **121**, 2923 (1999).

[10] F. De Angelis, N. Jin, R. Car, and J. Groves, Inorg. Chem. **45**, 4268 (2006).

[11] R. Latifi, L. Tahsini, B. Karamzadeh, N. Safari, W. Nam, and S. de Visser, Arch. Biochem. Biophys. **507**, 4 (2011).

[12] A. Jasat and D. Dolphin, Chem. Rev. **97**, 2267 (1997).

[13] R. Paolesse, S. Nardis, F. Sagone, and R. Khoury, J. Org. Chem. **66**, 550 (2001).

[14] A. Johnson and I. Kay, Proc. Chem. Soc. p. 89 (1964).

[15] Z. Gross, N. Galili, and I. Saltsman, Angew. Chem. Int. Ed. **38**, 1427 (1999).

[16] Z. Gross, N. Galili, L. Simkhovich, I. Saltsman, M. Botoshansky, D. Blaser, R. Boese, and I. Goldberg, Org. Lett. **1**, 599 (1999).

[17] Z. Gross, J. Biol. Inorg. Chem. **6**, 733 (2001).

[18] I. Aviv and Z. Gross, Chem. Commun. pp. 1987–1999 (2007).

[19] I. Aviv and Z. Gross, Chem. Eur. J. **15**, 8382 (2009).

[20] S. Berg, K. Thomas, C. Beavers, and A. Ghosh, Inorg. Chem. **51**, 9911 (2012).

[21] K. Thomas, A. Alemayehu, J. Conradie, C. Beavers, and A. Ghosh, Acc. Chem. Res. **45**, 1203 (2012).

[22] H. Zhao, K. Pierloot, E. Langner, J. Swarts, J. Conradie, and A. Ghosh, Inorg. Chem. **51**, 4002 (2012).

[23] A. Alemayehu, K. Gagnon, J. Terner, and A. Ghosh, Angew. Chem. Int. Ed. **53**, 14411 (2014).

[24] J. Capar, J. Conradie, C. Beavers, and A. Ghosh, J. Phys. Chem. A **119**, 3452 (2015).

[25] K. Pierloot, H. Zhao, and S. Vancoillie, Inorg. Chem. **49**, 10316 (2010).

[26] B. Roos, V. Veryazov, J. Conradie, P. Taylor, and A. Ghosh, J. Phys. Chem. B **112**, 14099 (2008).

[27] H. Vazquez-Lima, H.-K. Norheim, R. Einrem, and A. Ghosh, Dalton Trans. **44**, 10146 (2015).

[28] B. Ramdhanie, C. Stern, and D. Goldberg, J. Am. Chem. Soc. **123**, 9447 (2001).

[29] W. Kerber and D. Goldberg, J. Inorg. Biochem. **100**, 838 (2006).

[30] D. P. Goldberg, Acc. Chem. Res. **40**, 626 (2007).

[31] H. Liu, M. Mahmood, S. Qiu, and C. Chang, Coord. Chem. Rev. **257**, 1306 (2013).

[32] Z. Gross, G. Golubkov, and L. Simkhovich, Angew. Chem. Int. Ed. **39**, 4045 (2000).

[33] H. Liu, T. Lai, L. Yeung, and C. Chang, Org. Lett. **5**, 617 (2003).

[34] Z. Gross and H. Gray, Adv. Synth. Catal. **346**, 165 (2004).

[35] A. Kumar, I. Goldberg, M. Botoshansky, Y. Buchman, and Z. Gross, J. Am. Chem. Soc. **132**, 15233 (2010).

[36] B. Mandimutsira, B. Ramdhanie, R. Todd, H. Wang, A. Zareba, R. Czemuszewicz, and D. Goldberg, J. Am. Chem. Soc. **124**, 15170 (2002).

[37] D. Lansky, B. Mandimutsira, B. Ramdhanie, M. Clausen, J. Penner-Hahn, S. Zvyagin, J. Telser, J. Krzystek, R. Zhan, Z. Ou, et al., Inorg. Chem. **44**, 4485 (2005).

References

[38] D. Lansky and D. Goldberg, Inorg. Chem. **45**, 5119 (2006).

[39] R. A. Eikey, S. I. Khan, and M. M. Abu-Omar, Angew. Chem. Int. Ed. **41**, 3592 (2002).

[40] N. Edwards, R. Eikey, M. Loring, and M. Abu-Omar, Inorg. Chem. **44**, 3700 (2005).

[41] D. E. Lansky, J. R. Kosack, A. A. N. Sarjeant, and D. P. Goldberg, Inorg. Chem. **45**, 8477 (2006).

[42] M. J. Zdilla and M. M. Abu-Omar, J. Am. Chem. Soc. **128**, 16971 (2006).

[43] M. Abu-Omar, Dalton Trans. **40**, 3435 (2011).

[44] F. Weigend, M. Haser, H. Patzelt, and R. Ahlrichs, Chem. Phys. Lett. **294**, 143 (1998).

[45] F. Weigend and R. Ahlrichs, Phys. Chem. Chem. Phys. **7**, 3297 (2005).

[46] J. Perdew and Y. Wang, Phys. Rev. B **45**, 13244 (1992).

[47] J. Perdew, K. Burke, and M. Ernzerhof, Phys. Rev. Lett. **77**, 3865 (1996).

[48] J. Perdew, M. Ernzerhof, and K. Burke, J. Chem. Phys. **105**, 9982 (1996).

[49] J. Perdew, Phys. Rev. B **33**, 8822 (1986).

[50] A. Becke, Phys. Rev. A **38**, 3098 (1988).

[51] S. De Visser, F. Ogliaro, Z. Gross, and S. Shaik, Chem. Eur. J. **7**, 4954 (2001).

[52] A. Ghosh and P. Taylor, Current Opinion in Chemical Biology **7**, 113 (2003).

[53] M. Swart, A. Groenhof, A. Ehlers, and K. Lammertsma, J. Phys. Chem. A **108**, 5479 (2004).

[54] H. Chen, W. Lai, and S. Shaik, J. Phys. Chem. B **115**, 1727 (2011).

[55] B. Roos, R. Lindh, P.-. Malmqvist, V. Veryazov, and P.-O. Widmark, J. Phys. Chem. A **108**, 2851 (2004).

[56] B. Roos, R. Lindh, P.-. Malmqvist, V. Veryazov, and P.-O. Widmark, J. Phys. Chem. A **109**, 6575 (2005).

[57] K. Pierloot, B. Dumez, P.-O. Widmark, and B. Roos, Theor. Chim. Acta **90**, 87 (1995).

[58] K. Pierloot, Int. J. Quantum Chem. **111**, 3291 (2011).

[59] K. Pierloot and S. Vancoillie, J. Chem. Phys. **125**, 124303 (2006).

[60] K. Pierloot, E. Tsokos, and B. Roos, Chem. Phys. Lett. **214**, 583 (1993).

[61] K. Pierloot, Q. Phung, and A. Domingo, p. **To be published** (????).

[62] J. Miralles, J. Daudey, and R. Caballol, Chem. Phys. Lett. **198**, 555 (1992).

[63] J. Miralles, O. Castell, R. Caballol, and J. Malrieu, J. Chem. Phys. **172**, 33 (1993).

[64] D. Maynau, S. Evangelisti, N. Guihery, C. Calzado, and J. Malrieu, J. Chem. Phys. **116**, 10060 (2002).

[65] C. Calzado, S. Evangelisti, and D. Maynau, J. Phys. Chem. A **107**, 7581 (2003).

[66] N. Ben Amor, F. Bessac, S. Hoyau, and D. Maynau, J. Chem. Phys. **135**, 014101 (2011).

[67] S. Shaik and P. Hiberty, A Chemist's Guide to Valence Bond Theory (Wiley, 2007), ISBN 9780470192580.

[68] W. Wu, P. Su, S. Shaik, and P. Hiberty, Phys. Chem. Chem. Phys. **111**, 7557 (2011).

[69] M. Radon, E. Broclawik, and K. Pierloot, J. Phys. Chem. B **114**, 1518 (2010).

[70] J. Zapata-Rivera, R. Caballol, and C. Calzado, Phys. Chem. Chem. Phys. **13**, 20241 (2011).

[71] J. Zapata-Rivera, R. Caballol, and C. Calzado, J. Comput. Chem. **32**, 1144 (2011).

[72] J. Zapata-Rivera, R. Caballol, and C. Calzado, J. Comput. Chem. **33**, 1407 (2012).

[73] C. Angeli, C. Calzado, C. de Graaf, and R. Caballol, Phys. Chem. Chem. Phys. **13**, 14617 (2011).

[74] A. Sadoc, R. Broer, and C. de Graaf, J. Chem. Phys. **126**, 134709 (2007).

[75] A. Sadoc, R. Broer, and C. de Graaf, Chem. Phys. Lett. **454**, 196 (2008).

Chapter 7

Conclusions

As exposed in the introduction, advances in the synthesis and characterization of transition metal complexes have given room to new and promising materials with spin-crossover and other interesting magnetic properties. In this thesis we have used the *ab initio* methods described in the theoretical background chapter to get insights on magnetic and photochemical properties of spin-crossover complexes with transition metals beyond the widely studied octahedral $Fe^{II}N_6$ systems. The conclusions that are extracted from this work can be divided into two parts. First, we will expose some technical conclusions related with the computational part of the work, and thereafter a list is given that summarizes the most important findings concerning the physics of the systems studied.

Computational issues:

DFT or TD-DFT has been found to deliver reliable geometries for those cases where experimental data are available. This allows us to determine the optimal geometry for excited states and metastable spin states, for which experimental data are absent or only indirect indications of some geometrical parameters can be found in the literature. This is especially interesting for excited states or metastable spin states. Although this study and previous works in the literature indicate that the nature of the functional used in the optimization is not crucial

–most functionals lead to similar geometries–, we have found some exceptions. The most salient one is the prediction of a very long Mn-N_{axial} bond distance by the PBE0 functional for the corrole and corrolazine complexes discussed in Chapter 6. This has been ascribed to the large spin contamination of the triplet state. Hence, the results should be carefully checked to detect possible anomalous behaviour of (TD-)DFT.

In the study of the spin-crossover complexes with extended π systems the choice of the functional is a more delicate matter. The use of functionals that do not accurately treat the dispersion interactions can easily lead to incorrect geometries and in consequence incorrect representations of the electronic structure. This has been observed in this work by comparing the geometries of the NiTPP-PAPy complex optimized with the BP86 and the M06-2X functionals. The latter functional, optimized to give an accurate description of the dispersion, places the pyridine ring of the PAPy group close and parallel to the porphyrin ring, optimizing the π-π interactions, while the BP86 functional maximizes the separation between the two subsystems. We have observed that the combination of B3LYP and the D3 correction of Grimme leads to similar results as the M06-2X functional.

The inclusion of solvent effects with PCM or COSMO models does not have significant effects on the geometries, the relative energies and the wave function of the different spin states of the complexes studied here. The small effect of the solvent has been analysed in some detail for the absorption spectrum of $[Ru(bpy)_3]^{2+}$. The metal-centred excitations do not induce significant changes in the dipole of the complex and solvent effects are logically small. The ^{1}MLCT vertical excited states could induce larger changes in the dipole but the unpaired electron is delocalized over the three ligands in a symmetric manner and only a small dipole moment is created. In fact, the DFT estimations of the reduction potentials of this complex are the only properties where the solvent has a significant role throughout this thesis.

In some cases, DFT geometries have to be refined through a reoptimization of certain geometrical parameters with single point CASPT2 calculations on a series of structures obtained by restricted DFT optimizations. The Ru-N

distances in the singlet state of $[Ru(bpy)_3]^{2+}$ obtained with this procedure coincide with the PBE0 ones. This is somewhat unexpected since a shortening of 0.1 Å was obtained in the analogous $[Fe(bpy)_3]^{2+}$ complex. On the contrary, the CASPT2/DFT reoptimization of the axial coordination distance and angle in Mn corrole and corrolazine complexes removes the degeneracy of the singlet and triplet states. Small variations of these parameters result in stabilization of the triplet state.

While DFT and TD-DFT perform rather well in the reproduction of the absorption spectra (see $[Ru(bpy)_3]^{2+}$), they fail predicting high-spin low-spin relative energies. Multiconfigurational single point energy calculations have been used to this purpose. The choice of an adequate active space for the CASSCF calculations is fundamental and in this sense one has to take into account the system and the problem studied in each case. Sometimes this can lead to computationally unaffordable calculations. An example is found in Chapter 5, where the d-d states of Ni, the isomerization of PAPy and the spectrum of the whole system have potential interest to understand the spin-crossover mechanism of the complex but the active space required to study all this features is too large and we have tackled the problem by parts. In most of the cases, the non-dynamical electron correlation accounted at CASSCF level is not enough for a quantitative description of the relative energies and we have to include the dynamic correlation in terms of CASPT2 calculations.

To have an overall view of the processes involved in the spin-crossover induced by light, the study of the energies of the different states has to be complemented with the estimation of the time-scale on which these processes occur. Fermi's golden rule has been used to estimate intersystem crossing rates. The large spin-orbit coupling between states with the same electronic configuration favours this crossing and the large overlap of the vibrational wave functions of states with similar geometries also facilitates the process.

The 3s-3p contribution to the dynamic electron correlation is non-negligible when two spin states are close in energy. In Chapter 6, its inclusion stabilizes the triplet states by 0.2 eV and in one case changes the ground state of the complex. In some cases, the inclusion of this part of the correlation with

CASPT2 had been shown to be not fully consistent and has deserved our special attention. In this work, we have estimated the 3s-3p correlation in terms of DDCI calculations and made a comparison with the CASPT2 results. No significant differences have been detected for the Mn complex.

Physics of the spin-crossover systems:

In the $[Ru(bpy)_3]^{2+}$ complex DFT, TD-DFT and CASSCF calculations show that during the relaxation of the MLCT states the unpaired electron becomes localized on a single pyridine ligand. Once localized, the electron remains confined since the probability of inter-ligand electron transfer between two bipyridine ligands has been estimated to be low with CAS state interaction calculations. Localization and trapping favour the electron transfer to acceptor molecules in the MLCT states. Furthermore, our DFT estimation of the reduction potential of the MLCT states indicates that the electron transfer is favoured in the ^{3}MLCT state over the singlet ground state state, confirming the experimental findings. The possibility of spin-crossover in $[Ru(bpy)_3]^{2+}$ has been analyzed in terms of DFT and multireference wave function calculations of the relative energies of the metal centred triplet states.

Ni-porphyrins are also susceptible to light induced spin crossover processes. The TD-DFT and CASPT2 calculations confirm that irradiation with light of 500 nm induces a π-π^* excitation in the porphyrin moiety which after relaxation and intersystem crossing reaches a metal centred triplet state. Our calculations indicate that the axial coordination of a pyridine solvent molecule is barrierless and greatly stabilizes the S=1 state. On the contrary, the coordination represents a large barrier on the ground state surface, indicating that spin crossover can only be attained by irradiation. The inverse process of decoordination is also shown to have a significant barrier. This indicates that the initial situation can only be restored by a π-π^* excitation that deactivates into a closed-shell singlet in a square-pyramid conformation of the complex, which releases the axial ligand to recover the original square-planar geometry.

In the Ni porphyrin functionalized with a PAPy DFT and multiconfigurational calculations have shown that the 500 nm excitation induces a π-π^* excitation involving a π orbital of the porphyrin and a π^* orbital with contributions from

both the porphyrin and the N=N group of the PAPy arm. The orbitals implied in this excitation are different from the ones in the isomerization of the isolated PAPy systems, explaining the anomaly in the wavelength. Furthermore, we have studied the isomerization mechanism of the PAPy arm. Isomerization is most probable through the rotation mechanism and can part from two different excited states, each with a different relaxation path. This can explain the experimental observation that irradiating with light of two different wavelengths, different quantum yields are observed.

The role of the axial ligand in Mn corrole and corrolazine complexes in the relative energies of the magnetic states of these complexes axially coordinated to three different imide ligands has been confirmed. The singlet-triplet gap presents a clear dependence on both the axial coordination distance and angle. These parameters directly affect the energy of the metal 3d orbitals and while singlet states are favoured by linear angles and short distances, triplets prefer bent angles and long distances. This effect is crucial in the complex with the N-tosyl axial ligand, which has a triplet ground state. Furthermore, our orthogonal valence bond analysis of the wave function shows that the manganese ion is highly stabilized by the transfer of electrons from both the equatorial macrocycle and the axial imide ligand to the metal centre. This study opens the door to control the magnetic states of Mn corrole and corrolazines modifying the nature of the imide axial ligand.

List of publications

1. **Spin-crossover in phenylazopyridine-functionalized Ni-porphyrin: trans-cis isomerization triggered by $\pi - \pi$ interactions.** G. Alcover-Fortuny, C. de Graaf and R. Caballol. Phys. Chem. Chem. Phys. **17**, 217-225 (2015)

2. **Role of the imide axial ligand in the spin and oxidation state of manganese corrole and corrolazine complexes.** G. Alcover-Fortuny, R. Caballol, K. Pierloot and C. de Graaf. Inorg. Chem. **55**, 5274-5280 (2016)

3. **Elucidating the reversible light-induced mechanism for the photoisomerization of phenylazopyridine.** J. Casellas, G. Alcover-Fortuny, M. Reguero and C. de Graaf. (Manuscript in preparation)

4. **Anti Lippert-Mataga behaviour explained. Computational predictions on Stokes shifts corroborated by measurements in Ru(II) polypyridil complexes.** G. Alcover-Fortuny, J. Casellas, G. Ielasi, C. de Graaf, G. Orellana and M. Reguero. (Manuscript in preparation)

5. **Solvent and substitution effects on the photochemistry of $[Ru(bpy)_3]^{2+}$.** G. Alcover-Fortuny, J. Wu, R. Caballol and C. de Graaf. (Manuscript in preparation)

6. **Light-induced excited state spin trapping in Ni porphyrin complexes in coordinative solvents.** G. Alcover-Fortuny, C. de Graaf and R. Caballol. (Manuscript in preparation)